Attachment B

SSC Conceptual Design
Magnet Design Details

March 1986

SSC Central Design Group*

*Operated by Universities Research Association
under contract with the U.S. Department of Energy

A publication of the SSC Central Design Group
c/o LBL, 90/4040, 1 Cyclotron Road, Berkeley,
CA 94720 (415) 486-4772.

Editor:	J.D. Jackson
Art Editor:	R.G. Barton
Production Editor:	R. Donaldson
Typesetting:	D.K. Savage

U.S. Department of Energy
Contract DE-AC02-76CH03000/3001

Universities Research Association, 1111 19th
Street, N.W. Suite 400, Washington, DC 20036

Contents

B.1 Dipole Magnets: A Brief Description

C. Taylor
Lawrence Berkeley Laboratory
and
P. Dahl
Brookhaven National Laboratory

April 1986

B.1.1 Introduction

There are 7680 superconducting dipole magnets, each 17 m long, and 1356 3.3-m long quadrupoles in the regular bending arcs of the collider, as well as numerous special magnets to bring the two counter-rotating beams into collision in the interaction regions (experimental areas). The magnet system is the most challenging technical component of the collider, and is a major determinant of its cost. The dipole magnetic field strength determines the circumference of the collider ring and, thus, the cost of the tunnel. For these reasons, considerable effort has been devoted to minimizing the cost of the dipole magnets and selecting an operating field strength consistent with reasonable design principles [B.1-1] and minimum facility cost. The magnet aperture and operating field dictate the overall size of the magnet and, hence, the quantity of costly materials: superconductor, iron, stainless steel. (The superconductor alone accounts for approximately 30% of the cost of the magnet system.) The 40 mm aperture chosen is the minimum size that will accommodate the circulating beam at the injection energy of 1 TeV with allowances for inevitable deviations of the actual multipole fields from the design values. The maximum operating field strength, 6.6 T, is the highest value consistent with the use of NbTi superconducing alloy, conventional helium refrigeration technology, a superconducing cable that is very similar to one used in the Tevatron [B.1-2], and a cold-iron collared magnet design based on a two-layer coil structure. Here we summarize the salient features of this design, the main parameters of which are listed in Table B.1-1. The remainder of Attachment B documents particular aspects of the magnet design, including the performance (training behavior, field quality) of several series of model dipole magnets.

During the past two years, the dipole design has been refined through an intense multilaboratory effort spanning the national laboratories, university teams, and industry. Its most visible manifestation has been the construction and testing of approximately twenty full cross-section model magnets ranging in length from 1 m to 4.5 m [B.1-3]. Full-length (17 m) dipoles are presently under construction; following individual tests of these units they will be incorporated in a magnet "string" for a magnet system test.

Table B.1-1
Dipole Magnet Parameters

General	
No. of dipoles per ring	3840
Overall length [m]	17.4
Magnetic length [m]	16.6
Bore tube inner diameter [mm]	32.26
Mass of conductor [kg]	208
Cold mass [kg]	6759
Central field at injection [T]	0.33
Central field at 20 TeV [T]	6.6
Current at 20 TeV [A]	6500
Inductance [mH]	53
Stored energy [MJ]	1.12
Magnetic multipoles for infinite μ	
[at 1 cm, $b_n \times 10^4$]	
Sextupole, b_2	−0.0002
Decapole, b_4	−0.0008
14-Pole, b_6	−0.0049
18-Pole, b_8	−0.0014
22-Pole, b_{10}	0.0107
26-Pole, b_{12}	0.0116
Internal trim coil harmonic	b_2/b_4
Maximum trim coil field at 1 cm [G]	27/8
Maximum trim coil current [A]	5/5
Bore Tube Assembly	
Bore tube, material	Nitronic 40
Outer diameter [mm]	34.54
Wall thickness [mm/in.]	1.016/0.040
Copper coating [mm/in.]	0.127/0.005
Trim coil, type	Sextupole/decapole
Mean diameter [mm]	35.15/35.80
No. of turns per pole	15/9
Monolithic wire diameter, bare [mm/in.]	0.305/0.012
Monolithic wire diameter, insulated [mm/in.]	0.381/0.015
Spacers, number	8
Spacers, thickness [mm/in.]	1.397/0.055
Radial clearance to coil [mm/in.]	1.397/0.055
Winding	
Inner Layer	
Inner diameter [mm]	40.00
Outer diameter [mm]	59.23
Length, coil straight section [m]	16.54
Length, overall [m]	16.75
Cable length [m]	1076
Cable mass [kg]	100
Maximum field [T]	7.0
No. of turns	16
No. of turns, 1st block	5
First wedge mid-thickness (insulated) [mm]	1.46
No. of turns, 2nd block	5
Second wedge mid-thickness (insulated) [mm]	2.90
No. of turns, 3rd block	4
Third wedge mid-thickness (insulated) [mm]	3.31
No. of turns, 4th block	2

Outer Layer	
Inner diameter [mm]	59.74
Outer diameter [mm]	79.86
Length, coil straight section [m]	16.50
Length, overall [m]	16.75
Cable length [m]	1341
Cable mass [kg]	108
Maximum field [T]	5.6
No. of turns	20
No. of turns, 1st block	5
Wedge mid-thickness (insulated) [mm]	1.90
No. of turns, 2nd block	15
Conductor	
Inner Layer	
Cross section, bare [in.]	0.366 × (0.0625-0.0522)
Keystone [deg.]	1.61
Strand diameter [mm/in.]	0.808/0.0318
No. of strands	23
Strand twist pitch [per cm]	0.4
Cable twist pitch [per cm]	0.126
Copper-to-superconductor ratio	1.3:1
Copper residual resistivity ratio	>80
No. of superconducting filaments	11000
Filament diameter [μm]	5
Strand I_c, 4.2 K and 5 T [A]	613
J_c (non-Cu), 4.2 K and 5 T [A/mm^2]	2400
Cable I_c, 4.2 K and 5 T [A]	11970
Outer Layer	
Cross section, bare [in.]	0.383 × (0.050-0.042)
Keystone [deg.]	1.21
Strand diameter [mm/in.]	0.648/0.0255
No. of strands	30
Strand twist pitch [per cm]	0.4
Cable twist pitch [per cm]	0.136
Copper-to-superconductor ratio	1.8:1
Copper residual resistivity ratio	>90
No. of superconducting filaments	6000
Filament diameter [μm]	5
Strand I_c, 4.2 K and 5 T [A]	282
J_c (non-Cu), 4.2 K and 5 T [A/mm^2]	2400
Cable I_c, 4.2 K and 5 T [A]	7190
Collars	
Material	Nitronic 40
Lamination thickness [mm/in.]	1.52/0.060
Outer diameter [mm]	110.9
Radial thickness, nominal [mm]	15
Minimum stress at 4 K [psi]	3500
Coil Insulation	
Dielectric strength to ground [kV]	5.0
Collar insulation type	Kapton layers
Collar insulation thickness [mm/in.]	0.38/0.015
Inner/outer Kapton [mm/in.]	0.15/0.006
Inner/outer Teflon [mm/in.]	0.08/0.003

Midplane Kapton [mm/in.]	0.20/0.008
Assembly shims [mm/in.]	0.75/0.030

Iron Yoke

Material	low carbon steel
Inner diameter [mm]	111.4
Inner diameter, ends [mm]	175.1
Outer diameter [mm]	266.7
Lamination length, straight section [m]	16.50
Yoke length, overall [m]	16.76
Lamination thickness [mm/in.]	1.524/0.060
No. of laminations	22,000
Weight of iron [kg]	5171
Bus cavity width [mm]	43.18
Bus cavity height [mm]	27.18
No. of bypass holes	4
Diameter of bypass holes [mm]	29

Yoke Containment Structure

Material	304 SS
Outer diameter [mm]	276.2
Wall thickness [mm]	4.7
Weight of shell [kg]	540
Type of yoke survey markers	inserts
Location of markers	45 deg.
No. of markers per magnet	20
Warm-up heater type	band heater
Warm-up heater, kW per dipole	9.6

Cryostat

Vacuum vessel material	steel
Vacuum vessel outer diameter [mm]	609.6
Wall thickness [mm]	6.35
80 K heat shield, outer diameter [mm]	457.2
80 K heat shield thickness [mm]	1.52
20 K shield pipe, inner diameter [mm]	63.5
20 K heat shield, outer diameter [mm]	406.4
20 K heat shield thickness [mm]	1.52
20 K shield pipe, inner diameter [mm]	76.2
He supply pipe, outer diameter [mm]	42.2
He return pipe, outer diameter [mm]	73.0
Superinsulation layers, outside 80 K shield	52
Superinsulation layers, outside 20 K shield	13
Cold mass support type	reentrant post
Support material	F.R.P. unidirectional
Number of supports	5
Support interval [m]	$\sim$3.5
Load per support [kg]	1352
Load per support [kg]	3.5

Electrical System

Main bus stabilization Cu [cm^2]	1.213
Bypass bus stabilization Cu [cm^2]	1.213
Max amps per sq-cm in main bus Cu @ 6500 A	5960
Max amps per sq-cm in bypass bus Cu @ 6500 A	5360
Minimum bus burn-out decay time, sec.	74
Bus expansion joint motion [mm]	$\pm$32.0
Quench heater type	hot-spot foil
Quench heater input, joules/magnet/circuit	1000

Cryogenic System	
Total He mass flow per dipole [g/sec]	100.0
Coil He mass flow per dipole [g/sec]	1.000
Max longitudinal coil ΔT [deg.]	0.090
Pressure drop per magnet [atm.]	0.001
Cold mass support load [watts]	0.12
4.35 K radiation [watts]	0.050
4.35 K interconnections load [watts]	0.050
4.35 K instrumentation leads [watts]	0.10
Total 4.35 K load per dipole [watts]	0.32
Synchrotron load per dipole [watts]	2.34
20 K shield supports [watts]	0.82
20 K radiation per dipole [watts]	2.16
20 K interconnections [watts]	0.10
20 K instrumentation [watts]	0.22
Total 20 K load [watts]	3.3
80 K shield supports [watts]	7.2
80 K shield radiation [watts]	17.7
80 K interconnection [watts]	1.6
80 K instrumentation [watts]	0.5
Total 80 K load [watts]	27.0

One of the major achievements of the R&D program [B.1-4] has been to improve the current-carrying capacity of the NbTi filaments by steadily improving metallurgy and optimized heat treatment procedures, as discussed in Section B.3 and numerous references found therein. As a result, one can expect to consistently achieve a critical current density in the superconductor of at least 2750 A/mm^2 at 4.2 K and 5 T. This value has already been demonstrated in production quantities. By comparison, the specification for the Tevatron conductor (ca. 1980) was 1800 A/mm^2; as late as 1984, a value of 2400 A/mm^2 was assumed as the nominal specification for the SSC Reference Designs Study. In view of the experience with the aforementioned model magnets (see W.S. Gilbert and P. Wanderer, Sections B.14 and B.15), which did not utilize cable incorporating the latest improvements, an operating dipole field of 6.6 T at the operating temperature of 4.35 K can confidentially be projected.

B.1.2 Magnet Description

Coils

The magnetic design is summarized in Section B.2. The superconducting cable is based on NbTi alloy embedded in high-purity copper, drawn into wire, twisted, and wound into a flattened cable which is slightly keystoned and compacted to precise dimensions. The inner coil layer, which is exposed to the highest magnetic field, has 18 turns per half coil and three wedge-shaped spacers in each winding quadrant, as shown in Fig. B.1-1; the spacers are required to properly shape the magnetic field and, with the keystoned cable, provide a "Roman arch" type of coil support. The cable has 23 multifilamentary strands of 0.808 mm (0.0318 in.) diameter each, with a copper-to-superconductor ratio of 1.3:1. The outer coil layer, taking advantage of a lower magnetic field, has 1.3 times higher current density in the superconductor. Here, each half coil has 20 turns with a single wedge per quadrant. The cable has 30 strands of 0.648 mm (0.0255 in.) diameter, with a copper-to-superconductor ratio of 1.8:1. The end turns of each coil contain spacers that minimize field enhancement as well as field harmonics in the magnet end region. The superconducting strands each contain about 10,000 filaments, 5 μm in diameter, to minimize persistent current, or magnetization, effects inherent to superconductors exposed to a changing field. No electrical insulation is needed between strands to suppress eddy currents between them, because the acceleration period, or field rise time, of the collider is long (1000 sec). The finished cable is spiral wrapped, first, with a layer of 0.058 mm thick Kapton film insulation, and next with epoxy-impregnated fiberglass tape (of nominal 0.0508 mm thickness when the winding is under compression). The epoxy serves primarily to hold the coil together during handling in the various magnet assembly steps.

The two inner and two outer coil segments are wound separately on an automatic winding machine, then transferred to a curing press where they are molded to precise dimensions under relatively high temperature and pressure. These operations are delineated in some detail in Section B.5.

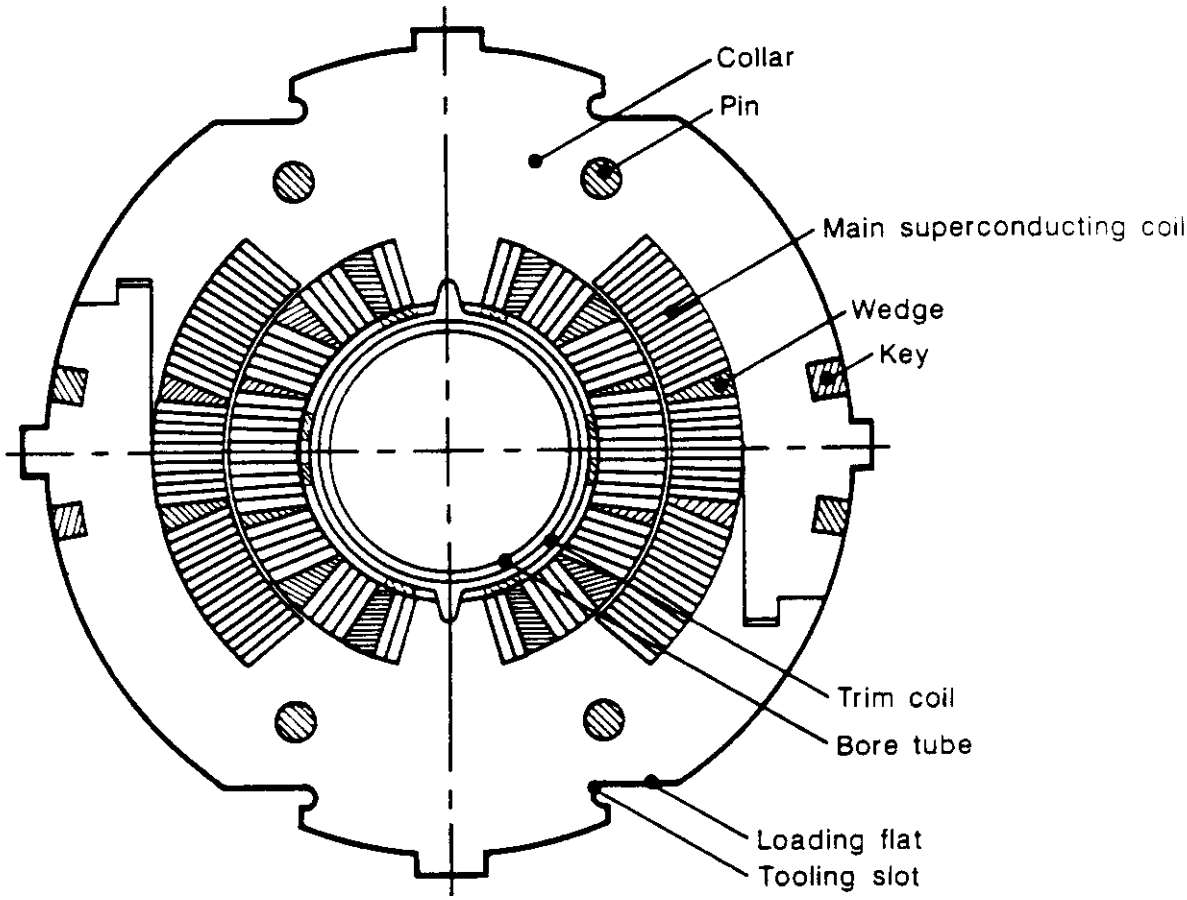

Figure B.1-1. Cross section of collared coils for dipole magnet, showing bore tube, two layer coil, and stainless steel collars.

Bore Tube and Correction Coils

Next, the coils are assembled around a stainless steel bore tube of 32-mm inner diameter. Between the inner and outer coil layers are inserted sheets of Kapton and Teflon, the latter acting as a slip-plane to reduce friction in case of conductor motion when the magnet is energized. There is Kapton insulation on the mid-plane as well. The bore tube, 1.0 mm thick, is plated on its interior with high-purity copper to provide a low impendance path for currents induced by the circulating beam. Its outer surface is covered, first, with a double layer of Kapton bonded with Teflon, each layer 0.025 mm thick. Next, it receives a Kapton-Teflon substrate, 0.10 mm thick, on top of which is located a very thin composite (sextupole and decapole) winding of 0.012 in. diameter superconducting wires. The multipole pattern is produced by embedding the superconducting wire in a Kapton sheet by an automatic technique akin to printed circuit fabrication.

The correction coils compensate for distortions in the field caused by magnetization currents induced in the superconducting filaments of the main dipole winding at low (injection) field and by saturation of the iron yoke near maximum field. (Both are relatively minor effects, as a consequence of the fine superconducting filaments and the presence of non-magnetic collars between the dipole coil and iron yoke.) They are keyed to the pole spacers of the external dipole coil to maintain orientation of the multipole fields with respect to the primary vertical dipole field. Because this winding covers the entire magnet length, the compensation is exact. These trim coils are discussed in Section B.8. (The extensive array of correction elements grouped together at each quadrupole location in the lattice are not as effective for compensation of these particular distortions.) The trim coils are secured to the bore tube with two layers of Kevlar cord (each 0.127 mm thick) and Kapton coated with Teflon (three layers, each 0.025 mm thick), and the entire bore tube assembly (Fig. B.1-2) is accurately centered within the dipole winding by longitudinal G-10 spacers (1.4 mm thick) which also define helium cooling passages.

Collars

A system of precision non-magnetic, interlocking collars, 15 mm in radial dimension and locked together with close-fitting keys, as shown in Fig. B.1-1, provides substantial compression of the coils at assembly; the collars maintain precise location to ensure magnetic field uniformity and also contain the strong Lorentz forces (43,000 Nt/m) generated at maximum field (6.6 T) and current (6.5 kA). Collar analysis and design considerations are discussed, in some detail, in Section B.6, and further summarized in Section B.7. The windings are fully self-supporting on their inside surface because of the Roman arch geometry noted earlier. The four coil segments are connected in series, with two electrical leads (and trim coil leads) emerging from the magnet at one end. The coils are insulated from the collars by several interleaved layers of Kapton sheet, providing dielectric strength to resist 5 kV to ground.

An important feature of the collaring technique is that it provides an intermediate assembly step where the electrical integrity of the Kapton insulation and the harmonic content of the field produced by this subassembly can be checked before further effort is invested in the construction of the magnet. The harmonic measurements will be made by a rotating coil in the collared coil at room temperature.

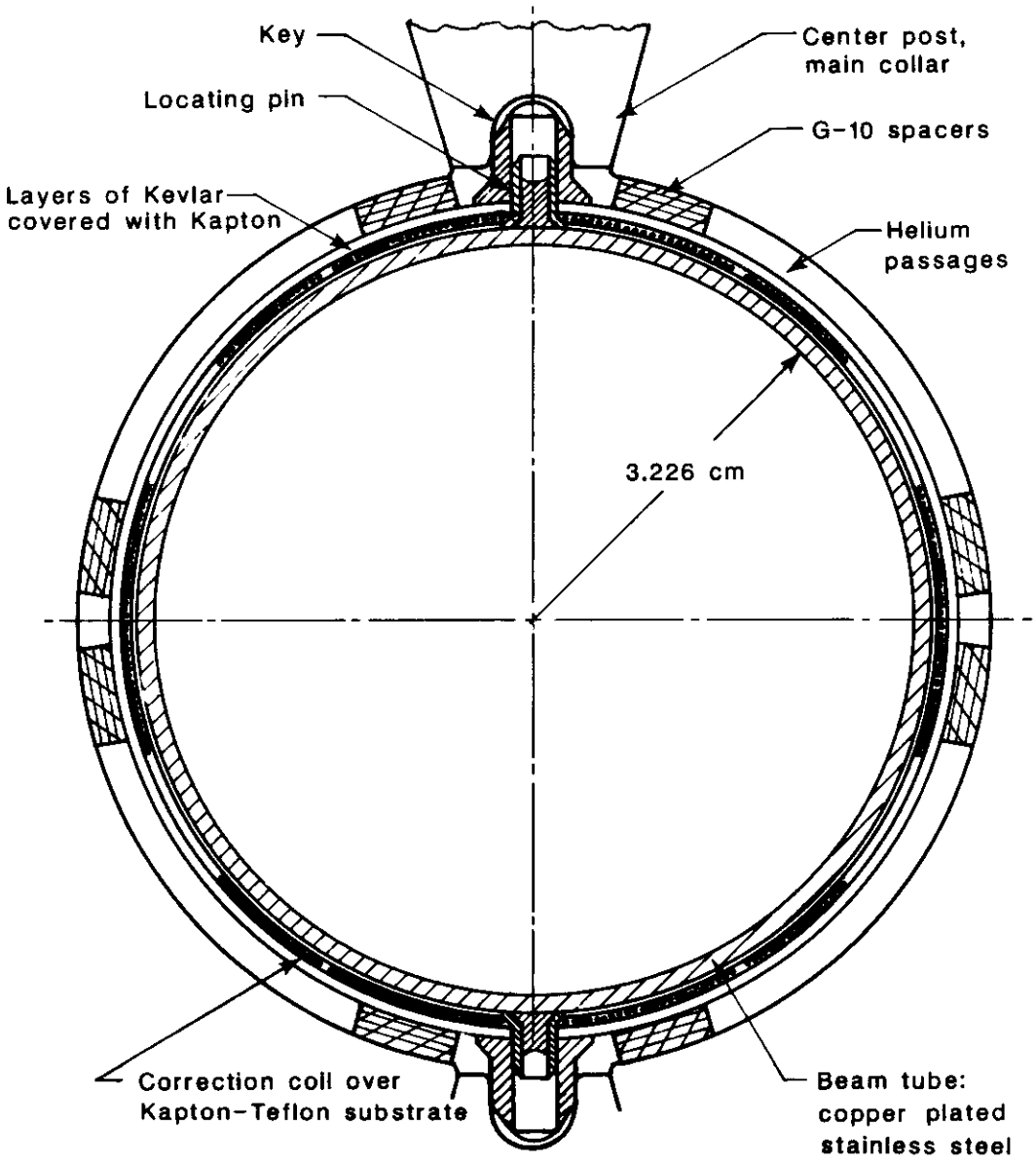

Figure B.1-2. Bore tube assembly, including copper-plated beam tube, sextupole correction coil, and G-10 spacers. The spacers define cooling passages, and ensure that the assembly is concentrically positioned with respect to the main dipole coil. Also shown is the method for keying the trim coil to the dipole center post.

Yoke

The self-supporting coil assembly is suspended via four tabs that are part of the collars, in a laminated, split-iron yoke of 26.67 cm o.d. (Fig. B.1-3). The iron provides the magnetic function of a flux return path, contributes about 1.7 T at maximum operating field, and acts as a shield to minimize the stray magnetic field of the dipole. The iron yoke also ensures rigid alignment of the collared coil assembly (the key tabs register the collared coil assembly in the yoke to an angular tolerance of ± 0.5 mrad), and provides the primary passages for the helium coolant (the four large symmetrically placed holes in Fig. B.1-3). The laminations are die-punched from 1.5 mm thick low carbon, cold-rolled steel possessing magnetic properties typical of those required for accelerators; e.g., low coercive force, high permeability at both high and low induction, and high saturation induction. Longitudinal slots in the yoke provide conduits for the electrical bus between magnets (main dipole bus in top slot, correction coil leads in bottom slot). A 4.7-mm thick close-fitting stainless steel yoke-support shell, welded from two half-shells by a seam along the horizontal mid-plane, also provides (with the bore tube and end plates) a vacuum-tight enclosure for the pressurized helium coolant.

Support Posts

The collared coil assembly, with iron yoke and yoke support shell—the "cold mass"—weighs approximately 7000 kg. It is supported by five hollow posts inside a cryostat assembly (Fig. B.1-4) providing space for heat shields, thermal insulation, and cryogenic headers, all mounted within a cylindrical vacuum vessel. The cryostat and the support system are described in Section B.13. Each support post is a nested pair of thin-wall fiberglass-reinforced plastic tubes loaded in compression. One tube is fastened at the top to the cold mass at 4.35 K and extends through rings supporting the 20 and 80 K heat shields, successively; the outer, shorter tube supports the load at 80 K and rests on the magnet base at room temperature. Models of this design configuration have performed well under all expected mechanical loading conditions. Moreover, the measured heat leak is close to the predicted value. Thus, the five supports together contribute a heat leak of about 0.1 watt to the 4.35 K assembly, or about 5% of the total 4.35 K load from all sources.

The center post is rigidly connected to the cold mass, while the other supports can slide axially to accommodate thermal contraction. When the posts are attached to the cold mass, their positions are carefully adjusted with special tooling; thus, the magnet (bore tube) location, including the required sagitta, is determined prior to final cryostat assembly and magnet installation. Aluminum heat shields are supported by the posts in a manner such that their thermal distortion can be accommodated without overloading the posts. The 20 K shield is integral with an aluminum pipe cooled by helium gas; another aluminum pipe, carrying gas returning to the refrigerator, is also supported by the posts. A further aluminum tube, attached to the outer 80 K heat shield, is cooled by nitrogen gas. Thermal connections between heat shields and their support rings (heat intercepts) are flexible metallic straps. The fourth pipe in the cryostat is a 4.35 K helium return pipe.

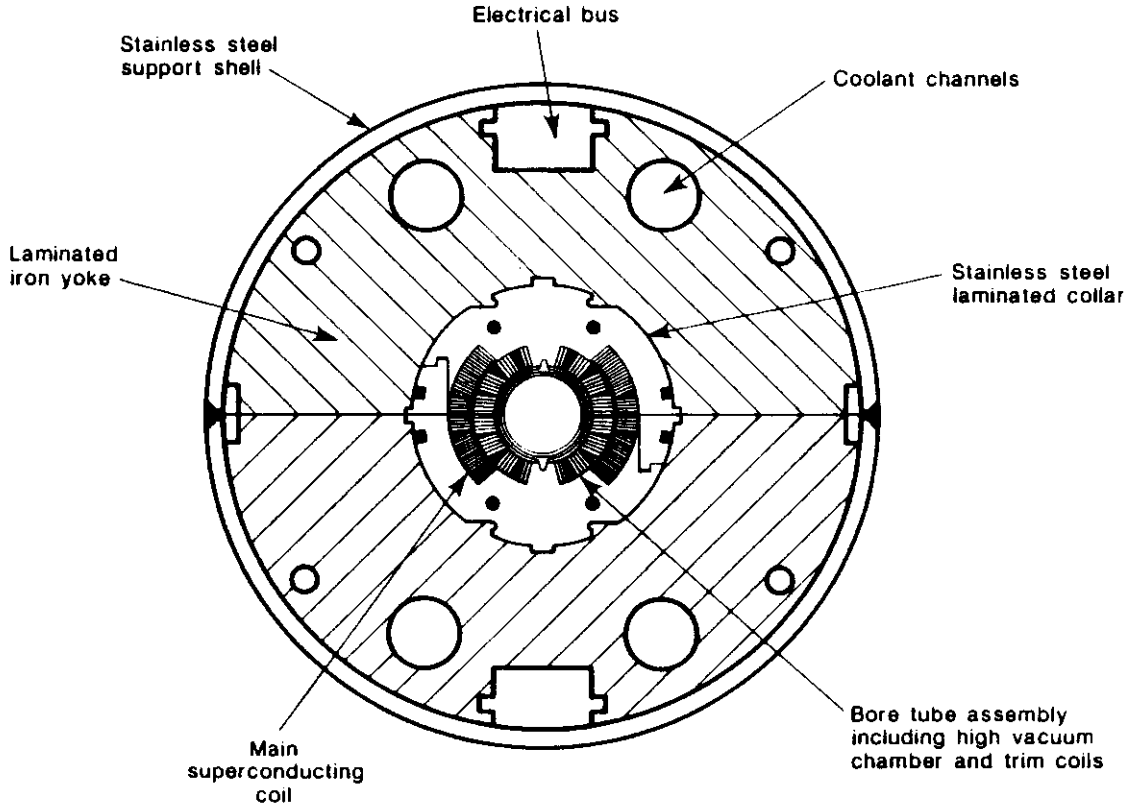

Figure B.1-3. Cross section of dipole magnet, including iron yoke and yoke support tube.

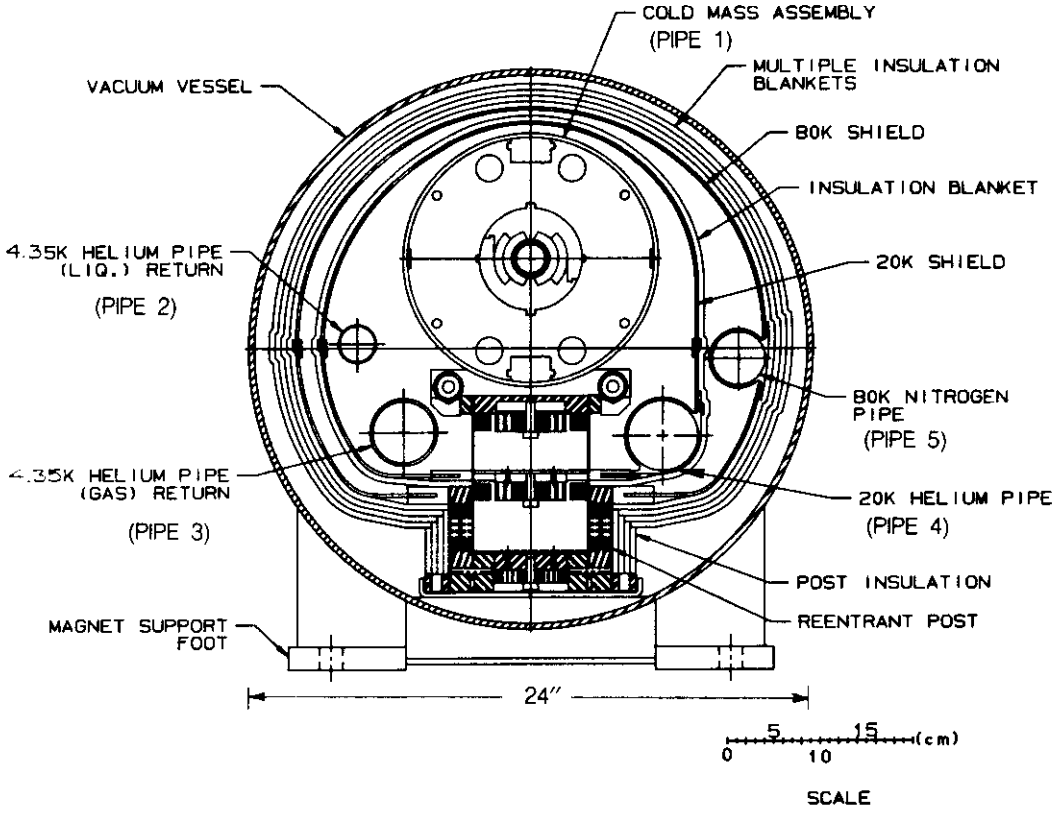

Figure B.1-4. Cross section of cryostat, showing dipole (cold mass), heat shields with thermal insulation blankets, cryogenic headers, reentrant support post, and external vacuum vessel.

Magnet Assembly

The cold mass with posts, heat shields, thermal insulation in the form of blankets of aluminized polyester film interleaved with fiberglass mat spacers (one blanket around the 20 K shield, four around the 80 K shield), and cryogenic piping attached, is inserted into the vacuum vessel (60.96 cm outer diameter) with the aid of special rolling cradles and rails. The post support plate is then bolted to the magnet support feet of the vacuum vessel. For shipping, close-fitting, removable restraints are inserted in the hollow center section of each post; these allow axial and transverse loads from shipping and handling to be transmitted directly to the support feet without overloading the thin-walled reentrant posts.

In the magnet-to-magnet interconnection region, all cryogenic tubes are joined with bellows to accommodate axial thermal motion, including large-diameter bellows connecting the yoke support shells enclosing the cold mass assembly, and even larger bellows joining the outer vacuum vessels. All connections are made with automatic welding equipment. The bellows connecting bore tube sections are of the double wall type incorporating a "guard vacuum" space pumped by a connection to the insulating vacuum system. The interconnections include the magnet-to-magnet electrical bus (main bus as well as trim coil bus), leads connecting the quench protection strip heaters embedded in the Kapton ground insulation over the outer coil, and various instrumentation leads. Considerations governing the design of the bus work are discussed in Section B.9.

Quench Protection

In the active magnet quench protection system of the present design, the outer coil layer of a quenching magnet will be driven normal by discharging a capacitor bank into the stainless steel heater strips. The inner coils follow soon thereafter. (Two of the four heaters are spare elements.) In this way the normal resistive zone is accelerated, ensuring that the magnet's energy is distributed rapidly over a large coil volume to prevent local overheating of the conductor. The use of active heaters avoids the alternative need for passive quench protection diodes in each magnet; diodes may be vulnerable to neutron radiation during machine operation. However, recent studies have shown that the Cu:SC ratio of the conductor, and thus the margin against overheating, is quite conservative, implying that a passive quench protection system is also quite feasible.

References

B.1-1. R. Palmer and A. Tollestrup, Annual Review of Nuclear and Particle Science, **34** (1984), 247–284.

B.1-2. H.T. Edwards, Annual Review of Nuclear and Particle Science, **35** (1985), 605–660.

B.1-3. P. Dahl et al., Proc. 9th Int. Conf. on Magnet Technology (Zurich, 1985), 80–83. P.J. Reardon, IEEE Transactions on Nuclear Science, **NS-32** (1985), 3466–3470.

B.1-4. A.F. Greene, D.C. Larbalestier, W.B. Sampson, and R. Scanlan, "Status of Superconducting Development for the SSC Design D Dipole," SSC Central Design Group Report SSC-N-64 (1985).

B.2 NC515 — A New Dipole Cross Section for SSC

S. Caspi, M. Helm, L.J. Laslett, and C. Taylor
Lawrence Berkeley Laboratory

March 1986

B.2.1 Introduction

A new dipole cross section for the SSC is outlined which has multipole coefficients of less than 1.0×10^{-6} of the dipole field (or 0.01 units) at 1.0 cm. This cross section has four conductor blocks (three wedges, sixteen turns) in the inner layer and two conductor blocks (one wedge, twenty turns) in the outer layer. The two layers were formed from the same types of "partially-keystoned" cable used in model magnets at LBL and BNL. Based on the present cable design an operating field of 6.6 T at 4.35 K is chosen. The new cross section "NC515" is shown in Figs. B.2-1 and B.2-2, and the multipoles (for μ-infinite in iron) are listed in Table B.2-1.

Table B.2-1
Multipoles for Dipole NC515*

n	0	2	4	6	8	10
b_n	1.0	-1.8×10^{-8}	-8.5×10^{-8}	-4.9×10^{-7}	-1.4×10^{-6}	1.1×10^{-6}

*Multipole coefficients evaluated at 1.0 cm.

B.2.2 Magnet Design

Discussions with the SSC Central Design Group suggested that we attempt to redesign dipole magnet C5 (the dipole design used thus far in model dipoles for Reference Design D) so that higher multipoles—b_8 (18-pole) and above—are less than 0.2 units of the dipole field at a radius of 1.0 cm. Also, we have increased the midplane insulation thickness from 4 mil, used in current model magnets, to 8 mil (not including conductor insulation). Using this new design, model magnets can be constructed with the available collars, which was a desired but not necessary consideration. Also, the wedge shape is constrained to stay above a minimum practical size at its "pointed" end to permit precise positioning and to avoid

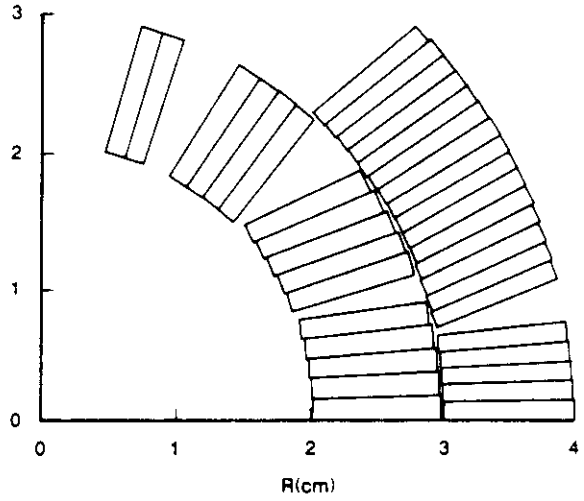

Figure B.2-1. A quadrant cross section of NC515, a 4-wedge solution.

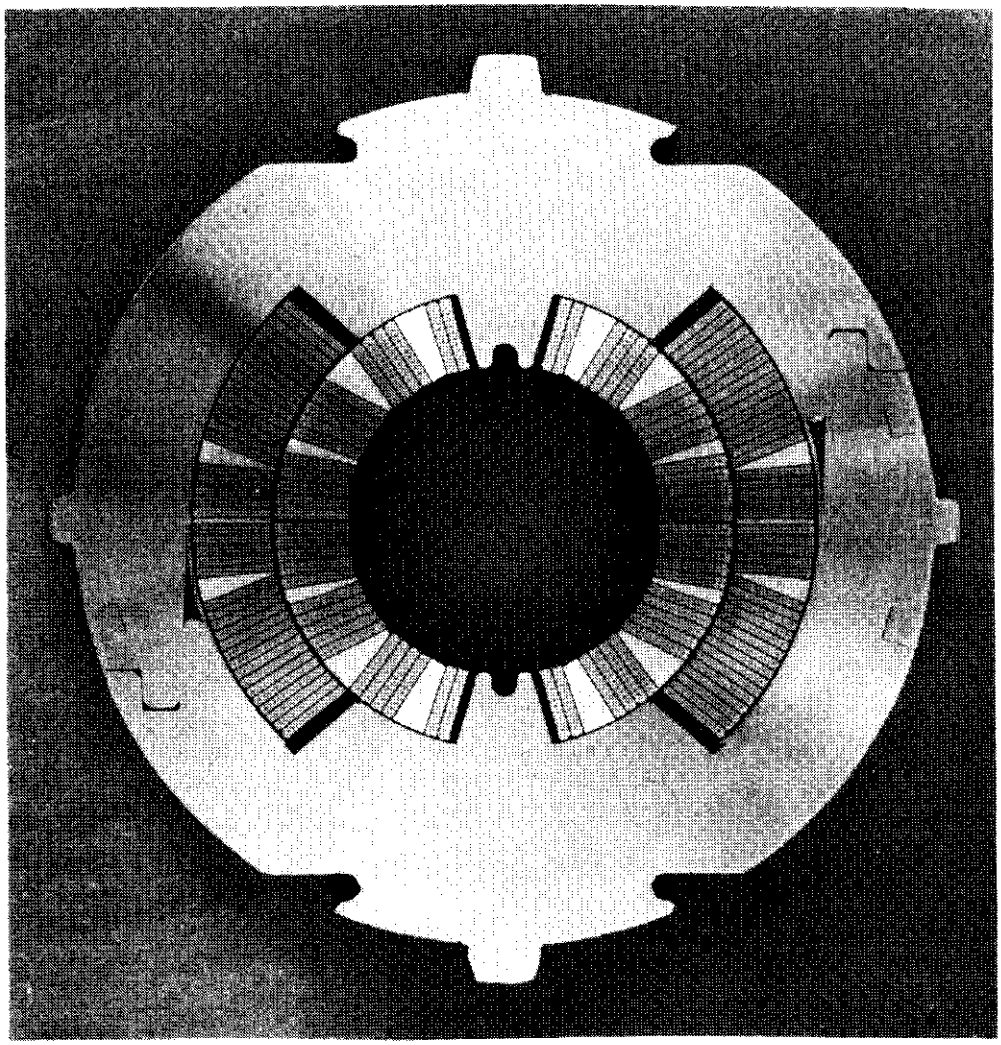

Figure B.2-2. A model cross section of NC515.

sharp edges. The character of this new design and steps taken to develop it are outlined in the remainder of this report.

The BNL program PARTIALKEYSTONE, was available to search for "good" (low multipole value) cross sections. We modified PARTIALKEYSTONE so that current blocks may deviate from a purely radial orientation. We also developed independent techniques for providing PARTIALKEYSTONE with preliminary cross-sections for optimization. We realized that there are many solutions that are "good" but differ very much in their geometry, and that at which one of these "good" solutions PARTIALKEYSTONE arrives depends on where it starts out. We therefore used some assumptions to choose starting points likely to result in "good" designs. For further information, see Ref. B.2-1.

Using the modified PARTIALKEYSTONE, we examined several families of three-wedge cross sections. For mechanical and magnetic considerations an additional wedge was introduced into the inner layer of a particularly promising cross section (four wedges in all). Optimization of this four-wedge case yielded a solution with a better field quality than had been found in any of the three-wedge cases. By restricting the number of turns in the outer layer of this case to twenty, and moving the position of the outer-layer wedge, a cross section with low multipole values and acceptable pole angles was found. This design is NC515 (Fig. B.2-1).

We used the computer program POISSON to study the effects iron saturation and current distribution have on the harmonic content of NC515, refinements not available in PARTIALKEYSTONE. Several POISSON runs were made using a cross section very closely approximating NC515 (in POISSON, it is difficult to model individual turns inside conductor blocks). We modeled two different current distributions. In the Constant Density model, each block of conductor is assumed to have a constant current density (the same assumption used by PARTIALKEYSTONE). A better approximation to the distribution of current in the conductor is the Split Density model, where each layer of conductor is divided radially in half, and each half assigned half the total current; the number of strands is assumed to be equal in each half, while the effective cross-sectional area per strand differs radially due to keystoning. The difference between these two models is shown in Table B.2-2.

Table B.2-2
Difference in Multipoles between Split Density and Constant Density Models (at 1 cm)

	(10^{-4} dipole units)			
Multipoles	b_2	b_4	b_6	b_8
b_n (S.D.)-b_n (C.D.)	−3.76	−0.75	−0.145	−0.011

Since we felt the Split Density model to be more accurate than the Constant Density model, we designed a slightly revised cross-section geometry to compensate for the

multipole differences between them. We asked PARTIALKEYSTONE to optimize the wedge dimensions to arrive at a solution where the first four multipoles are the inverse of those in Table B.2-2. This revised cross-section geometry, NC515AUG, should result in a magnet with very low multipoles.

B.2.3 Operating Field

It is difficult to predict precisely the critical current of a magnet since the conditions under which a cable in the magnet "quenches" cannot be duplicated in tests of short sections of cable. However, observation of critical current achieved in Design D model magnets at BNL and LBL constructed of cable with varying strand current density, indicates that an operating current density, J_o of 80% of the uncabled strand current density J_c, is a reasonable design value. This allows for some degradation during cabling and some operating margin. J_c is determined at the maximum field value calculated at the edge of the cable and at the maximum operating temperature of 4.35 K provided by the helium coolant. The cable properties are described in Table B.2-3.

Table B.2-3

	Inner Layer	Outer Layer
Strand diameter	0.0808 cm	0.0648 cm
Number of strands	23	30
Copper to superconductor ratio	1.3	1.8
Cable dimensions (including insulation) used in the calculation		
Cable width	0.9627 cm	1.0058 cm
Cable thickness (nominal)	0.1605 cm	0.1345 cm
Cable keystone	0.0272 cm	0.0211 cm
Inner radius	2.0193 cm	3.0074 cm
Outer radius	2.9820 cm	4.0132 cm

In addition to these mechanical specifications, the minimum critical current of the strands is characterized by J_c of 2750/A/mm^2 at 4.22 K, 5 T, and $\rho = 10^{-14}$ Ω-m. Scaling of J_c with temperature and field is done using the following relationship.

$$J_c(T,B) = P_1 \left[1 - \frac{T-4.2}{P_2 - P_3 B} \right] \left[1 + P_4 B \right]$$

where [B.2-2]

$$P_1 = 5509.72 \frac{J_c(4.22K, 5T)}{2750}$$

$|J_c\ (4.22\ K,\ 5T) = 2750\ \text{A/mm}^2$ for this design, as cited above|

$$P_2 = 7.81042$$

$$P_3 = 0.778448$$

$$P_4 = -0.996643$$

Table B.2-4 gives the operating conditions for the magnet at 4.35 K and at 4.50 K for equivalent operating margin, J_c/J_o. (Current density, J, is in A/mm^2.)

Table B.2-4

			Inner Coil				Outer Coil			
$T(K)$	$B_o(T)$	$I(A)$	B_{max}	J_o	J_c	J_c/J_o	B_{max}	J_o	J_c	J_c/J_o
4.35	6.595	6485	6.961	1265	1581	1.250	5.566	1837	2347	1.278
4.50	6.466	6357	6.825	1241	1550	1.250	5.457	1801	2301	1.278

Table B.2-4 shows that the inner and outer cables are reasonably well balanced, with the inner coil having slightly less operating margin than the outer coil; however, this small difference is not significant compared with other variations in cable behavior that affect maximum operating field. Therefore, at 4.35 T, the operating field is chosen to be 6.6 T for cross section NC515; other cross sections would result in variations from this depending on details of magnetic field in the windings.

B.2.4 Effect of Real Iron

We have calculated the effect of iron saturation on the multipoles for various field levels and, also, the effect of iron stacking factors of 1.0 and 0.97. These calculations used the NC515 cross section and iron with 11.14 cm i.d., 26.66 cm o.d., and no holes. A tabulation of these results for the first four multipoles is given in Table B.2-5, and a plot of sextupole versus field level (including stacking factor = 1.0 and 0.97) is given in Fig. B.2-3. Included in Fig. B.2-4 are the geometry and flux plot for NC515 solved by POISSON. Note that each layer was split in half as an approximation to the radial current distribution due to keystoning. Table B.2-5 assumes that a perfect dipole exists at low field (with real iron), i.e., all multipole coefficients become equal to zero at $B_o = -0.6597$ T. The values in

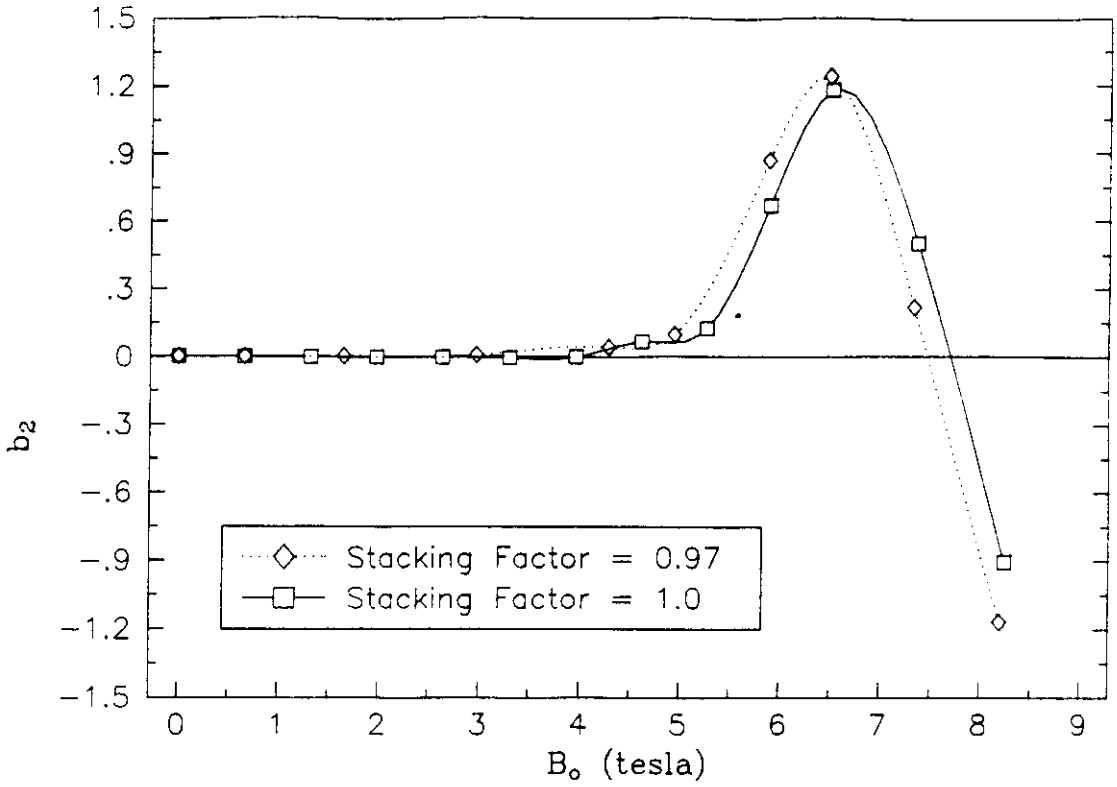

Figure B.2-3. Sextupole coefficient in units of 10^{-4} cm^{-2} as a function of the dipole field for real iron, 266.7 mm outer diameter.

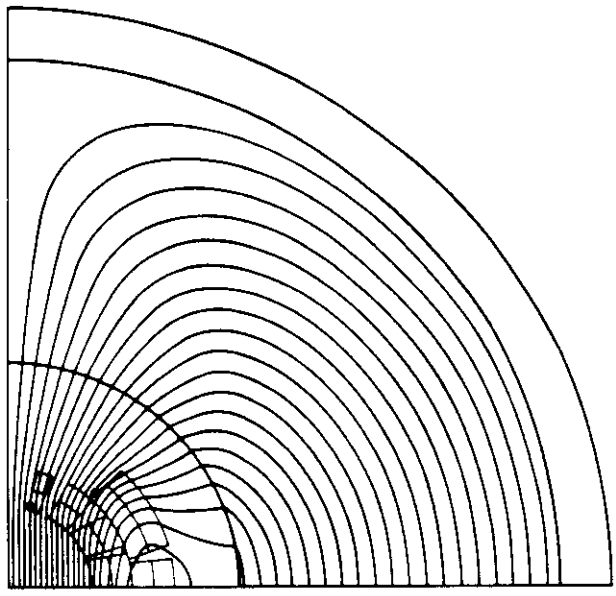

Figure B.2-4. Flux plot of NC515 solved by POISSON. Inner coil radius 20.193 mm, outer coil radius 40.132 mm, iron inner radius 55.70 mm, iron outer radius 133.30 mm.

Table B.2-5, accordingly, have been normalized by subtracting the multipoles for the high field cases from the corresponding values in the low field (perfect dipole) case. In Table B.2-6 are shown the values and locations of the maximum field in each layer for a case where B_o = 6.5 T, with transfer functions and stored energy in Table B.2-7. Note that this energy is for the full cross-section, per unit length. The coil inductance at 6400 A is computed to be 3.146 mHy/m.

Table B.2-5
Effect of Iron Saturation on Multipoles
(Coefficients in units of 10^{-4} cm^{-n})

Current (A)	Field (T)	b_2	b_4	b_6	b_8
640.0	−0.66	0.0	0.0	0.0	0.0
1280.0	−1.32	−0.0005	−0.0089	−0.0089	0.0171
1920.0	−1.98	−0.0017	−0.0090	−0.0089	0.0172
2560.0	−2.64	−0.0043	−0.0090	−0.0089	0.0172
3200.0	−3.30	−0.0074	−0.0090	−0.0089	0.0172
3840.0	−3.96	−0.0007	−0.0094	−0.0089	0.0172
4480.0	−4.62	0.0666	−0.0109	−0.0089	0.0172
5120.0	−5.27	0.1251	−0.019	−0.0095	0.0172
5760.0	−5.90	0.669	−0.035	−0.010	0.0180
6400.0	−6.51	1.1793	−0.0512	−0.0137	0.0168
7360.0	−7.37	0.5008	−0.0837	−0.0149	0.0199
8384.0	−8.24	−0.905	−0.1203	−0.0189	0.0209

Table B.2-6
Peak Field Locations
(B = 6.5 T)

μ	Layer	X (cm)	Y (cm)	B_{max}/B_o
infinite	inner	0.44	2.02	1.0497
	outer	2.20	2.50	0.842
real iron	inner	0.45	2.15	1.0555
	outer	2.15	2.45	0.844

Table B.2-7
Transfer Function and Stored Energy

B_o (T)	Transfer function (G/A)	Stored Energy (kJ/m)
$\mu = \infty$ (6400 A)	10.316	—
1.32	10.309	2.62
6.5 (6400 A)	10.172	64.42

References

B.2-1. S. Caspi, M. Helm, L.J. Laslett, and C. Taylor, SSC Technical Note SSC-Mag-64 (January 1986).

B.2-2. This linear relationship is accurate within the range of this design. (M. McAshan, personal communication).

B.3 Superconductor: Conductor Development, Final Specifications

A.F. Greene
Brookhaven National Laboratory

D.C. Larbalestier
University of Wisconsin, Madison

and

R. Scanlan
Lawrence Berkeley Laboratory

March 1986

B.3.1 Rationale for Choice of NbTi; Survey of High Field Superconductors

In this section we present a survey of high field superconductors which could possibly be used in accelerator dipole magnets, and then we rank these candidates with respect to ease of fabrication and cost as well as superconducting properties. We will present only a summary of results; references will be listed for those who wish more detail. The superconducting properties [B.3-1] which are important for applications involving electromagnets are transition temperature, T_c, upper critical field, H_{c2}, and critical current density, J_c. The first two are often referred to as "intrinsic" properties because they are determined by the chemical composition and are not strongly dependent on the microstructure, as is the case for J_c. The relationship between H_{c2} and T_c for many potentially useful high field superconductors is shown in Fig. B.3-1. However, in addition to these properties, the superconductor must have a high J_c and also be capable of manufacture at a reasonable cost.

A major difference between NbTi and the other superconductors shown in Fig. B.3-1 is its ease of fabrication. NbTi is a ductile alloy which can be processed from cm-size rods to micron-size filaments by standard extrusion and cold drawing techniques (Fig. B.3-2). On the other hand, the other materials in Fig. B.3-1 are intermetallic compounds which can be deformed only about 0.2% in order to utilize them in the form of continuous multifilamentary superconductors; a number of special fabrication techniques have been developed [B.3-1, B.3-2]. Within the group of intermetallic compound superconductors, fabrication technology is most advanced for Nb_3Sn. (See Table B.3-1.)

Several processes have been developed which allow Nb filaments to be fabricated and then converted to Nb_3Sn after mechanical deformation is complete. In the first, called the "bronze process" (Fig. B.3-3), Nb filaments are processed in a bronze (Cu-13 wt % Sn)

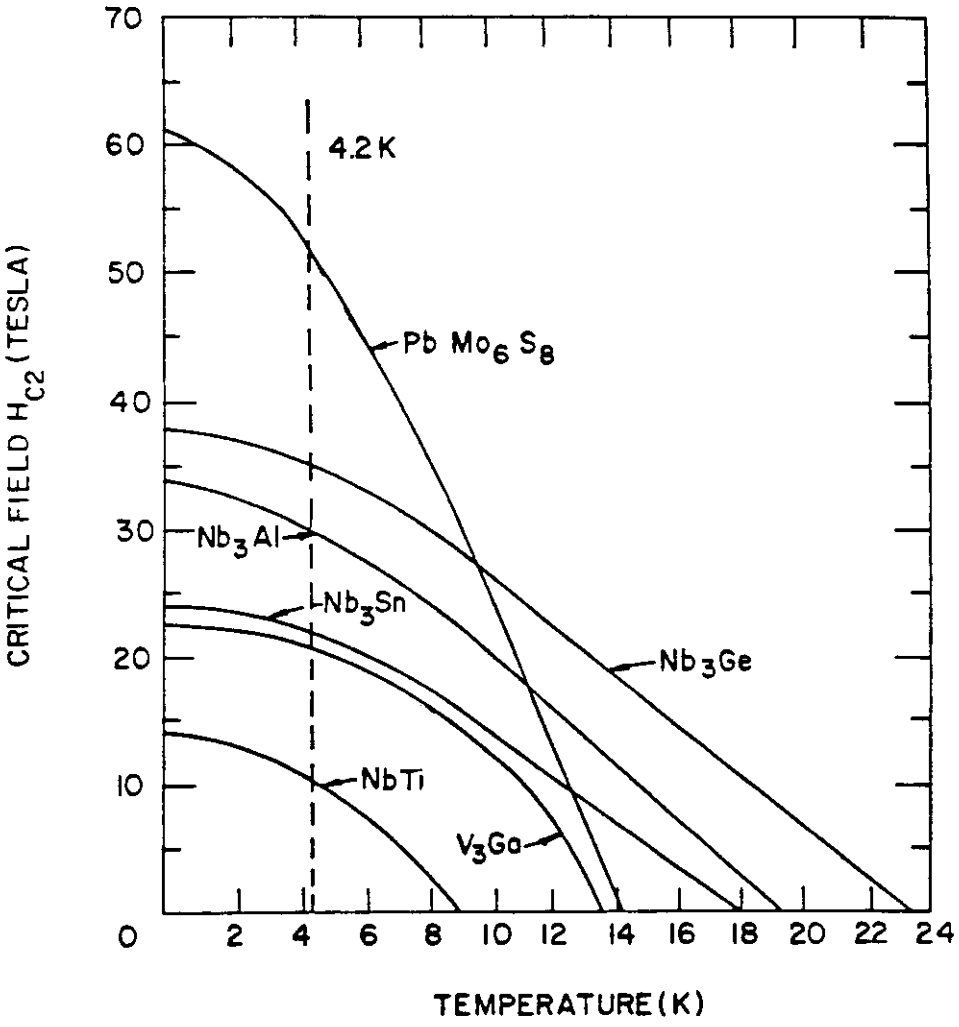

Figure B.3-1. Critical field versus temperature for various high field superconducting materials.

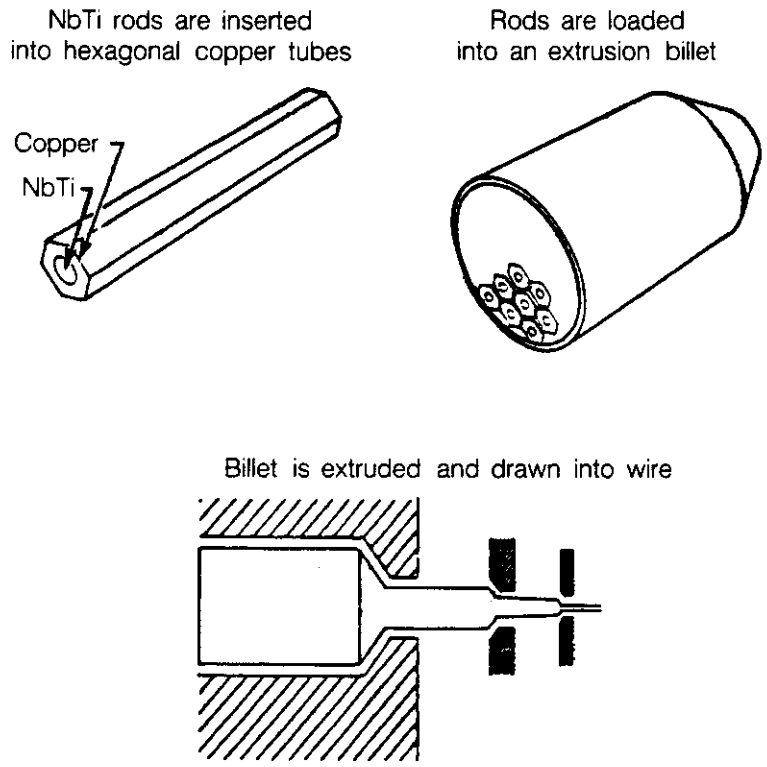

Figure B.3-2. Schematic diagram of the NbTi wire fabrication method.

Table B.3-1
Fine Multifilament Superconductor Fabrication Techniques

Material	Mechanical Properties	Fabrication Process	Remarks
NbTi	Very ductile	Conventional hot extrusion or hydrostatic extrusion followed by cold drawing	Versatile, cost effective processing
Nb_3Sn	0.2% tensile strain limit before fracture	"Bronze" process	Many intermediate anneals are necessary
		"Internal tin" process	Redistribution of tin necessary before conversion into Nb_3Sn
V_3Ga	0.2% tensile strain limit before fracture	"Bronze" process	Best properties with V-Ga alloy rods
Nb_3Al	0.2% tensile strain	Nb, Al powder process	Lab scale demonstration only, high purity powders, good Q.C. required, filaments may be electrically coupled.
$PbMo_6S_8$	0.2% tensile strain	Mo, MoS_2, PbS powders	Lab scale demonstration only, high purity powders, good Q.C. required; filaments may be electrically coupled.

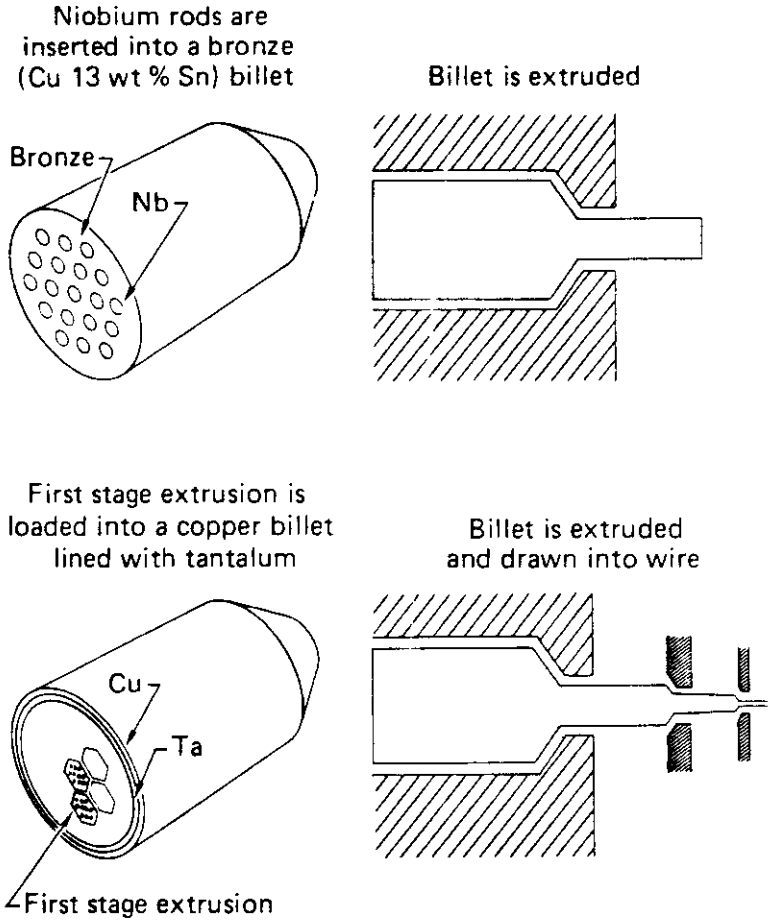

Figure B.3-3. Schematic diagram of the Nb_3Sn "bronze process" wire fabrication method.

matrix and then reacted typically at 650–750°C for 10–100 hrs to form the Nb_3Sn superconductor. This process is well established in industry and has been used to fabricate about 10 tons of superconductor compound, primarily for fusion research magnets [B.3-3, B.3-4, B.3-5]. Note, however, that this amount is still small in comparison with the quantity necessary for an accelerator the size of the SSC, i.e., between 250 and 500 tons of Nb_3Sn compound, depending on operating fields. (See Table B.3-2.) Two major limitations of this process are (1) the limited ductility of bronze requires many costly intermediate annealing steps during wire drawing, and (2) the need to co-process with bronze means that the overall current density is reduced. Alternate processes are under development, the most advanced of which is the "internal tin process" (Fig. B.3-4) in which pure or low-alloy Sn is co-processed with Cu and Nb. Problems associated with bronze processing, such as limits on Sn content, limited ductility, and the risk of Nb_3Sn formation during bronze annealing, are avoided. Approximately 1 ton of material has been processed using this technique and several fabrication problems have been identified. Another fabrication approach [B.3-7] which is under development utilizies Nb tubes filled with $NbSn_2$ powder or alloyed Sn; the material is processed to wire and the powder or Sn reacted with the Nb tube wall to produce Nb_3Sn. Although laboratory processing has produced approximately 100 lbs. of material with very good J_c values, many production problems remain, such as quality control on the powder and limits on filament diameters achievable using a tube approach.

The time scale for the evolution of these processes for fabrication of multifilamentary Nb_3Sn has been quite long; the bronze process was initially proposed about 1970, [B.3-8, B.3-9] the Nb tube-$NbSn_2$ powder process in 1975 [B.3-7] and the internal tin process in 1974 [B.3-10]. The long development time is due in part to the rather complex and lengthy processing required for Nb_3Sn and, in part, to the lack of a strong demand for this type of conductor. As a result, the industrial base does not appear adequate for producing the 250–500 tons of Nb_3Sn compound (1000–2000 tons of wire) which would be required to begin construction of the SSC in 1988.

On the other hand, the industrial fabrication of NbTi is well developed with about 35 tons/yr [B.3-11] being produced, largely for NMR tomography applications. In addition, recent results from the SSC related R&D program [B.3-12, B.3-13, B.3-14] show that significant improvements in NbTi are possible. As shown in Fig. B.3-5, the critical current density J_c (5.0 T, 4.2 K) achievable in production-size billets has been increased from about 1800–2000 A/mm^2 (typical for the Tevatron and CBA conductor procurements), to 2400–2750 A/mm^2 for SSC R&D procurements. More recent results [B.13-15] with an R&D billet indicate that values as high as 3000 A/mm^2 are possible.

Comparison of Performance of Nb_3Sn with NbTi for SSC Design D Magnets

Of primary interest in the evaluation of different superconductor materials is the performance in an SSC magnet design. Figure B.3-6 attempts to provide such an evaluation. Here we have shown the critical current performance for NbTi based on a wire current density of 2750 A/mm^2 at 4.2 K, 5 T. These data have been plotted at fields from 3 to 8 T using a field enhancement factor in the magnet of $1.045 \times B_o$, and have been adjusted for the magnet operating temperature of 4.35 K.

The Nb_3Sn critical current line has been plotted using the same field enhancement and temperature correction; it has been normalized to J_c = 865 A/mm^2 at 4.2 K, 10 T. This J_c is the value measured for strand fabricated using the internal tin process with filament

Table B.3-2
Production Status of Superconductors

	Ease of Fabrication	Quantities of Alloy or Superconductor Compounds Produced	Present Cost
NbTi	Excellent (ductile alloy, compatible with Cu)	Present rate 35 tons/yr NMR HERA requirement 50 tons	$60–$80/lb
NbTiTa	Good, but not as ductile as NbTi	<1 ton	$150/lb
Nb_3Sn	Special fabrication techniques are necessary to avoid brittle phase	4 tons MFTF, HFTF 5 tons LCP	$250–$600/lb
V_3Ga	Special fabrication techniques are necessary to avoid brittle phase	Approximately 100 kg	$1000/lb
Nb_3Al	Special fabrication techniques are necessary to avoid brittle phase	Approximately 20 kg	

Note: SSC requirements for 6.6 T magnets are ~2000 tons of NbTi wire or ~800 tons of NbTi alloy.

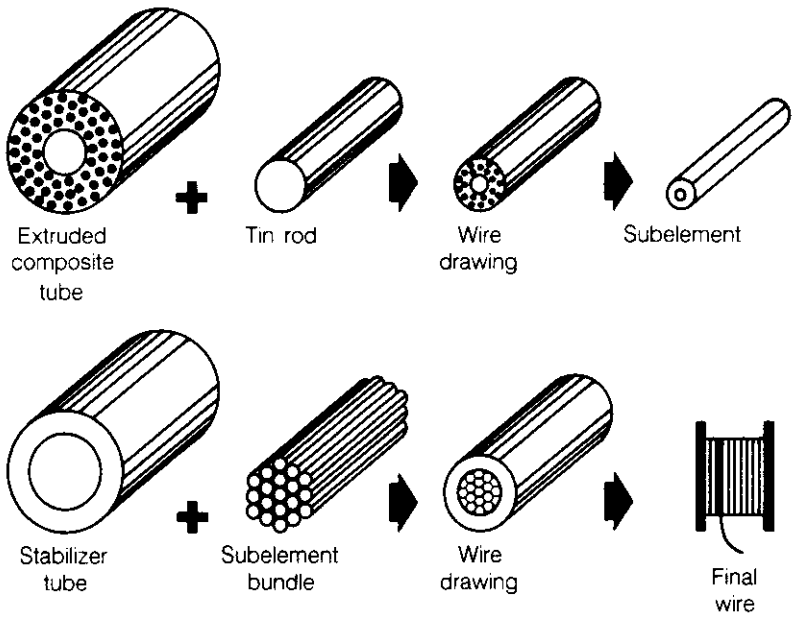

Figure B.3-4. Schematic diagram of the Nb_3SN "internal tin process" wire fabrication method.

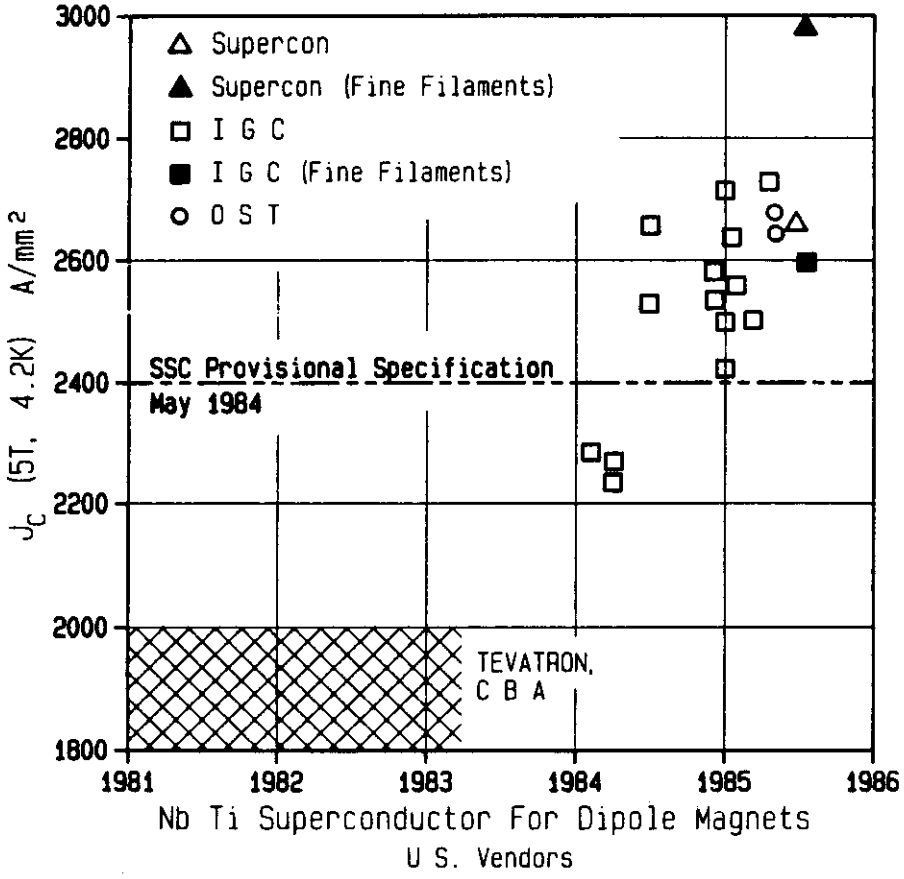

Figure B.3-5. Improvement in the current density of NbTi superconducting wire.

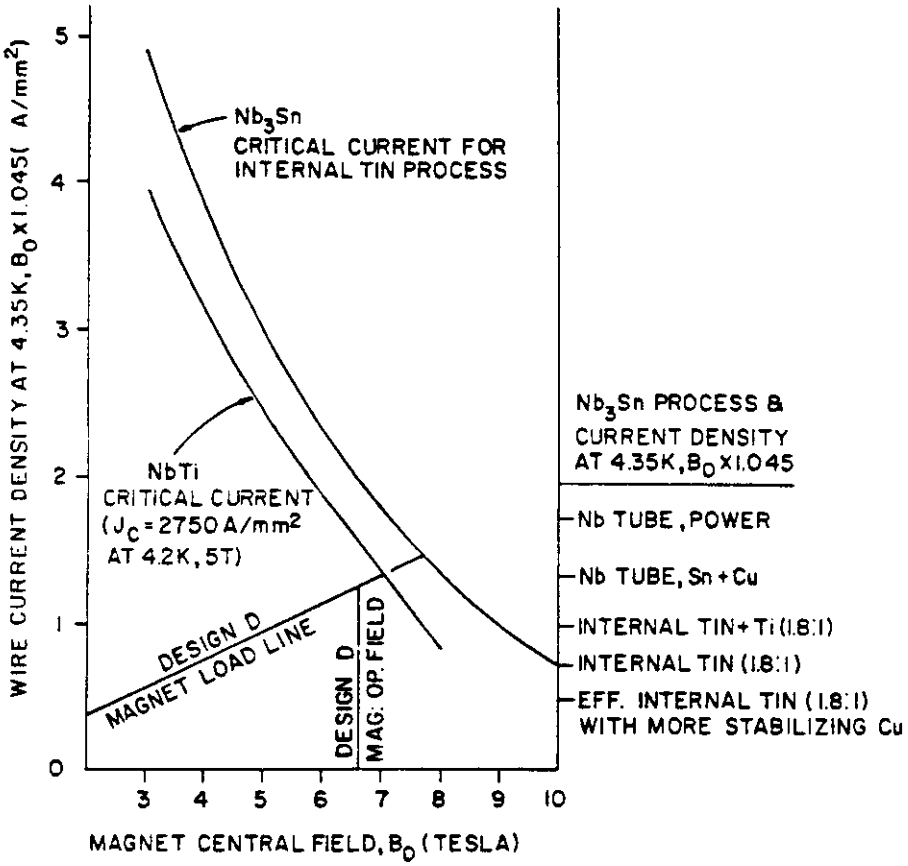

Figure B.3-6. Attempt to compare performance of an SSC Design D magnet constructed of NbTi and Nb_3Sn. The critical current lines for NbTi and Nb_3Sn are for wire production methods currently well developed. Most likely additional stabilizing copper would be required for Nb_3Sn effectively lowering the curve as indicated.

spacing designed to reduce magnetization to acceptable levels (1.8:1 local ratio). Other likely cost-effective processes for producing Nb_3Sn would have critical current lines having current densities at 10 Tesla indicated on the right side of Fig. B.3-6. However, those processes are not yet fully developed. The bronze process is not indicated here because it is felt that it would not be cost effective in large-scale production.

An important question that still remains is the amount of stablizing copper required for Nb_3Sn magnets. The critical current line for Nb_3Sn in Fig. B.3-6 is for wire with a copper-to-superconductor ratio of 1:1.

This ratio is most likely too low. The ratio is 1.3:1 for inner layer Design D magnet coils and 1.8:1 for outer layer coils; these values are found to be adequate for NbTi. At least the same current density is required for Nb_3Sn for similar quench protection behavior. Appropriate adjustment in the copper would effectively lower all points on the Nb_3Sn critical current line in Fig. B.3-6 by a factor of 0.87. As a consequence, the Design D magnets would not be expected to perform significantly better with Nb_3Sn by the present internal tin process than if they were constructed with currently available NbTi. Of course, improvements to the Nb_3Sn fabrication process, as indicated in Fig. B.3-6, could eventually change the arguments.

Conclusions

Among the available superconducting materials, NbTi and Nb_3Sn are the only ones which are available for large-scale production of accelerator magnets for the SSC. For dipole magnets designed to operate in the 6 to 7 T field range, the currently available Nb_3Sn produced by the internal tin process holds no advantages over the latest generation NbTi superconducting wire. The situation regarding choice of superconducting wires has changed significantly in the past year, when there has been a large improvement in the current density of NbTi wires accompanied by reductions in filament size; further improvements may be possible. There appear to be methods for improving Nb_3Sn further, possibly through addition of Ti. However, these improvements will require further R&D and 3 to 5 years of additional development, depending on the level of the R&D effort. For accelerator dipole magnets to operate in the 8 to 10 Tesla range at a temperature of 4.2–4.5 K, Nb_3Sn would hold the advantage over NbTi because of its higher critical field. However, the mechanical design and construction of such high field magnets present totally new challenges and would require significant additional magnet R&D.

There is optimism about perfecting the techniques for constructing accelerator magnets with Nb_3Sn using either the react-after-wind or wind-after-react methods. It would appear prudent to continue to pursue these development activities at a low level within the overall SSC R&D program to learn how to use brittle superconducting compounds in magnet construction. In fact, there might be a role for Nb_3Sn in the SSC if it is necessary to construct a few special magnets with very high dipole fields or especially large quadrupole gradients. However, for perhaps the next few years there appears to be no practical alternative to the choice of NbTi for the magnets of the main lattice of the SSC.

B.3.2 Choice of Superconductor and Cable Parameters

Superconductor

A collaborative R&D program, aimed at achieving significant improvements in the critical current density of NbTi, has been underway since 1983. This collaboration includes participants from U.S. industry (IGC, Supercon, TWCA, and OST), the University of Wisconsin, and LBL; it is funded by the Division of High Energy Physics of the U.S. Department of Energy. This collaborative effort has resulted in the demonstration, on an industrial scale and with superconductor produced in industry, that properties exceeding those chosen for the SSC Conceptual Design can be achieved. The steady progress in improving NbTi critical current density, and the implications for the Conceptual Design, will now be summarized.

The "new era" for high critical current density NbTi was initiated in 1982 with the report by the Baoji group of J_c = 3900 A/mm^2 at 5 T (using a more sensitive criterion for J_c, Larbalestier confirmed a value of about 3450 A/mm^2). This announcement stimulated a new interest in binary NbTi alloys in the U.S., in particular by Larbalestier and coworkers at Wisconsin. This group made an extensive analysis of conductors being produced in the U.S. and found that the composition of the NbTi alloy was quite inhomogeneous. They concluded that this lack of homogeneity prevented these alloys from responding effectively to the multiple heat treatments used by the Baoji group. After a series of discussions with the NbTi alloy manufacturer (Teledyne Wah-Chang, Albany) a collaborative experiment aimed at testing these ideas was begun in August, 1983. In this experiment a 10-inch billet was ordered by LBL. A special lot of high homogeneity alloy was purchased from TWCA and provided to a superconductor manufacturer for processing. After extrusion, the material was divided into two lots—one for processing by a standard commercial process and the other to be held until a J_c-optimization study could be completed and an alternative heat treatment suggested. The material processed by conventional techniques produced an improved J_c (about 2300 A/mm^2 compared with about 2000 A/mm^2 for the best Doubler/CBA material). This result was verified on two additional billets procured by LBL and processed while Larbalestier was completing his optimization studies. Larbalestier recommended a new processing schedule and IGC processed the remaining material with this schedule. The J_c values improved significantly (from 2365 A/mm^2 to 2645 A/mm^2 for the 0.6 mm diam. strand). Based on these results, LBL ordered two additional billets and FNAL ordered five billets. This material was delivered in the first half of 1985. The J_c values in all cases exceeded our target specification value of 2400 A/mm^2 (see Fig. B.3-5).

Another favorable result from these procurements has been the piece lengths compared with Doubler/CBA experience. The longer piece length greatly facilitates cabling and simplifies testing and quality control.

In addition to the SSC requirement of high current density, it is desirable to use conductors with a fine filament size in order to reduce field distortion at low fields due to magnetization effects. If a conductor can be fabricated with filament diameters of 2.5 μm or less, these effects could be largely eliminated. Another approach currently being evaluated would require a filament size in the 5-6 μm range. During the past few months, significant progress has been made in establishing the technical feasibility of fine-filament NbTi.

Conventional production of NbTi superconductor consists of a hot extrusion (500–600 C) of NbTi rods in a copper matrix. During this extrusion and the prior heating of the billet, a layer of titanium-copper intermetallic compound, perhaps 1–2 μm thick, can form around the filaments. This brittle intermetallic layer does not co-reduce and thus can become nearly equal to the filament diameter at final wire size; this results in extensive filament breakage and sometimes strand breakage. This problem can be eliminated by enclosing the NbTi rods at extrusion size in a barrier material, such as Nb or Ta, which prevents the titanium-copper intermetallic formation. This barrier need only be 0.1 to 0.2 mm thick, and will be reduced to an insignificant fraction of the filament cross section at final filament size.

Another problem can arise from the introduction of foreign particles during the billet preparation operations. Any "dirt" consisting of micron size particles, or any inclusions of this size in the NbTi rods or the copper components, can result in filament breakage at the final wire size. This type of problem is insidious, since processing may proceed successfully until the final wire size is approached. Also, the size of inclusion which is tolerable depends upon the desired filament size; e.g., a one micron diameter inclusion is acceptable for a 20 micron filament, but not for a 2 micron filament. This problem can be minimized by careful selection of raw materials and by clean room practice in billet assembly.

When a large number of rods are stacked in a billet, as is necessary to achieve fine filaments, a large void fraction is present, and this can lead to non-uniform reduction in the extrusion step. The filaments are necked down locally and this also leads to filament breakage. This problem can be eliminated by compacting the billet before extrusion.

When these potential problems are eliminated by proper processing and quality control, there is no metallurgical reason why a J_c value of greater than 2400 A/mm^2 cannot be achieved in filaments approximately 2 μm in diameter. In fact, the increased total reduction in area of the NbTi filaments may mean that it is possible to introduce more heat treat/cold work cycles and hence raise the value of J_c.

Several results from industrial scale billets procured as part of the SSC superconductor R&D program have been reported. These results indicate that J_c-values exceeding 2750 A/mm^2 can be expected in a fine filament NbTi superconductor. At present, this current density has been achieved in conductors with 5 μm filament size processed by several companies using several different techniques. However, J_c values exceeding 3000 A/mm^2 in material with less than 3 μm diameter filaments have been achieved to date by only one manufacturer. Thus, a more conservative filament size value of 5 μm has been chosen for use in the CDR. R&D efforts are continuing in order to determine the practicality of a specification of 2750 A/mm^2 in 2.5 μm NbTi filaments.

Cable

The most important cable parameters to be established are copper to superconductor ratio, number and size of strands, keystone angle, amount of compaction, and allowable dimensional tolerances. These parameters must be established with reference to a particular dipole magnet design. The CDR dipole magnet is based on a design developed at LBL in 1983, with the following guidelines. In order to minimize the amount of superconductor, a very small inner diameter (40 mm) was chosen. Next, emphasis was placed on obtaining the highest current density NbTi superconductor and on minimizing the amount of copper in the cable. The copper to superconductor ratio was chosen to give the inner

23 STRAND KEYSTONED CABLE

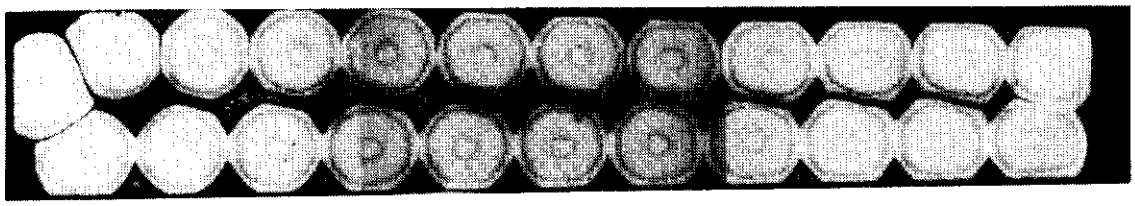

30 STRAND KEYSTONED CABLE

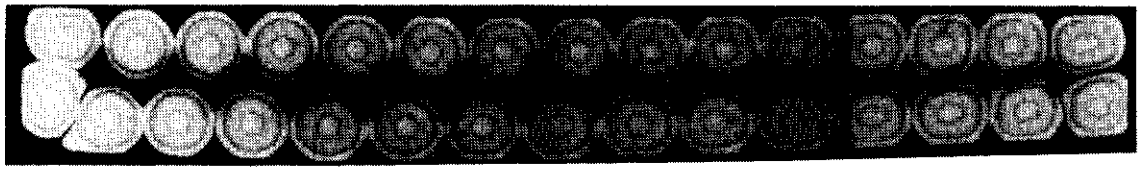

Figure B.3-7. 23 strand and 30 strand keystoned cable cross sections.

and outer layers approximately equal quench protection behavior. The number of strands in each Rutherford cable were chosen so that the inner and outer layers could be energized in series at the maximum efficiency. A "partial keystone" cable design was chosen in order to reach an optimum between achieving the maximum number of turns (full keystone with minimum number of wedges) and minimizing loss of critical current by cable damage. As a result of these considerations, the parameters discussed in the Specifications, below, have been established for the inner layer [Fig. B.3-7(a)] and outer layer [Fig. B.3-7(b)] cables.

After an initial R&D phase in which cabling parameters and techniques were developed, numerous cables have been produced and tested in the model dipole magnets constructed at LBL and BNL. These cables proved satisfactory both from the electrical and mechanical standpoint. Consequently, the remaining task before the quantity of cable required for SSC could be delivered is the construction of 6-8 production cabling machines. This can be accomplished with about 12 months' lead time and at a cost of less than $250,000 each.

References

B.3-1. R. M. Scanlan, "Superconducting Material," Annual Review of Materials Sciences **10,** 113–132 (1980).

B.3-2. M. Suenaga, "Metallurgy of Continuous Filamentary, A15 Superconductors," in *Superconductor Materials Science,* S. Foner and B. Schwartz, eds., pp. 201–274 (1981).

B.3-3. P. A. Sanger, 9th Symp. on Eng. Prob. of Fusion Research, IEEE Publ. 81 CH 1715, p. 1333 (1981).

B.3-4. R. M. Scanlan, D. N. Cornish, C. R. Spencer, E. Gregory, and E. Adam, *ibid,* p. 1317.

B.3-5. R. M. Scanlan, J. P. Zbasnik, R. W. Baldi, J. L. Pickering, Y. Furuto, M. Ikeda, S. Meguro, IEEE Trans. on Magnetics **MAG-21,** 1087 (1985).

B.3-6. D. B. Smathers, K. R. Marken, D. C. Larbalestier, and R. M. Scanlan, IEEE Trans. on Magnetics **MAG-19,** 1417 (1983).

B.3-7. C. van Beijnen and J. Elen, IEEE Trans. on Magnetics **MAG-11,** 243 (1975).

B.3-8. A. R. Kaufman and J. J. Pickett, Bull. Am. Phys. Soc. **15,** 833 (1970).

B.3-9. E. W. Howlett, U. S. Pat. 3, 728, 165 (filed Oct. 19, 1970); a Great Britian Pat. 52, 623/69 (filed Oct. 27, 1969).

B.3-10. Y. Hashimoto, K. Yoshizaki, and M. Tanaka, Proc. 5th Int. Cryo. Eng. Conf., Kyoto, Japan, 332 (1974).

B.3-11. C. Laverick, private communication.

B.3-12. D. C. Larbalestier et al., IEEE Trans. on Magnetics, **MAG-21,** 265 (1985).

B.3-13. R. M. Scanlan, J. Royet, R. Hannaford, and D. Horler, Int. Cryo. Materials Conf., M.I.T., Aug. 1985.

B.3-14. A. F. Greene, D. C. Larbalestier, W. B. Sampson, and R. Scanlan, "Status of Superconductor Development for the Design D Magnet," SSC Technical Note No. 39, distributed by BNL.

B.3-15. T. S. Kreilick, E. Gregory, J. Wong, paper CZ-6 presented at Int. Cryo. Materials Conf., M.I.T. (Aug. 1985).

B.3-16. P. Dahl et al., paper at 9th Int. Conf. on Magnet Technology, Zurich (1985).
B.3-17. P. J. Reardon, IEEE Trans. Nucl. Sci. **NS-32,** 3466 (1985).
B.3-18. SSC Conceptual Design Report, in preparation.
B.3-19. J. P. Zbasnik et al., Adv. in Cryo. Eng. **29,** 95 (1985).
B.3-20. R. M. Scanlan, J. P. Zbasnik, R. W. Baldi, J. L. Pickering, Y. Furuto, M. Ikeda, and S. Meguro, IEEE Trans. on Magnetics **MAG-21,** 1087 (1985).
B.3-21. P. A. Sanger, E. Adam, G. Grabinsky, E. Gregory, E. Ioriatti, and F. Roemer, Proc. Ninth Symp. on Eng. Prob. of Fusion Research, IEEE Pub. 81Ch1715-2, 1333 (1981).
B.3-22. J. Perot, IEEE Trans. on Magnetics, **MAG-19,** 1378 (1983).
B.3-23. C. Taylor, R. Scanlan, C. Peters, R. Wolgast, W. Gilbert, W. Hassenzahl, R. Meuser, and J. Rechen, IEEE Trans. on Magnetics **MAG-21,** 967 (1985).
B.3-24. A. Asner, C. Becquet, M. Rieder, C. Niqueletto, and W. Thomi, *ibid.*, 1410–1416.
B.3-25. M. S. Walker, J. M. Cutro, B. A. Zietlin, G. M. Ozeryansky, R. E. Schwall, C. E. Oberly, J. C. Ho, and J. A. Woolam, IEEE Trans. on Magnetics **MAG-15,** 80 (1979).
B.3-26. Y. Tanaka, M. Ikeda, and H. Tanaka, to be published in Proc. of 1985 Accelerator Conference.
B.3-27. N. Higuchi, K. Tsuchiya, C. J. Klamut, and M. Suenaga, Adv. Cryogenic Eng. **30,** 739 (1984).
B.3-28. M. Suenaga (unpublished).
B.3-29. T. Kuroda, M. Suenaga, C. J. Klamut, and R. Sabatini, to be published in Adv. Cryo. Engr. **32** (1986).
B.3-30. A. C. A. van Wees, P. Hoogendam, and H. Veringa, IEEE Trans. on Magnetics **MAG-19,** 556 (1983).
B.3-31. M. Suenaga (unpublished).
B.3-32. A. Ghosh (unpublished).
B.3-33. J. W. Ekin, "Superconductors," in *Materials at Low Temperatures*, R. P. Reed and A. F. Clark, eds., American Society for Metals, 496 (1983).

Appendix for Section B.3
Preliminary Specification for NbTi Superconductor Wire for SSC Dipole Magnets

1. Technical Requirements

1.1. ***Conductor Type:*** The conductor shall be a composite of NbTi filaments in an oxygen-free copper matrix. *The superconductor composition shall be Nb 46.5 ± 1.5 wt.% Ti, and shall be high homogeneity grade or equivalent.*

1.2. ***Critical Current:*** The conductors shall have a critical current greater than the values listed in Table B.3-A1. These values refer to a test temperature of 4.224 K and a critical current criterion of $\rho = 10^{-12}$ ohm−cm, based on the total wire cross section area and with the applied magnetic field perpendicular to the wire axis. *The currents given in Table B.3-A1 and the conditions defined above correspond to a current density in the superconductor of 2750 A/mm^2 at 5 T and 1100 A/mm^2 at 8 T.*

1.3. ***Filament Size:*** The vendor can choose a nominal filament size of 5 microns or less. In order to insure that the filaments are electrically decoupled, the filament spacing shall be greater than 0.5μm.

1.4. ***Copper-to-Superconductor Ratio:*** The copper-to-superconductor area ratio is determined by first weighing a length of wire and then weighing the filaments after dissolving the copper matrix in the same wire. The ratio is defined by the equation and constants below; the required values and tolerances are given in Table B.3-A1.

$$\frac{\text{Area of copper}}{\text{Area of superconductor}} = \frac{\text{Density of superconductor}}{\text{Density of copper}} \times \left[\frac{\text{Total weight}}{\text{Weight of superconductor}} - 1 \right]$$

Density of superconductor = 6.02 g/cm^3

Density of copper = 8.95 g/cm^3

1.5. ***Resistance at Room and Transition Temperatures:*** The resistance of the wire at room temperature (or normal state resistance) is usually expressed as R at 295 K or R_{295}. It is an important parameter for magnet construction and depends on the content and purity of the copper. The resistance of the wire at transition temperature, usually expressed as R at 10 K or R_{10}, can also provide a convenient independent check of the copper to superconductor ratio. The procedures for measuring R_{295} and R_{10} are described in Appendix B of this specification. The values for resistances and tolerances are given in Table B.3-A1.

1.6. ***Copper Residual Resistivity Ratio:*** The RRR for wire at final size, equal to R_{295}/R_{10}, is defined by the values of R_{295} and R_{10} given in Table B.3-A1. *The target values for RRR as given there are greater than 80 for the inner layer wire and greater than 90 for the outer layer wire.*

Table B.3-A1
Requirements for Inner and Outer Layer Superconducting Wire

	Inner Layer	Outer Layer
Requirement		
Minimum critical current at 5 T	613 A	323 A
Minimum critical current at 8 T	248 A	128 A
Copper-to-superconductor ratio	(1.3 ± .05):1	(1.8 ± .05):1
Wire diameter	0.0318 ± 0.0001 in.	0.0255 ± 0.0001 in.
Guideline Value		
R_{295} (micro-ohms/cm)	580 ± 15	800 ± 15
Maximum R_{10} (micro-ohms/cm)	7.0	9.0

1.7. ***Twist Pitch:*** The wire shall be twisted to produce a twist pitch of *1.0 ± 0.1* twists per inch at the final wire size. All wire shall be twisted clockwise so that the filaments follow the same rotation as a right-hand screw thread.

1.8. ***Final Anneal:*** The wire shall be *annealed at 260 C for 3 hours followed by a furnace cool.* This heat treatment will take place after the final drawing and twisting and shall be performed in a protective atmosphere so that the copper is not oxidized. Annealing is required to prepare the wire for subsequent cabling.

1.9. *Surface Condition:* The wire surface shall be free of all surface defects, slivers, folds, laminations, dirt, or inclusions. No NbTi filaments shall be visible.

2.0. ***Minimum Lengths:*** *The minimum acceptable length at final wire size shall be 2500 ft.* This minimum length shall be determined after all lead and end defects have been removed by cropping. These defects include areas of distorted cross section due to wire pointing by swaging, and foreign material attached as a temporary leader, or areas of distorted filaments that occur at the start and end of an extrusion.

2. Seller's Quality Assurance, Inspection, and Tests

2.1. ***Seller Responsibility:*** The seller shall establish a quality assurance program that assures manufacture of a product that complies with this specification. The seller shall provide the purchaser with seller's sampling plan and inspection schedule and a description of the means whereby he will maintain control over his own and his subcontractor's manufacturing processes, inspection and testing, handling and storage. Included shall be means for identification of conforming material, serialized identification by lot of finished product, and procedures for the segregation of nonconforming material. The seller's record-keeping system shall be such that traceability exists for all QC records and material used in the conductor from the time raw materials are received by the seller until the final conductor is completed. In particular, detailed records shall be maintained for billet extrusion conditions (time and temperature of pre-heat, extrusion temperature and speed, post extrusion cooling if any, etc.) and wire annealing conditions.

2.2. ***Test Witnessing:*** The purchaser reserves the right to witness manufacturing steps, tests, and inspections established under the seller's quality assurance program, and all other testing performed at the seller's plant and his subcontractor's plants to demonstrate compliance with this specification. Any information of a proprietary nature must be identified in the seller's bid response. The seller will not be required to disclose this proprietary information, but will be required to show that adequate records and quality controls are maintained in these proprietary steps.

2.3. ***Sample Testing:*** The seller shall measure the critical current for samples from each continuous length of wire at B = 5 T and 8 T, and T = 4.224 K. If a temperature of 4.224 is not possible, measurements may be made at another temperature and a conversion constant must be supplied. The conversion constant must be approved by Buyer. A 5-foot sample of wire adjacent to each length used by the Seller for critical current measurements shall be sent to the Buyer. These samples shall be identified by billet number, spool number, original continuous wire length, and purchase order number. Samples will be checked by the Buyer to insure that they conform to all aspects of the specification, both mechanical and electrical.

ASTM B-714-82 and Item 1.2 of this specification will form the basic method and criteria for measurement of the critical current of these samples. The techniques described in Appendix B of this specification are consistent with the ASTM procedures for determining the short sample critical current and will be employed by the Buyer to verify the measurements. In addition, Appendix B describes the practical test methods to be used for determining the normal state resistance and copper-to-superconductor ratio of the wire.

2.4. ***Certification:*** The seller must provide a written statement with each wire shipment certifying that it meets all of the buyer's specifications.

3.0. ***Spooling and Shipping:*** Wire shall be level-wound. Spools shall be labeled with wire length, weight, billet number and purchase order number. Spools shall be packaged so that neither spools nor wire are damaged in shipment.

Verification of Electrical Properties of Superconducting Wire

A. Short Sample Test Method for Critical Current Determination of Twisted Multifilamentary Wire.

1. *General Outline; Definition of Critical Current*

The V-I curve is determined as a function of increasing current until an irreversible transition or quench occurs. This measurement is carried out in specified external fields, 5 T or 8 T typically, applied normal to the wire axis, and in a temperature bath of liquid helium at 4.224 K. For currents less than the quench current the V-I curve is reversible.

The critical current is defined as that at which the resistance per unit length, R, is

$$R = 10^{-14}/(\pi D^2/4) \text{ ohms/m}$$

where D is the wire diameter in meters. The effective resistivity of the wire is 10^{-14} ohm/m.

2. *Sample Mounting*

The sample wire is most conveniently mounted on a cylindrical former so that it fits in a solenoid magnet (see Section 4 below). Either bifilar or monofilar mounting arrangement may be used, if the procedures outlined below are followed. A non-inductive (bifilar) form will provide adequate length, reduce inductive voltage signals, and provide for ease of connection; see Fig. B.3-A1. Shorter, monofilar mounts may be used if adequately sensitive signal detectors are available; voltage taps are arranged as in Fig. B.3-A2 in this case. Means must be provided for constraint of mechanical motion without interfering with coolant contact: use of a G-10 former with grooved location of wire and careful tensioning during mounting. Care must be taken to ensure that a temperature gradient is not introduced into the region of measurement (gauge length). Care must also be taken in bending the samples, especially at the end of a bifilar sample. The radius of curvature should be at least 5 wire diameters.

3. *Procedure (See Fig. B.3-A3)*

The sample length (between voltage taps) should be $\gtrsim 25$ cm. This corresponds, typically, to a voltage drop of several microvolts. This is readily measured with the aid of a suitable preamplifier or digital voltmeter. Samples of shorter length may be used if a well functioning nanovolt detection system is available. Equipment must be capable of determining the effective resistivity to a precision of 10%.

The amplifier signal should be recorded on an X-Y recorder (or if desired in a digital memory device). The V-I curve may be taken either point-by-point (current constant for each measurement) or continuously if induced signals due to ramping are not too large or noisy. Typically, current is supplied by a stable, well-filtered power supply. The current should be measured to a precision of $\pm 5\%$. Use of a low resistance normal metal shunt connected across the sample is permitted provided the resulting correction for shunt current is accurately known and is $<1\%$. Electronic circuitry for quench protection is preferable. Frequently, a quality index, n, is estimated using either the equation $V = \text{constant} \times I^n$ or $\rho = \text{constant} \times I^n$.

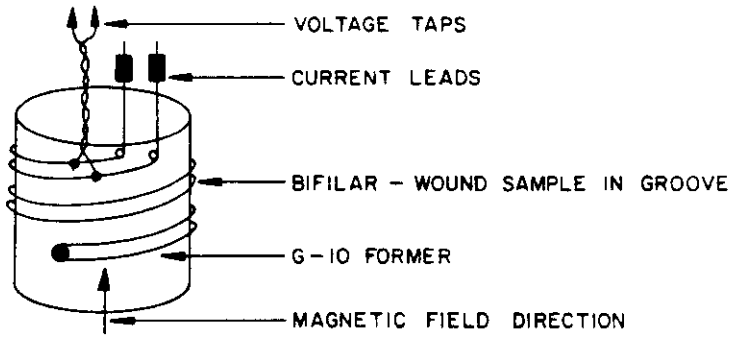

Figure B.3-A1. Non-inductive sample mounting arrangement.

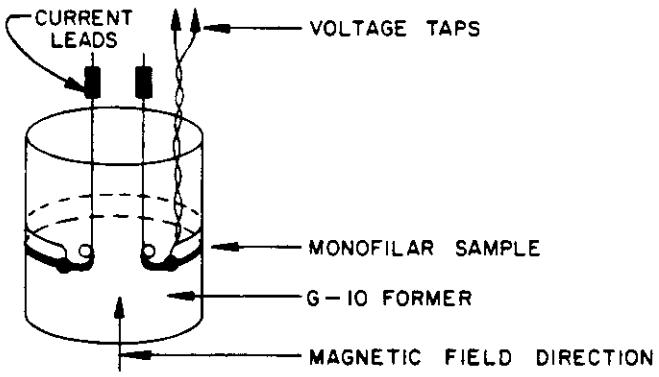

Figure B.3-A2. Alternative sample mounting arrangement.

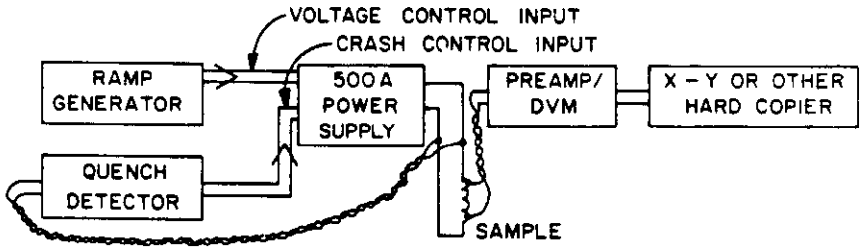

Figure B.3-A3. Schematic of electrical measurement apparatus.

4. *Magnetic Field*

The external field is most conveniently applied by means of a superconducting solenoid. The field must be uniform over the sample reference length to ±0.5%. The direction between field and wire axis must be 90° ± 6° everywhere. This range of angles corresponds to a variation in I_c of 0.5%.

5. *Bath Temperature Correction*

The specification temperature is 4.222 K, that of boiling helium at standard atmospheric pressure. The bath temperature must be recorded with the aid of appropriate thermometry (cryogenic thermometer or vapor pressure of bath) with a precision of ±0.010 K (10 mK). Deviations of 25 mK or less from 4.224 K correspond to an error in I_c of 1% or less and may be ignored. For larger temperature excursions the "linear T" type of correction should be applied

$$\frac{I_c}{I_m} = \frac{T_c - T}{T_c - T_m}$$

where T_c is the transition temperature at the specified magnetic field. (T_c = 6.9 K at 5 T and 5.7 at 8 T.) I_m is the current measured at temperature T_m, and I_c is the critical current at the specification temperature, T(= 4.224 K).

B. Test Method for Normal State Resistance of NbTi Superconducting Wire

1. *General Outline; Definition of Residual Resistance Ratio*

This method covers the measurement of electrical resistance of NbTi multifilamentary composite wire which is used to make high current superconducting cables. The composite matrix is copper. The resistance per unit length is determined at room temperature (295 K) and just above the transition temperature ($T_c \sim 9.5$ K). These quantities are designated R_{295} and R_{10}, respectively, and are measured with an accuracy of 0.5%. The ratio R_{295}/R_{10} is defined to be the residual resistance ratio, RRR.

R_{295} is determined chiefly by the copper matrix. For a given wire diameter it provides a measure of the volume copper-to-superconductor ratio (Cu/SC) of the wire.

R_{10} is determined chiefly by the residual resistance of the copper matrix. The ratio RRR provides a measure of the electronic purity of the copper matrix.

2. *Apparatus Description*

A four wire method is used to determine the resistance. The wire sample is mounted on a probe which is also used for superconducting critical current measurements. It has leads which are suitable for carrying the required current from room temperature into a liquid helium bath, and potential leads for measuring the voltage drop across a measured length of the test specimen. The probe should be mounted so that the test specimen can conveniently be raised and lowered through the level of a helium bath.

Voltage drops are measured with a digital voltmeter of 0.5 μV resolution. It is helpful during the low temperature measurement to use an X-Y recorder simultaneously with the digital voltmeter, with Y set to voltage and X to time (see Section 4 below).

Current in the range 0.1 to 1.0 A is provided by a well regulated and filtered dc power supply. It is measured by a shunt of 0.5% accuracy.

In the room temperature measurement a thermocouple device of 0.1 C accuracy is used to determine the ambient temperature.

3. *Sample Mounting*

The test specimen is wound on a grooved form. The ends are soldered to the copper terminations of the current leads over a minimum length of 1 inch. Voltage taps are soldered to the specimen at a distance of at least 1 inch from the current joint. Voltage taps are soldered to the specimen at a separation distance of at least 1 inch from each current lead connection. It is advisable that these taps be in the form of fixed pins so that the test length be constant throughout a series of measurements. In order to assure an accuracy of 0.2% this length should be 50 cm or more. The voltage leads should follow the sample in a non-inductive fashion so as to minimize noise pickup. Alternatively, the sample may be wound non-inductively on the form.

4. *Procedure*

Room temperature measurements are made at currents which are a compromise between the requirements of sensitivity and negligible ohmic heating. A typical value is 0.5 A. Voltage readings are taken for forward and reversed current and averaged.

Low temperature measurements are made in a helium dewar. The probe is raised so that the lowest point of the specimen is a few centimeters above the liquid helium bath level while measuring current is flowing. As the sample warms, the voltmeter reading will go suddenly from zero to a finite value corresponding to its normal state resistance. The latter is substantially independent of temperature from the transition temperature, T_c, to 15 K, so that the voltage remains constant long enough to be read and is recorded. With a reasonably designed probe and former it may take 1 or 2 seconds for the specimen to go normal. The resistance will remain in the residual resistance region several times longer than this. When the X-Y recorder is used, a series of abrupt voltage changes are recorded as the specimen is alternately raised and lowered through the helium bath level. The height of these steps should be reproducible.

5. *Room Temperature Correction*

Normally occurring room temperature variations may produce significant variations in the measured resistance. Designating this resistance as R_m and the ambient temperature as T_m (C), the resistance at the reference temperature of 295 K is calculated as follows

$$R_{295} = R_m / |1 + 0.0039\,(T_m - 22)|$$

The effect of the NbTi is neglected for the purpose of this correction.

6. *Copper/Superconductor Ratio*

The copper-to-superconductor (Cu/SC) ratio is related to R_{295}. Therefore, an independent check can be made of this ratio measured by a weighing technique and by measuring R_{295}. The range of acceptable values of R_{295} is determined by the Cu/SC ratio and the wire diameter.

Specification for NbTi Superconductor Cable for SSC Dipole Magnets

The final assembled conductor is a flat (Rutherford) cable. It is composed of either 23 or 30 superconducting wires which are twisted around one another during the cabling operation and then pressed into a keystoned shape. Each wire is a multifilamentary conductor with requirements described in an accompanying specification.

1. *Details of Cable Construction and Dimensions*

The dimensions of the cable and other properties are given on the attached drawing (Drawing No. 20-00.49-4E). (This drawing is available from LBL or BNL).

The following comments relate to the construction and dimensions of the cable:

Note 1: The project staff will work with the cable vendor to establish the correct keystone angle and edge dimensions of the cable using measuring techniques that have been developed for this type of cable. Prior to a production run, samples will be sent to the project office for evaluation.

Note 2: The mid-thickness of the cable will be measured once for each continuous length of cable. This procedure will include cutting a 5 ft cable sample at the start of each cable reel and then dividing this piece into 10 equal-length segments. These 10 segments shall be placed with alternating keystone direction into a fixture and squeezed with the fixture to a specified pressure to determine the overall stack height. Results shall be recorded and sent to project office with other documentation about the cable. The project staff will verify this measurement on receipt of the cable samples with a similar measuring fixture. The resulting stack measurements for each piece of cable produced for GSC must match the total stack thickness given on the drawings accompanying this specification.

Note 3: The cable width will be measured at least once every 500 ft during cable manufacturing. This measurement will be made with the cable under tension during the cabling operation. Results shall be recorded in sequence and sent to the project office with other documentation about the spool of cable. The resulting measurements, with correction for the amount of springback, must match the cable width given on the accompanying drawing. The project office will work with the cable vendor to establish the cable width springback values.

Note 4: The reference to a cable edge radius is a caution that all cable which may cause damage to the cable insulation during coil winding or magnet assembly will be rejected.

Note 5: The directions of wire and cable twist (or lay) and cable twist pitch which have been successful during previous manufacturing of cable and subsequent use of the cable in coil winding are given on the accompanying drawings. If the vendor wishes to use different conditions during manufacture of cable, these changes must be approved by the project office.

2. *Additional Requirements on Cable*

a. Every billet of material, piece of strand, and spool of cable—either used in the manufacturing or shipped to the SSC project—shall have a unique serial number.

b. The vendor shall deliver to the project office 12 ft long samples of cable from one end of every continuous length of cable. These samples shall be marked with their serial numbers and delivered to the project office soon after the manufacture of the cable and ahead of the regular cable shipment. The cable samples will be accompanied by documentation as described below and will be shipped in a condition so they will not be damaged. The samples will be used to check that cable dimensions and electrical properties meet the requirements within the stated tolerances.

c. The vendor may use cold welds during the manufacture of the cable. No single strand can have two cold welds within a distance of 1000 ft, and there will not be any welds in the cable closer than 100 ft.

d. The vendor shall supply a strand map giving the serial numbers of the strands used in the cable manufacturing and the locations of any cold welds.

e. The cable surface must be thoroughly clean and free from oil, mechanical particles or residue. Any cleaning solvents to be used must be approved by the project office. The cable must be free of roughness, sharp edges or burrs. There can be no crossovers of strands in the cable. The cable cannot have excessive residual twist. If a light residual twist is observed, it should be in the reverse direction of the lay, so the straightening of the cable during magnet winding will result in a tighter cable.

f. For transporting, the cable must be spooled with a radius large enough to prevent damage to the cable properties. The spools must be constructed to prevent damage to the cable during spooling and unspooling. The spools shall be boxed or strapped to a pallet to prevent damage in shipment. The cable must be wound so there are no crossovers of the cable windings. A sheet of plastic or paper will be placed between cable layers to prevent penetration of one layer into another. The cable will be wound onto a spool in the following manner, with the observer looking down onto the spool and with the cable being wound in the horizontal plane:

    1. The spool rotation direction for winding the cable onto the spool shall be counterclockwise.
    2. The cable top or thick keystone edge will be up (facing the observer looking down).

3. *Electrical Requirements on Cable*
The electrical requirements are listed in Table B.3-A2.

Table B.3-A2
Electrical Requirements on Completed Cable

	Inner Layer	Outer Layer
Minimum critical current measured with magnetic field perpendicular to wide surface of the cable (measured at 4.224 K and 1×10^{-14} ohm m effective resisitivity across the entire cross section)		
Critical current at 5 T	11970 A	8239 A
Critical current at 8 T	4744 A	3266 A
R (295 K) (micro-ohms/cm) of finished cable See Note.	595^{+5}_{-15}	810^{+5}_{-15}
R (10 K) (micro-ohms/cm) of finished cable See Note.	8.5^{+0}_{-2}	11.0^{+0}_{-2}

Note 1: The RRR for finished cable is defined by the values of R_{295} and R_{10} given in Table B.3-A2. The target values for RRR as given there are greater than 70 for the inner and outer layer cables.

B.4 Operating Margin for Dipoles

M. Tigner
SSC Central Design Group

March 19, 1986

Of concern is the avoidance of quenches at high field where the heat absorption capability is least. A likely mechanism for inducing quenches is beam loss. Radiation level detectors in the tunnel will detect excessive beam loss, and fire the abort system. Thus, the excessive energy deposition may continue for as long as 300 μsec—the time needed to dump the beam.

If ℓ is the maximum volumetric energy deposition in the superconductor (due to normal beam-gas scattering loss), in watts, N is the multiplier due to this extraordinary condition, and τ is the time to detect such conditions and abort the beam, then the maximum temperature rise due to this excessive loss is

$$\Delta T_e = \frac{N \cdot \ell \cdot \tau}{C} \tag{B.4-1}$$

where C is the volumetric specific heat of NbTi at the operating temperature and magnetic field. If the "temperature margin," moreover, is denoted by ΔT_m and defined by

$$\Delta T_m = \left[T_c(B) - T_{\text{oper}}\right]\left(1 - \frac{J_{\text{oper}}}{J_c}\right), \tag{B.4-2}$$

then a quench will occur when $\Delta T_e = \Delta T_m$. (We assume the act of aborting does not itself cause quenches.) Equating (B.4-1) and (B.4-2), we can solve for N, a measure of safety.
If

$$\Delta T_m \approx |6.2\ \text{K}^{\dagger} - 4.4\ \text{K}|\,(1 - 0.8) \approx 0.4\ \text{K}$$

and

$$\Delta T_e \approx \frac{N \cdot 0.025^{*}\ \text{mW/cm}^3 \cdot 300 \times 10^{-6}\ \text{sec}}{7\text{mJ/cm}^3 \cdot \text{K}^{\ddagger}} \approx 1.1 \times 10^{-6} \cdot N \cdot \text{K},$$

then

$$N \approx \frac{0.4}{1.1 \times 10^{-6}} \cong 3.6 \times 10^{5}$$

which, by this reasoning, seems entirely adequate.

[†]M. Wilson, *Superconducting Magnets* (Oxford, 1983), p. 73.

[‡]*Ibid.*, p. 72.

*Don Groom, private communication (March 11, 1986).

B.5 Fabrication of Superconducting Coils for SSC Reference Design D Model Magnets

M.D. Anerella, J.R. Cullen, and A.F. Greene
Brookhaven National Laboratory

February 14, 1986

The superconducting coils for SSC straight-ended magnets have been fabricated using methods developed at BNL, starting with coils for CBA prototype magnets. It seems appropriate to relate the techniques used for fabricating the coils and to include descriptions of the component parts. The coil molding techniques, using a recure procedure, are somewhat unique. The methods are described here with an evaluation of the sizes of the individual coils produced for a series of six SSC model magnets, all constructed to demonstrate reproducible field quality.

B.5.1 Design Origins

Source Documents

The documents upon which the engineering design of the SSC magnet coils is based are the SSC Technical Note No. 19, "Coil Design for the 40 mm Collared Coil Dipole (SSC-C5)" and SSC Technical Note No. 23, "The 1-in-1 SSC Dipole with C-5 coils." These documents supplied the basic information which was used to develop engineering designs for the individual component parts of the dipole coils.

Design of the coil end is similar to that of other straight-ended coils. In previous coil designs, however, conductor turns were placed around the bore tube in a radial fashion. That is, the interfaces between conductors lie on radial lines with respect to the geometric center of the coil. This was possible because the coil radii were large enough to allow full keystoning of the conductor to the theoretical angle dictated by coil radius and mean conductor dimensions.

In an effort to reduce the cost of producing magnet coils, there has been a trend to reduce the coil diameter. Unfortunately, as the diameter decreases, the keystone angle for a given conductor increases. In general, increasing the keystone angle of a conductor increases the amount of degradation of the superconductor due to the keystoning operation. To reduce this degradation, coil geometries were developed using keystone angles which are some fraction of the full theoretical keystone. These partially keystoned conductors do not lie on radial lines within the coil. This complicates the design of most of the subcomponents in the coil. This is, however, not an insurmountable problem, and is the only

significant design difference between these and previous coils from a coil fabrication point of view. |Note, moreover, that the dipole cross section (C-5) utilized for initial 4.5 m model dipoles and initial 17 m prototype dipoles differs slightly in the wedge design (conductor sizes and total number of turns remain unchanged) assumed for the coil cross section NC515 specified in the SSC Conceptual Design and described in Section B.2 of Attachment B.| Figure B.5-1 shows the distribution of turns in the coil end.

B.5.2 Coil Components

Parts Catalog

A listing of parts used in the fabrication of the magnet coil is given in Table B.5-1. Although the conductor cable is listed here, a detailed discussion of the cable, including its mechanical and electrical properties, is given in the report entitled "Superconductor: Conductor Development, Final Specifications" appearing elsewhere in Attachment B.

Part Fabrication

In the following paragraphs fabrication of the individual subcomponents which make up a dipole coil will be discussed.

a) Wedges

Items 1–6 in Table B.5-1 are the drawings which make up the wedges used in the inner and outer coils of the magnet. In order to avoid repetition, the fabrication of a typical wedge will be discussed, and this discussion shall apply to all three wedges used in the inner and outer coils, as the fabrication of all wedges is identical.

Wedges are extruded and rolled to the precise cross-sectional geometry defined by the engineering drawing and are rough-cut to a length of 28 in. ± 1/8 in. by an outside vendor. The material used to fabricate these wedges is ASTM 102 OFHC copper (half-hard minimum). They are then cut at BNL to the precise length required, 27.125 in. ± 0.0002 in. for inner coils and 27.062 in. ± 0.002 in. for outer coils. Wedges which have been cut to length are now ready for insulation. After deburring and an alcohol wash, exposed ends of the wedge are sprayed with three coats of GE-7031 Adhesive and Insulating Varnish. Two minutes drying time is allowed between coats. The wedges are then allowed to air dry for a period of 30 to 45 minutes. This air-drying is required to prevent the formation of bubbles in the varnish during the bake cycle. After the air-drying period the wedges are placed in an oven which has been preheated to a temperature of 155 ± 5 C for a period of 1 to 1-1/2 hours. Baking prevents flow of the varnish during subsequent coil curing at 135 C. The wedges are helically wrapped in a semi-automatic machine with 0.001 in. thick × 3/8 in. wide Kapton tape which is coated with polyester resin adhesive on one side. This tape (T-320) is manufactured by Scheldahl Inc. The Kapton is half-lapped, adhesive side out, to form a 0.002 in. thick layer of Kapton on the surface of the wedge. The ends of the Kapton are secured with 0.001 in. adhesive-backed Kapton tape.

b) Saddles

Saddles are used to square off the ends of the coils and serve as a bearing surface for the end restraints. They are described in items 11, 12, 15, and 16 of Table B.5-1. These parts are molded of Ciba-Geigy XD-580 two-part epoxy ("green putty" in the vernacular). At present low rates of production these parts are molded in place on the coil mandrels

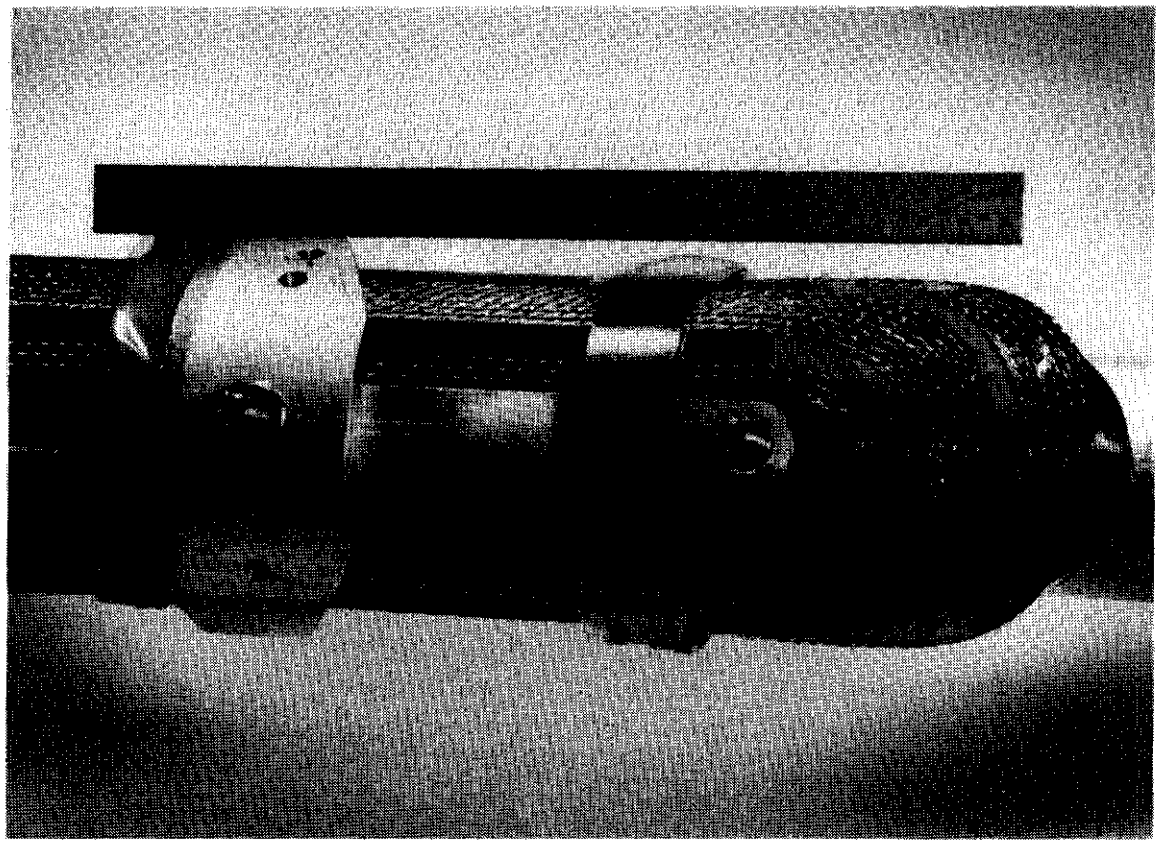

Figure B.5-1. End of model dipole coil, showing arrangement of superconducting turns.

Table B.5-1
Parts List

1)	22-299.11-2	Wedge, Inner Lower
2)	22-299.13-2	Wedge, Inner Upper
3)	22-299.17-2	Wedge, Outer
4)	22-299.18-2	Outer Wedge Wrapping Sequence
5)	22-299.12-2	Inner Lower Wedge Wrapping Sequence
6)	22-299.14-2	Inner Upper Wedge Wrapping Sequence
7)	22-299.04-3	Pretzel #1—Inner Coil
8)	22-299.05-3	Pretzel #2—Inner Coil
9)	22-299.06-3	End Spacer #1—Inner Coil
10)	22-299.07-3	End Spacer #2—Inner Coil
11)	22-299.19-3	Saddle Outer Coil Return End
12)	22-299.20-3	Saddle Outer Coil Lead End
13)	22-299.21-3	L.H. Wedge Tip Outer Coil
14)	22-299.22-3	R.H. Wedge Tip Outer Coil
15)	22-299.15-3	Saddle Inner Coil Return End
16)	22-299.16-3	Saddle Inner Coil Lead End
17)	22-299.08-3	End Spacer #3—Outer Coil
18)	22-299.09-3	End Spacer #4—Outer Coil
19)	22-299.10-3	End Spacer #5—Outer Coil
20)	20-000.49-4	Keystoned Cable and Insulation

during the winding operation. For slightly higher production rates they would be molded from green putty off-line in a separate operation. In full-scale production these parts would be injection-molded in Rogers RX-630.

c) Wedge Tips

Wedge Tips are described by items 13, and 14 in Table B.5-1. These small parts are used to smoothly taper the ends of the wedges and to create a smooth transition into the coil end region. The feathering wedges are fabricated from G-10 fiberglass material which has been machined to the cross section of the wedge to which it mates. Although the present method of fabrication is to sand the contour of the feathering wedge by hand to match the drawing, production runs would be produced by injection molding of Rogers RX-630.

B.5.3 Coil Fabrication

The fabrication method described here is based on the use of cable with an outer wrap of 0.004 in. B-Stage impregnated fiberglass tape. An experimental method of fabricating these coils without the glass tape is being investigated at Fermilab.

Fabrication of a magnet coil consists of two operations. First the coil is wound on a winding mandrel, then this mandrel is placed into a curing press and the coil is heated to form the individual turns into monolithic conductor blocks. The details of these operations will be discussed in this section.

This description of the winding operation will specifically discuss the winding of the outer coil. Winding of the inner coil is essentially identical to winding the outer coil, except that there is a different number of turns in each conductor block and there is an extra set of wedges, yielding three conductor blocks as opposed to two in the outer coil.

Winding

Prior to winding, the tooling and magnet parts are prepared. Winding tooling is cleaned of excess epoxy which may have accumulated during the previous curing operation, and is inspected for any damage or other anomalies which may have occurred during the previous curing step. Magnet parts are given a last visual check to insure that they are ready for the winding operation and that the proper quantities of each part are available. Figure B.5-2 is a photograph of the coil winding fixture.

The following steps are required to wind an outer SSC dipole coil:

1. Apply Frekote 1711 mold release to the winding mandrel.
2. Place one strip of Kapton, 5/16 in. wide $\times$ 0.001 in. thick, along each of the centerpost covering the straight length of the coil. This Kapton strip serves as an additional mold release agent.
3. Spray Frekote mold release over the Kapton strips applied in Step 2 above.
4. Initialize the coil winder. This action initializes the programmable controller and places the carriage of the coil winder in the proper position to allow off-spooling of cable so that the cable can be anchored in the center post.
5. Place the cable into the lead slot in the center post and activate the lump detector. This device sounds an alarm when it senses a lump on the cable of 0.015 in. or more, suggestive of a cable misweave.

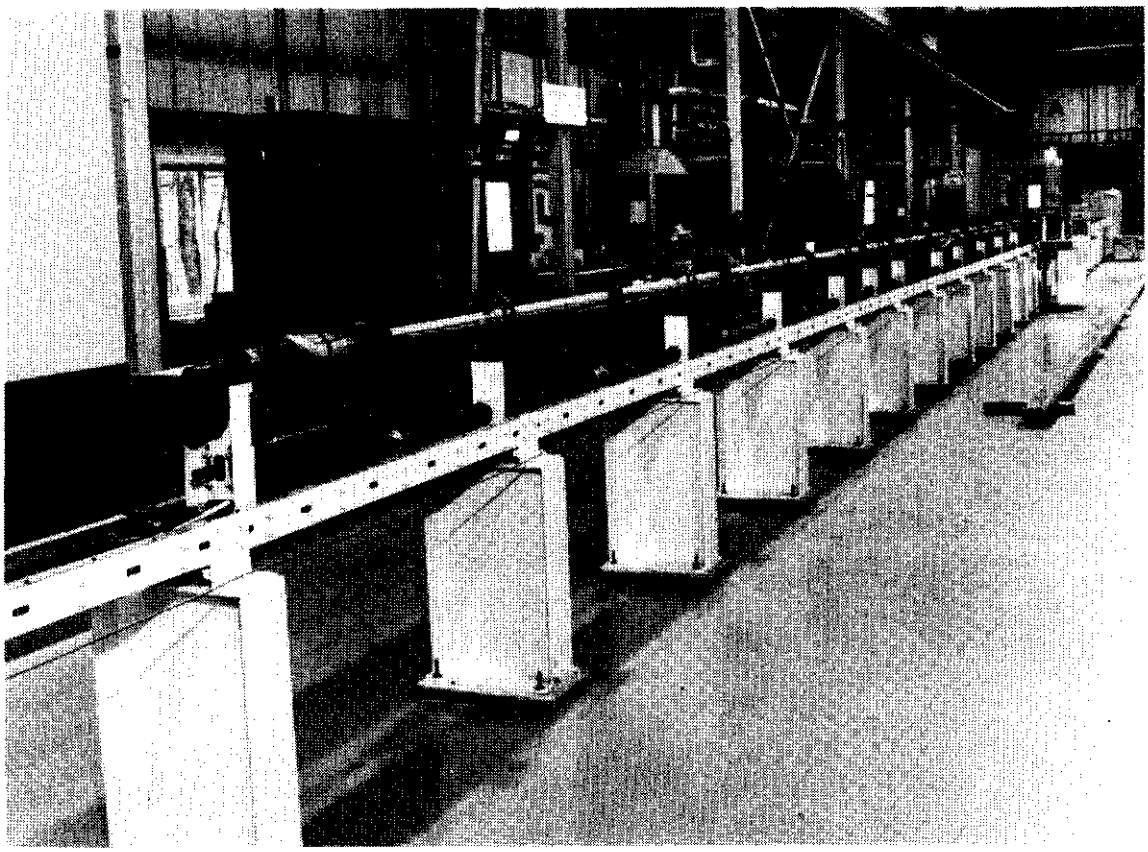

Figure B.5-2. Fixture for winding 17 m long dipole coils.

6. Mount winding "horseshoes" along the straight section of the mandrel. Clamp the first turn of conductor against the centerpost.
7. Wind twelve turns of conductor onto the mandrel.
8. Insert 1/2 of split "pretzel" and first wedge into the coil and apply first 1/2 turn of turn thirteen. Install balance of wedges for first half of turn thirteen.
9. Insert return end pretzel and first wedge in coil and apply second 1/2 turn of turn thirteen. Install balance of wedges for turn thirteen. Install other half of split pretzel.
10. Install one 3/8 in. wide $\times$ 0.005 in. thick $\times$ 1 in. long Kapton strip between turn twelve and the wedge and between turn thirteen and the wedge where the wedge and pretzel meet. Do this at both ends of the coil. This is to reduce the severity of transition from wedge to pretzel.
11. Wind the remaining seven turns.
12. Verify the turn count and perform a visual coil inspection.
13. Clamp the conductor to the mandrel and cut the cable, leaving 24 in. of extra cable.
14. Form green putty end spacers at the coil ends.
15. Mount and attach the pusher blade assembly to the mandrel. This assembly is used during curing to compress the coil azimuthally.
16. Tedlar wrap the coil using 0.001 in. thick half-lapped Tedlar. During application the Tedlar is tensioned at 20 pounds.
17. Remove completed, wrapped coil assembly from the winding fixture and transfer to the curing press.

Curing

The following procedure is used to cure an outer SSC dipole coil. This operation is described in graphical form in Figure B.5-3. Figure B.5-4 is a photograph of the curing fixture.

1. Clean and apply Frekote mold release to the curing fixture. Install hydraulic end "pusher" assemblies and tooling in the fixture.
2. Lower coil into the fixture and remove strongback from the mandrel assembly.
3. Seat coil in the fixture and install mandrel hold-down bolts. Hook up thermocouple and strain gauge instrumentation.
4. Verify that the hydraulic pull rod clamps are in the retracted position. Then lower top hat into position, install stop shims and position pull rods for clamping. The stop shims will be described in more detail later. They provide an adjustable method of closing the molding fixture and thus assuring dimensional uniformity of the coil. They may be changed for different coils to allow for variations in cable thickness.
5. Apply 500 psi hydraulic pressure (4.2 kpsi azimuthal stress) and heat the fixture to a temperature of 90 C. During this period of time relieve system hydraulic pressure at 10 minute intervals to allow the fixture to adjust for differential thermal expansion.
6. After 30 minutes at 90 C raise the fixture temperature to 135 C. Reduce steam pressure to 40 psi and allow the system to stabilize for 5 minutes.

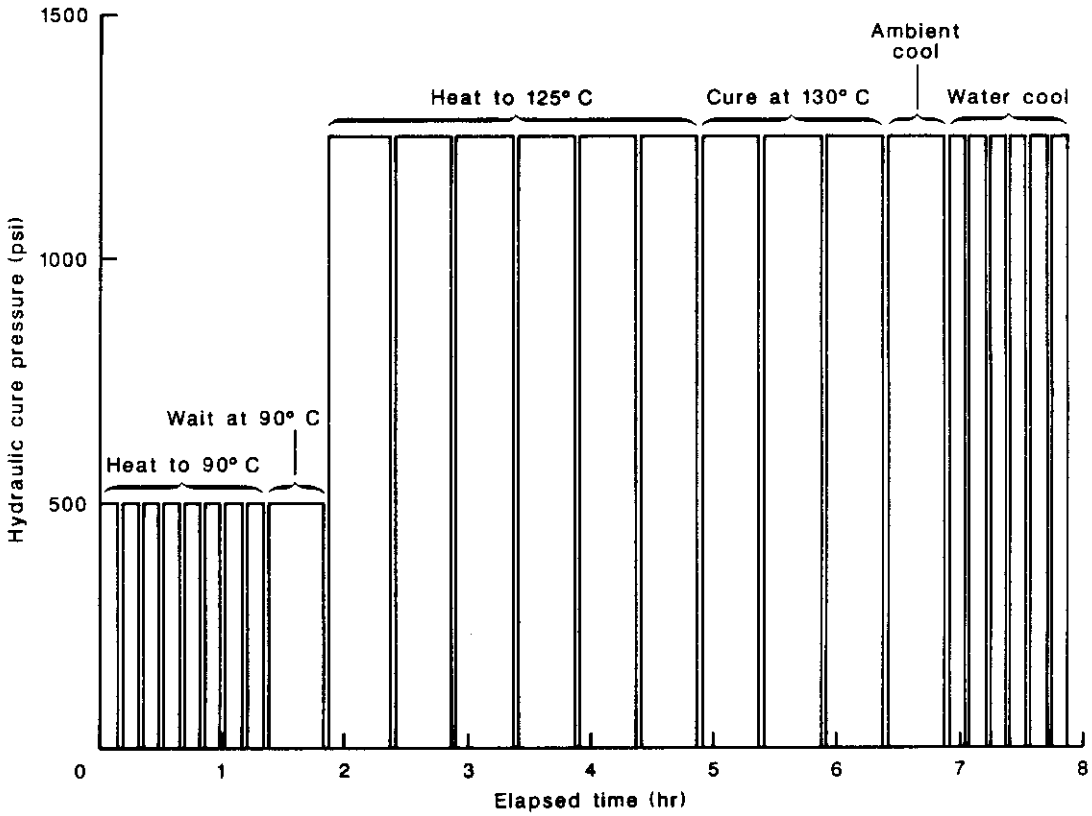

Figure B.5-3. Heating cycle for curing dipole coils.

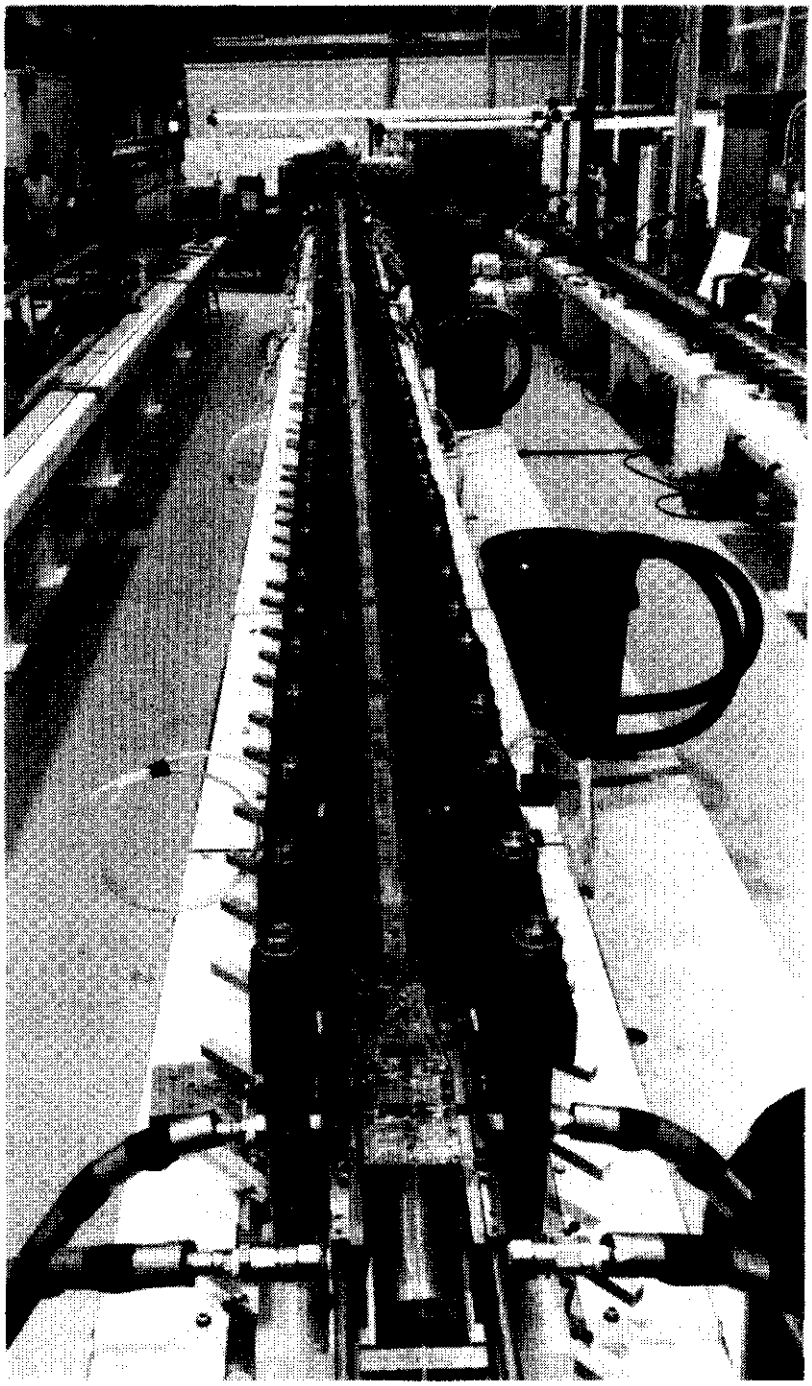

Figure B.5-4. Fixture for curing dipole coils under elevated pressure and temperature.

7. Apply side pressure to close the fixture. Record the pressure required to close the fixture. Actuate the end pusher system and close the end pusher to stop by applying 1000 psi to system.
8. Cure the coil at 135 ± 5 C for a period of 90–105 minutes. During the curing period cycle the fixture pressure every 1/2 hour to allow for differences in thermal expansion.
9. After 1-1/2 hour at 135 C cool the fixture to 30 C maximum. During the entire cooling process cycle the system hydraulic pressure at 10 minute intervals.
10. Reduce end pressure, then side pressure to zero psi. Remove stop shims. Apply 9000 ksi azimuthal stress to the coil and measure the fixture gap.
11. With the fixture gap at an acceptable size, the coil is removed from the fixture and transported to the coil assembly area for further assembly.

B.5.4 Coil Sizes

Discussion of Curing Methods

Early in the development of this type of coil using Rugherford type cable (i.e., during the CBA program) it was believed that two competing and conflicting requirements had to be fulfilled in order to produce a coil with the desired characteristics of consistent size and uniform elastic modulus. Intuitively, one can say that size uniformity is important from the standpoint of uniform conductor location, and for uniform pre-stress after assembly of coils in collars or yokes. It is also important for pre-stress that coil modulus be uniform from coil to coil. Ideally one should be able to produce a design which yields both the proper coil size and modules. It seems, however, that uniform size and uniform modulus would be conflicting requirements. This is because of the inevitable dimensional variations, such as bare cable mid-thickness, to be expected in reality. One might assume that if coils were molded using a constant size stop shim, then the goal of uniform size would be met. However, coils of varying modulus might result, due to variation in the cable mid-thickness. Alternatively, if one varied the stop shim so that a uniform modulus resulted, coil size might vary unacceptably.

With these ideas in mind, development of real coils was initiated. It was found that variation of conductor mid-thickness had slightly different effect than anticipated—a phenomenon known as overshoot was observed. Simply put, it was observed that if coils were produced using a constant size stop shim the coils modulus remained fairly constant. However, the size of the coils varied. Coils generally wound up measuring smaller than the size that would have been anticipated based upon the stop shim used. This dimensional difference was dubbed "overshoot." It is also possible for the coil to have zero overshoot, in which case recuring is not required, or negative overshoot. Using this result, a method of curing coils was developed which allowed the coils to be cured to a desired size with constant modulus of elasticity. This is accomplished as follows:

1. Cure the coil initially with a stop shim approximately 0.010 in. larger than the expected final shim size. A shim is used during coil molding so that the curing fixture can be closed, thus insuring a uniformity of dimensions. Measure the as-cured coil size while still in the fixture (this measurement procedure will be described later).

2. Compare the measured coil size with the ideal coil size calculated from the shim size used. Calculate the overshoot obtained.
3. From an empirically determined plot of first curing overshoot vs. recure overshoot determine the amount of overshoot which can be anticipated after a recure of the coil.
4. Select a stop shim for the recure which will yield the proper coil size based on the expected overshoot. Recure the coil.
5. Measure the recured coil, and remove from fixture, if properly sized; otherwise perform a second recure. In most cases only a single recure will be required.

Initially, because of schedule requirements, SSC coils were not cured using the more precise cure/recure process. They were cured using only a single cure, using a shim corresponding to the final coil size. Based on analysis of CBA coil data, this results in coils with an rms error band approximately twice as wide as recured coils.

b. In-fixture Coil Measurements

Since it would be very difficult to place a cured coil back into the curing fixture to do additional cures, it was necessary to design the fixture in such a way that the coil size could be measured in the fixture. Referring to Fig. B.5-5, with a coil in place and sized to be precisely at the midplane and the stop shims removed, one can see that a gap exists between the top hat and the form block. This gap is, by design, nominally 1/16 in. high; the as-built gap of each form block is carefully determined and recorded for use in coil size calculations. At the end of a cure stop shims are removed, and the system hydraulics are activated so as to apply an azimuthal stress of 9000 psi to the coil. The gap size is measured and compared to the as-built gap. We can now calculate the size of the coil relative to the midplane without removing the coil from the fixture. This is also the effective size of the assembled coil since it is measured at the nominal assembly pre-stress.

The validity of these gap measurements has been verified by measurements of coil size outside the fixture using a coil compression gauge. With the coil compression gauge taken as the standard of measurement, comparison of gap measurements are repeatable and the correlation between the two measurements is constant.

c. Coil Size Data

Table B.5-2 summarizes the size data for SSC coils which have been manufactured to date. The curing fixture sizes are measurements of the fixture gap referred to in Fig. B.5-5, and are used by coil factory personnel in the calculation of shim sizes to be used in recures and to determine if additional recures are necessary. The significance of these measurements should only be considered relative to the coil sizes produced as measured by the coil compression fixture. Compression gauge measurements are believed to be more accurate and are used to define coil sizes. Sizes stated in Table B.5-2 for compression gauge measurements are relative to the theoretical midplane of the coil. Zero indicates the coil is exactly at the midplane, positive indicates the coil is oversized or above the midplane, negative indicates the coil is undersized or below the midplane. The L (Left) and R (Right) size measurements in the curing fixture and compression gauge are actually the average of five measurements on each size of a coil equally spaced along the length.

Regarding the inner and outer coils as two groups we calculate, using the results in Table B.5-2, an overall average gauge measurement size for inner coils of 3.3 mils with an rms variation of 1.3 mils. Overall average for outer coils is 10.9 $\pm$ 1.4 mils. Absolute sizes

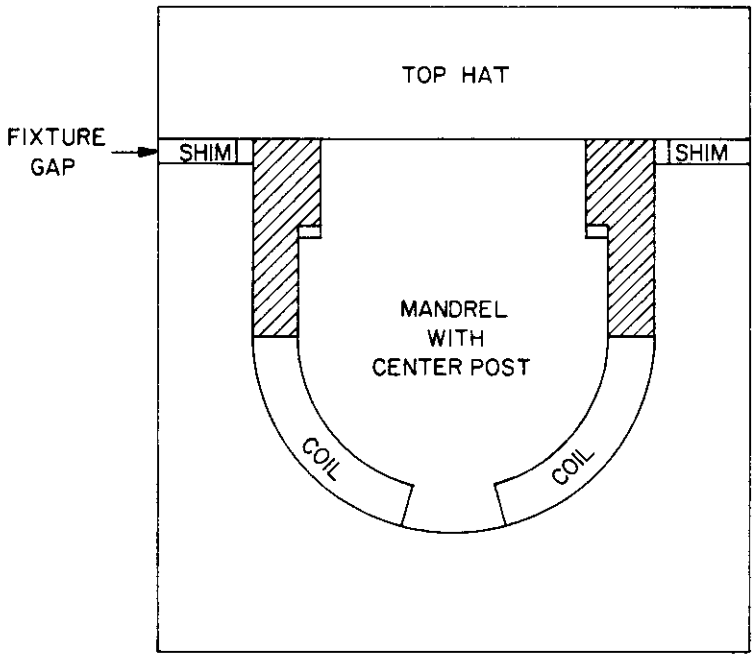

Figure B.5-5. Schematic cross section of curing fixture.

Table B.5-2
Coil Cure Data

Coil	Shim Size	Measured Size Cure Fixture L	R	AVG	Measured Size Compression Gauge L	R	AVG
I-1	58.0	54.3	55.8	55.1	1.6	1.5	1.55
I-2	70.0	60.2	65.2	62.7	5.0	4.7	4.85
I-3	70.0	59.2	65.0	62.3	2.6	2.1	2.35
I-4	70.0	60.0	66.0	63.0	5.1	4.8	4.95
I-5	70.0	59.6	63.3	61.4	1.9	1.3	1.60
I-6	70.0	67.3	73.6	70.5	—	—	—
	63.0	59.8	66.5	63.1	4.8	4.2	4.50
I-7	63.0	51.0	70.5	60.8	—	—	—
	64.0	57.6	65.5	61.5	4.1	3.5	3.80
I-8	63.0	57.3	64.6	61.0	1.7	1.6	1.65
I-9	64.0	60.5	65.8	63.2	3.3	2.9	3.10
I-10	75.0	63.7	69.7	66.7	—	—	—
	70.0	61.0	67.0	64.0	4.4	4.3	4.35
I-11	75.0	67.3	76.0	71.7	—	—	—
	64.0	61.5	67.8	64.6	—	—	—
	62.0	61.2	67.0	64.1	4.4	4.8	4.60
I-12	75.0	69.0	73.6	71.3	—	—	—
	62.0	59.3	63.5	61.4	1.5	2.3	1.90
I-13	75.0	68.6	73.6	71.1	—	—	—
	63.0	58.8	65.0	61.9	3.2	3.0	3.10
0-1	70.0	68.3	75.2	71.8	9.3	10.1	9.70
0-2	65.0	63.0	64.5	63.7	—	—	—
	70.0	63.0	73.0	68.0	8.8	8.5	8.65
0-3	68.0	67.0	73.0	70.0	12.3	9.8	11.00
0-4	67.0	66.5	68.5	67.5	—	—	—
	68.0	68.7	70.5	69.6	9.2	9.6	9.40
0-5	68.0	68.0	70.0	69.0	10.6	10.2	10.40
0-6	68.0	66.5	69.5	68.0	9.9	7.8	8.85
0-7	68.0	66.5	74.5	70.5	11.8	12.0	11.90
0-8	80.0	73.5	78.5	75.8	—	—	—
0-9	80.0	77.1	81.1	79.1	—	—	—
	58.0	72.7	77.8	75.3	—	—	—
	66.0	67.1	71.0	69.1	12.6	12.4	12.50
0-10	80.0	75.7	79.7	77.7	—	—	—
	66.0	67.1	71.5	69.2	13.8	11.9	12.85
0-11	80.0	75.1	80.5	77.8	—	—	—
	65.0	66.1	69.1	67.6	11.5	10.0	10.75
0-12	80.0	76.1	80.5	78.3	—	—	—
	66.0	65.5	70.0	67.7	11.0	13.0	12.0
0-13	80.0	76.5	79.2	77.8	—	—	—
	66.1	67.1	68.3	67.7	13.0	11.5	12.30
0-14	80.0	78.2	76.8	77.5	—	—	—
	65.0	68.1	68.0	68.0	11.1	10.3	10.70

required for coils are determined through an iterative process. Coils are assembled in a yoke and are squeezed to the midplane size. Coil prestress is measured and a determination is made as to the correct coil size. This information is fed back to the coil manufacturing operation and an adjustment is made in the as-built coil size if required. Small variations in coil size for the field quality magnets are accommodated in the yoke assembly by small variations in magnet prestress.

B.5.5 Conclusions

Coil winding and molding operations have become quite routine procedures which could easily be used in industrial production. The coil sizes resulting from these procedures appear to make it possible to demonstrate field quality performance for even a short production sequence of six model magnets. However, testing and magnetic field measurements can only show if these requirements are met.

Acknowledgements

Most of the tooling used for winding and curing the coils described here was designed by Y. Elisman and W. Stokes. The extremely competent technician staff in Building 924 is responsible for the high quality of the coils produced. The individuals with this responsibility are: J. Benante, C. Biggs, D. Ince, G. Jochen, R. McCluskey, T. Otten, W. Sandhoff, D. Schiappia, M. Stone, H. Strelecki, B. Vogt, M. Williams. Appreciation is extended to all of these individuals who have made possible the success of the coil construction.

B.6 Collars for the Design "D" SSC Dipole: A Design Review

R.J. LeRoy
Brookhaven National Laboratory

March 1, 1986

B.6.1 Abstract

The purpose of this report is to summarize the design of the collars, their use in the magnet, and the analysis done on the collars. This report revises and updates previous SSC Technical Note No. 32 of the same title. Covered are the considerations and analysis that went into the design of the collars. The collar loads are described which include the Lorentz forces at 6.5 T along with the necessary prestress to resist those forces. Outlined are the three basic considerations that determined the final design of the collars: collar deflections, collar stresses, and the magnetic losses due to the width of the collars. The finite element analysis used to predict the collar deflections and stresses is briefly reviewed. Material specifications and mechanical properties are presented on the stainless steel required for the collars. Measured results of collared deflections from both BNL and Lawrence Berkeley Laboratory (LBL) are given and compared to the predicted values. These results show that the actual room temperature deflections of the collars when keyed exceed those predicted. However, the collar deflections as measured by LBL when energized agree quite well with predicted values. Also, measurements taken of collars from the first 4.5 m magnet after disassembly indicate that the collars had yielded due to the loading in the press during keying.

Assembly experiences from the first 4.5 m magnets assembled at BNL are outlined along with a discussion on the retention of coil prestress after collar keying. Three areas of coil stress losses are identified and discussed: losses after pressing, coil relaxation, and losses due to cooldown. Finally, there is a discussion on what further work regarding the collars is being done or needs to be done.

B.6.2 Introduction

The Design "D" SSC dipole is a 4 cm bore, 6.5 T cold-iron superconducting magnet with collared coils. The function of the collars is to provide the necessary prestress to the coils to counteract the Lorentz forces generated for an operating central field of 6.5 tesla. This paper will discuss how the collar design was arrived at and how well the actual collars achieve this design.

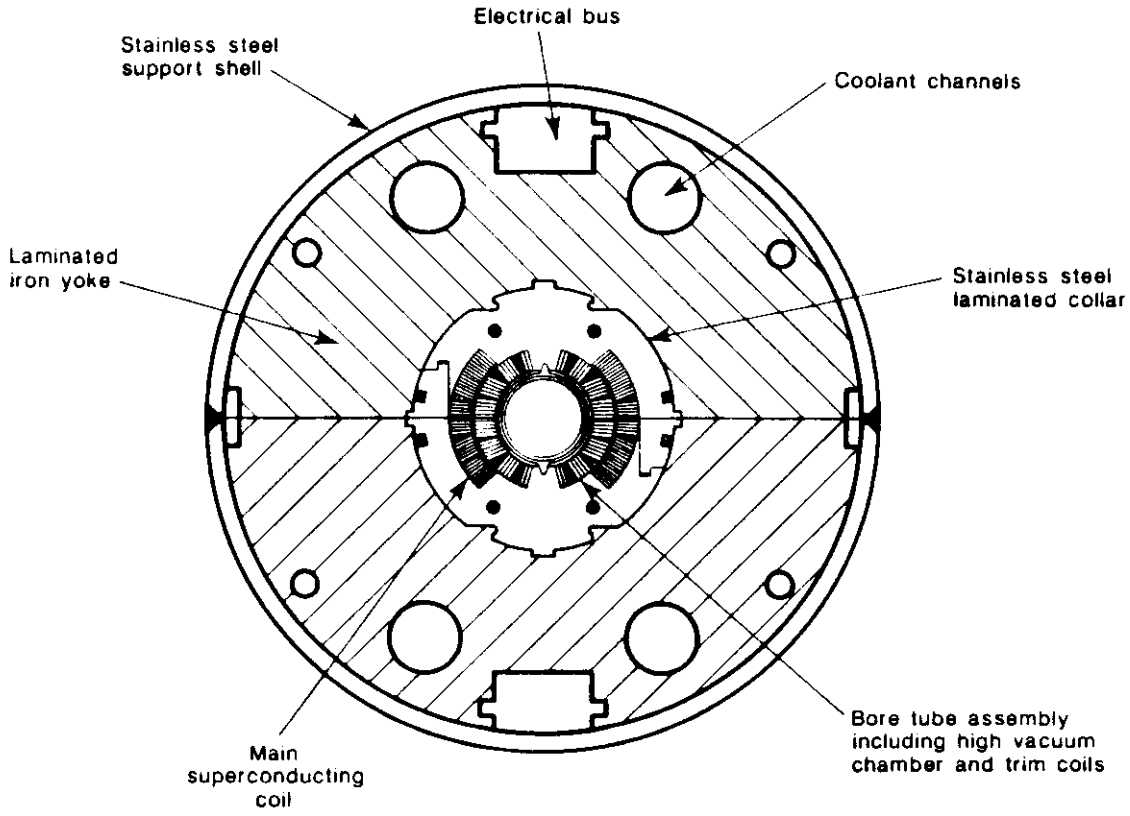

Figure B.6-1. Cross section of dipole magnet.

The design of the collars must take into account: the stresses developed in the collar under load, the resulting deflections, and the loss of field due to the removing of iron next to the coils. The collars also serve to position the coils within the iron yoke. The variable design parameters are collar cross-sectional width, keying slots, and material selection. A cross section of the magnet assembly in Fig. B.6-1 shows the 15 mm wide Design "D" collar with two 3/16 in. key slots. The collars are stamped from high strength stainless steel (60 ksi min. yield strength). The shape of the collars is similar to the Fermilab Saver collars. Fabrication and assembly of the collar packs are also similar except there is no welding involved. Pins and keys are used instead.

B.6.3 Collar Loads

The load that the collars must carry is dependent on the coil prestress necessary at 4 K to prevent the coils from pulling away from the poles when energized. The room temperature assembly prestress, which is greater than the 4 K prestress, is determined by taking into account coil stress losses due to differences in thermal contraction between collar and coil, and coil relaxation effects over time.

The 4 K prestress is determined by first calculating the Lorentz force per conductor turn for a central field of 6.5 T [B.6-1]. The plot in Fig. B.6-2 shows the circumferential and azimuthal components of the Lorentz forces per turn per linear inch. Next, a model of the coil is developed to calculate the force necessary to prevent coil motion at the pole along with the associated motions in the rest of the coil. The model in Fig. B.6-3 is of the inner coil. A similar model was also made for the outer coil.

This model is input into a finite element program using spar elements with the appropriate circumferential component of the Lorentz force applied at the nodes. To calculate the minimum coil prestress required, the pole and midplane are constrained. The resulting reaction force at the pole is the minimum force necessary to prevent coil motion at the pole. Different values of prestress are input by removing the constraint at the pole and applying an initial strain to each element corresponding to the prestress desired. Figure B.6-4 shows plots of coil deflections, ignoring friction effects, for: zero prestress, one half prestress, and full prestress. Assumed for deflection calculations in this figure is a conductor modulus of 1×10^6 psi. Measurements indicate this to be a conservative estimate of modulus at 4 K, thereby giving a higher estimate of coil motion. Required prestress is independent of elastic modulus.

Minimum Coil Prestress Required at 4 K and 6.5 T

Inner coil	3650 psi
Outer coil	2940 psi

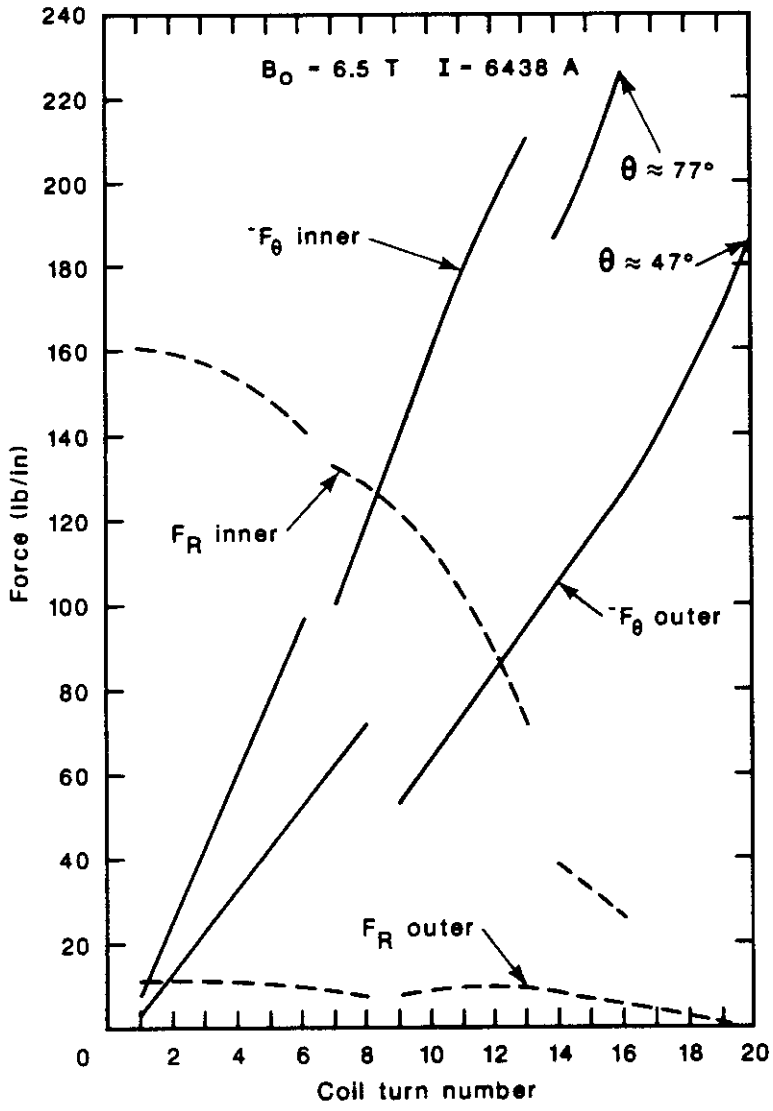

Figure B.6-2. Coil Lorentz forces per turn at a central field of 6.5 T.

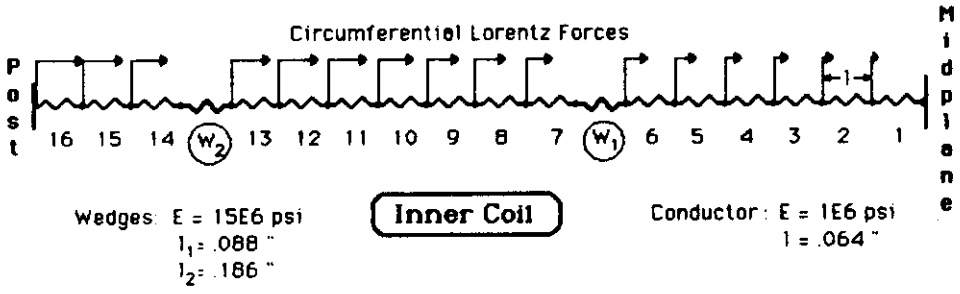

Figure B.6-3. Model for calculating azimuthal forces (prestress) necessary to prevent coil motion, for the inner dipole coil.

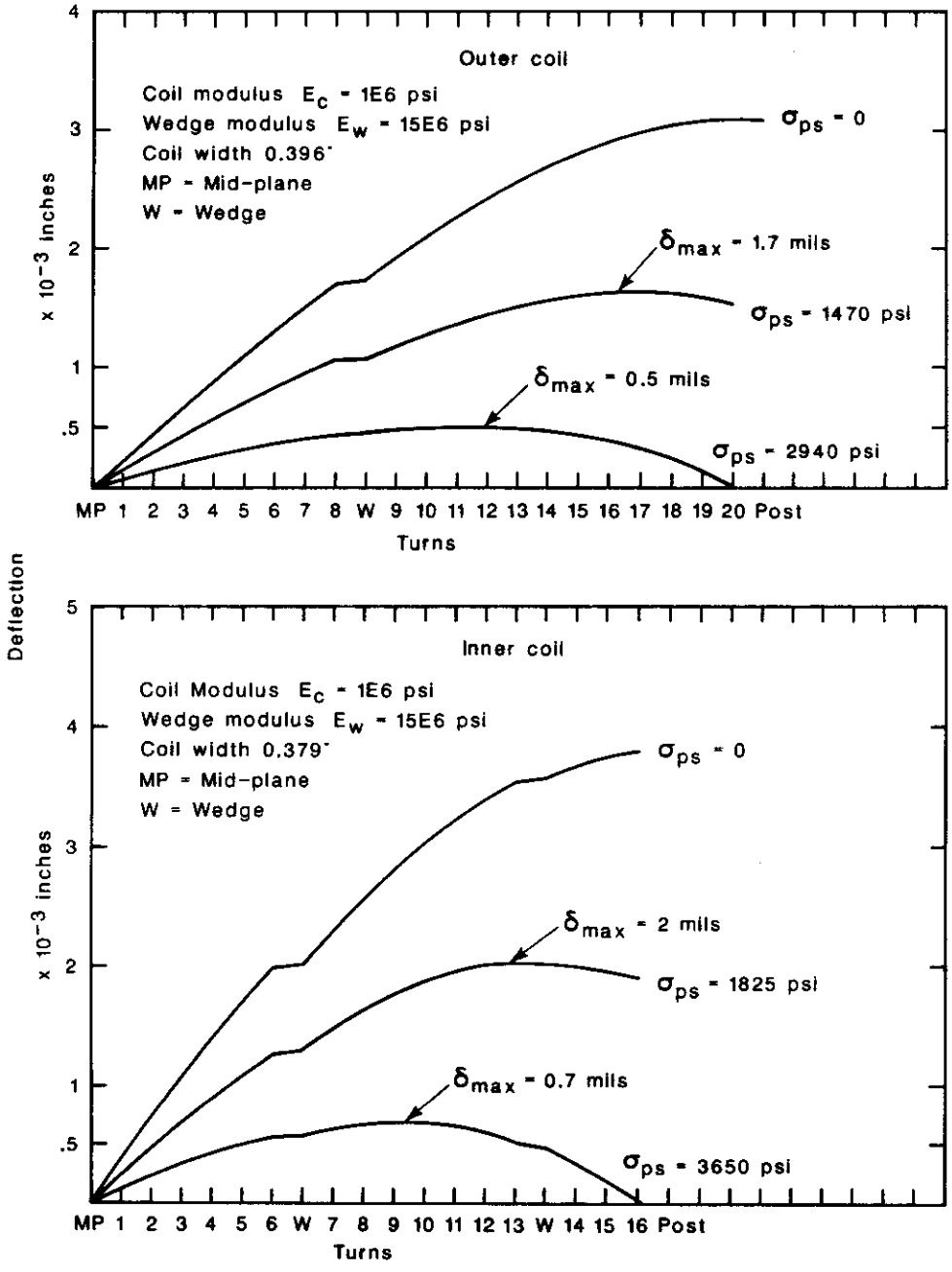

Figure B.6-4. Coil deflections for various prestress levels at 6.5 T.

The thermal loss of prestress in the coils is a function of the difference in thermal contraction between the coils and collars, and the change in the modulus of elasticity of the coils from 293 K to 4 K. Measurements of cured coil stacks compressed under the same load that is seen in assembly indicate the transverse (circumferential) thermal contraction of the coils to be about 0.75 mils per inch greater than the stainless steel. The thermal contraction of the coils in the longitudinal direction matches that of stainless steel. Measurements of the elastic modulus of coil stacks at 77 K indicate an increase in the modulus of about 0.5×10^6 psi from an average room temperature modulus of $1.5-1.2 \times 10^6$ psi. Preliminary calculations predict thermal coil stress losses not to exceed 1500 psi [B.6-2].

The other source of prestress loss is stress relaxation. The time between coil collaring, and when the magnets are installed in the ring and cooled down, could be as long as several years. The coils must have sufficient prestress remaining at the end of this period. Strain gauge measurements of collared coils under load show that the loss of prestress over several days due to stress relaxation at room temperature is about 15%. Experiments with CBA and 3.2 cm bore SSC coils clamped in iron over time periods of months at room temperature, show stress losses of about 25% [B.6-3].

With the above information the minimum amount of prestress necessary at assembly to fully restrain the coils from releasing at the posts at 4 K and 6.5 T can be determined. By adding the calculated thermal loss, 1500 psi, to the calculated minimum prestress requirement, and multiplying by 1.33 to allow for long term stress relaxation at room temperature, an assembly prestress value is arrived at. It needs to be noted that these are preliminary estimates only, since further calculations and verification of prestress losses due to thermal contraction and relaxation need to be done.

Estimated Assembly Prestress Requirements	
Inner coil	6870 psi
Outer coil	5900 psi

B.6.4 Collar Analysis: Deflections and Stresses

Analysis of the collars was accomplished using the finite element code ANSYS. The purpose of the analysis was to determine, for different collar widths, the deflections and stresses of the collars under different loads. Initial models considered left-right symmetry along the vertical plane and constraints on the collar tab to simulate the collars locked together. Results from this model were used to design the collars. Calculations and measurements made later proved this model inadequate in being able to predict actual collar deflections. However, the model appears adequate in comparing relative deflections between different designs and load cases. Later models considered the entire collar with appropriate constraint equations to simulate the pins which transfer the forces from one collar to the other. The coils were modeled as sections of isotropic cylinders. Conductor angles, friction, and the presence of wedges were not taken into account. The

circumferential prestress and the Lorentz forces are applied to the coil sections which, in turn, load the collars. The modulus of elasticity of the coils was taken as 1.5×10^6 psi. Figure B.6-5 shows the model of the coil-collar cross section.

Two basic load conditions were analyzed. The first considered the keyed collars under a prestress load only. This model was loaded with a compressive stress applied on the coil midplane of 9 ksi on the inner coils and 6.5 ksi on the outer coils. These are likely values of prestress that would be reached in assembly. The second load case imposed the 6.5 T Lorentz forces along the coils with the same preload applied at the midplane. The prestress at 4 K will actually be less than the prestress at room temperature. Zero vertical displacement is allowed in the key slots. The horizontal displacement of the tab is constrained to act symmetrically with the opposite side of the collar. This simulates the engagement of the tab with another collar. Initial analysis considered both 15 and 30 mm wide collars in both aluminum and stainless steel. The use of single or dual keys was also considered.

Results from the analysis indicated that a dual key design was preferable. Dual keys kept peak stresses down and made for a stiffer collar. Deflection results showed that a 30 mm aluminum collar with 30% less prestress load at room temperature was roughly equivalent to a 15 mm stainless collar. The lower room temperature prestress load in the aluminum collars is due to the greater thermal contraction of aluminum compared to stainless steel. At room temperature prestress, the collars are predicted to deflect more vertically than horizontally. However, when energized at 4 K, the collars are forced out along the horizontal axis. A summary of the calculated deflections, in mils, in the 15 mm stainless collars for both room temperature loading and Lorentz loading is shown in Fig. B.6-6.

The stresses in the collar were examined at both room temperature loading and Lorentz loading. Because the yield strength of the stainless steel is well above 150 ksi at 4 K, and the coil stresses are less after cooldown, the worst case with regard to stress is at room temperature. With the prestress loading in the inner coil at 12 ksi and the outer coil at 9 ksi, the maximum von Mises' yield stress after the collars are keyed is about 58 ksi at the key slot as shown in Fig. B.6-7. The actual yield strength of the material is about 15% higher. With 9 and 6.5 ksi on the inner and outer coils respectively and the Lorentz forces superimposed on the coils, the maximum von Mises' yield stress is 42 ksi as shown in Fig. B.6-8. The collars are designed to operate in the elastic range so that no permanent deformation occurs. Therefore, there is no variation in conductor placement between thermal cycles.

B.6.5 Magnetic Considerations

After the deflections and stresses in the collar are calculated the last consideration for collar selection is the effect it has on the central magnetic field. With respect to the magnitude of the field, the more iron removed, the greater the requirements made on the superconductor to achieve a given field. The plot in Fig. B.6-9 reflects the decreased contribution of the iron to the central field which must be made up by increased performance of the superconductor. The current density J_c, referred to 4.2 K and 5 T, is that which is required in the superconductor for a central field of 6.5 T [B.6-4]. The plot shows that J_c must be 200 A/mm^2 higher for a 30 mm collar than for a 15 mm collar in order to achieve the same central field of 6.5 T.

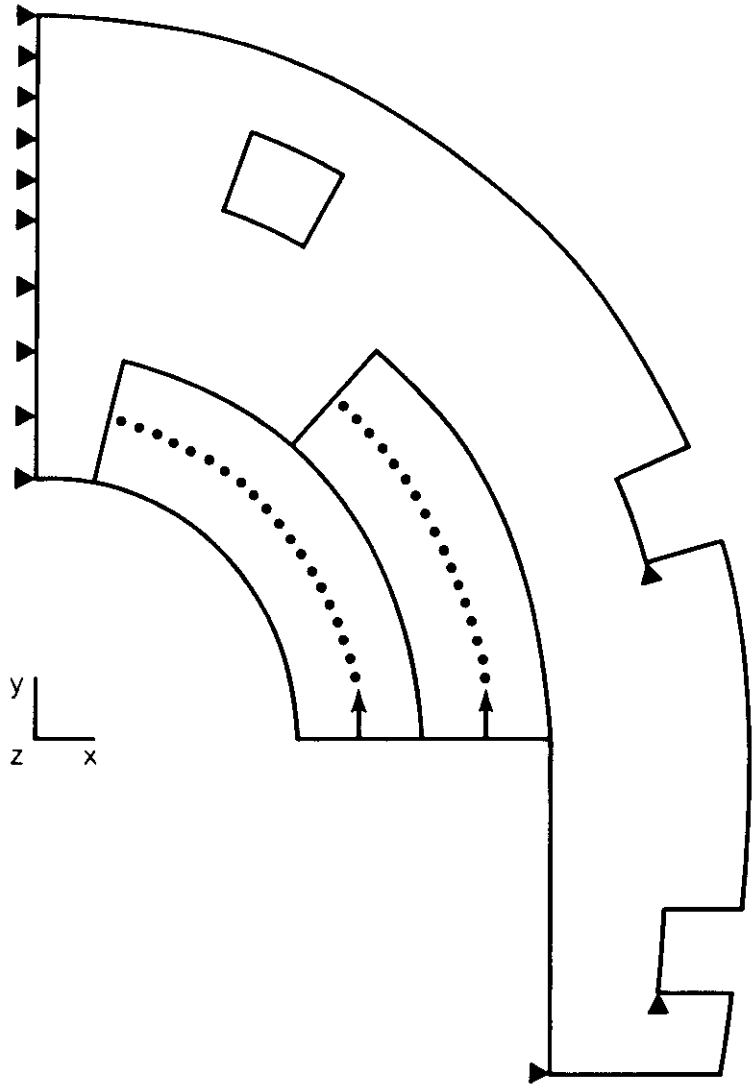

Figure B.6-5. Finite element model of collared coil.

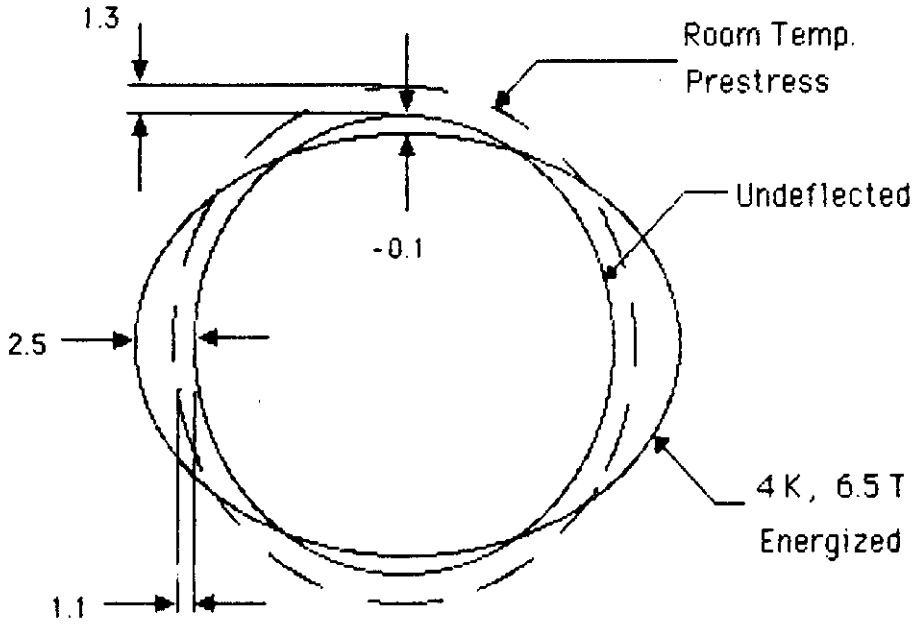

Figure B.6-6. Calculated coil deflections for 15 mm stainless steel collars.

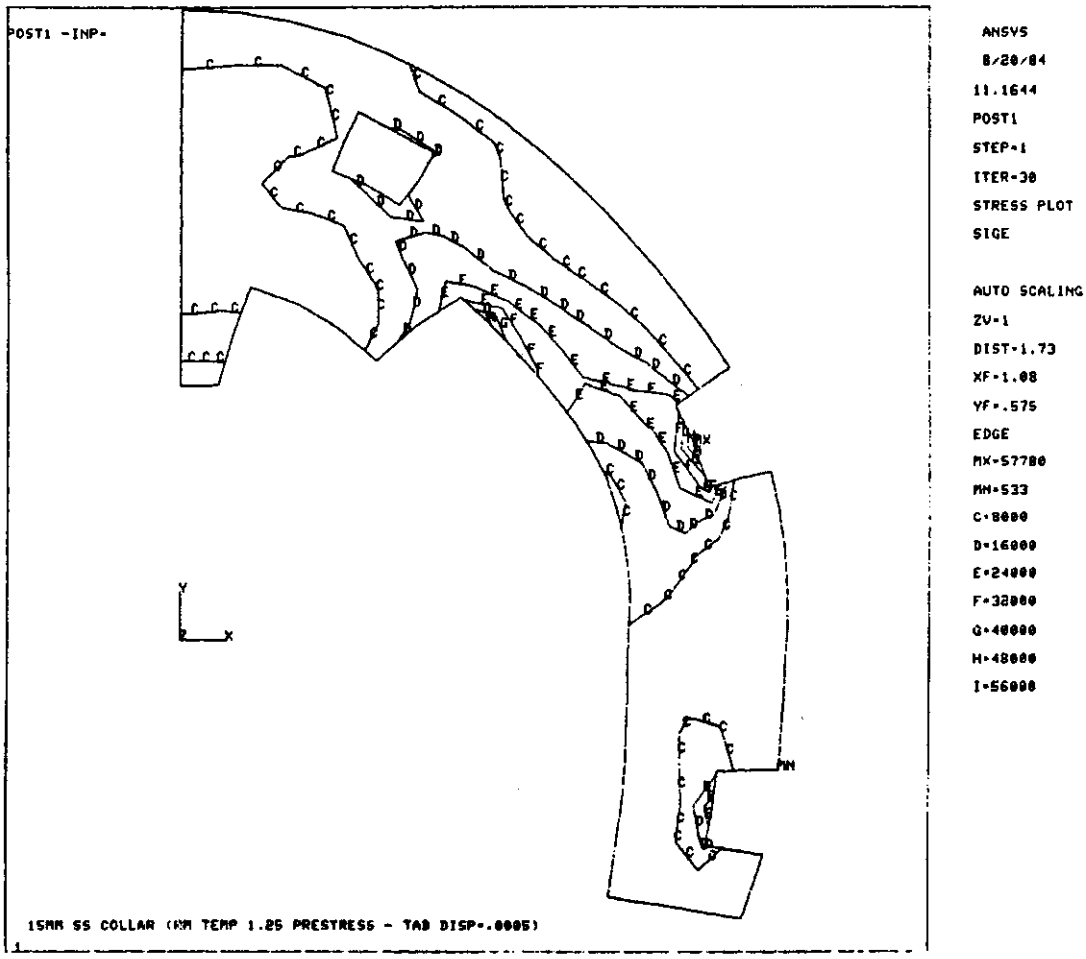

Figure B.6-7. Finite element stress results at room temperature.

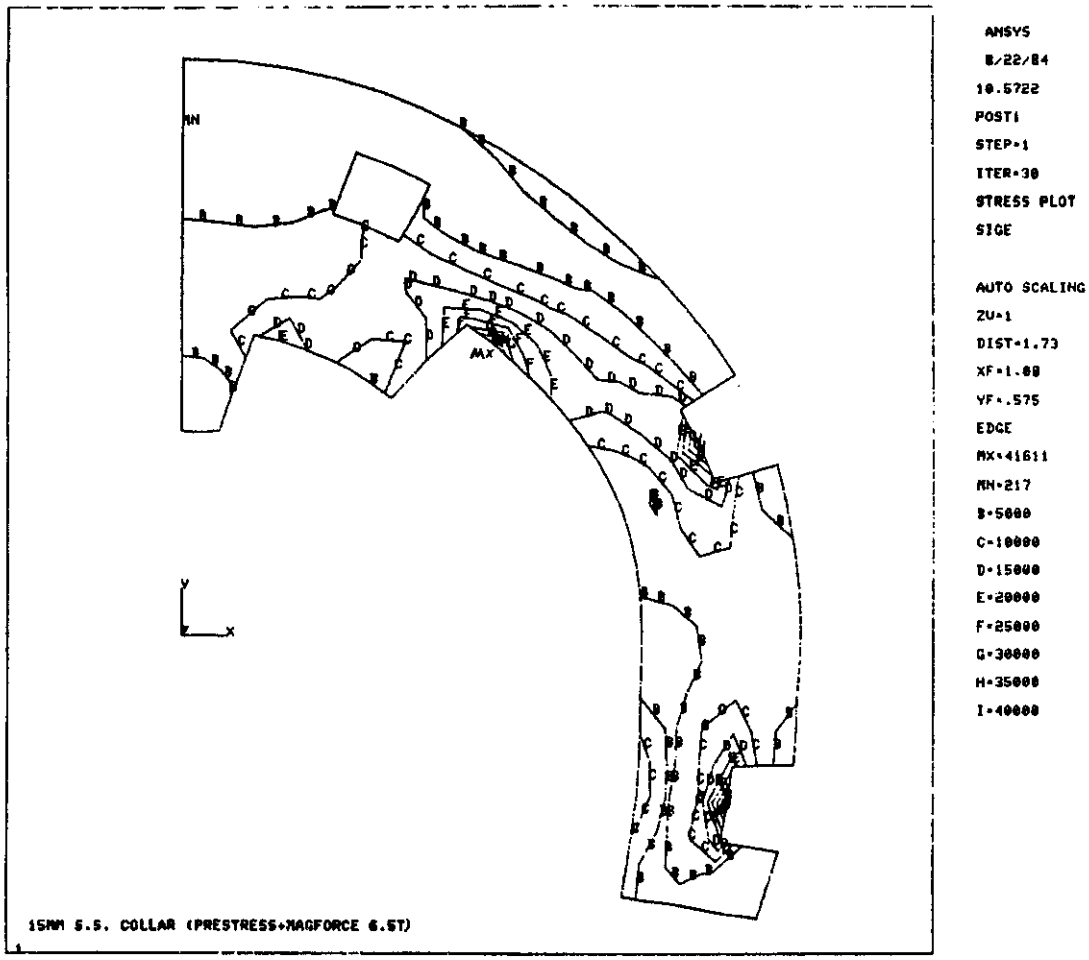

Figure B.6-8. Finite element stress results at 4.5 K.

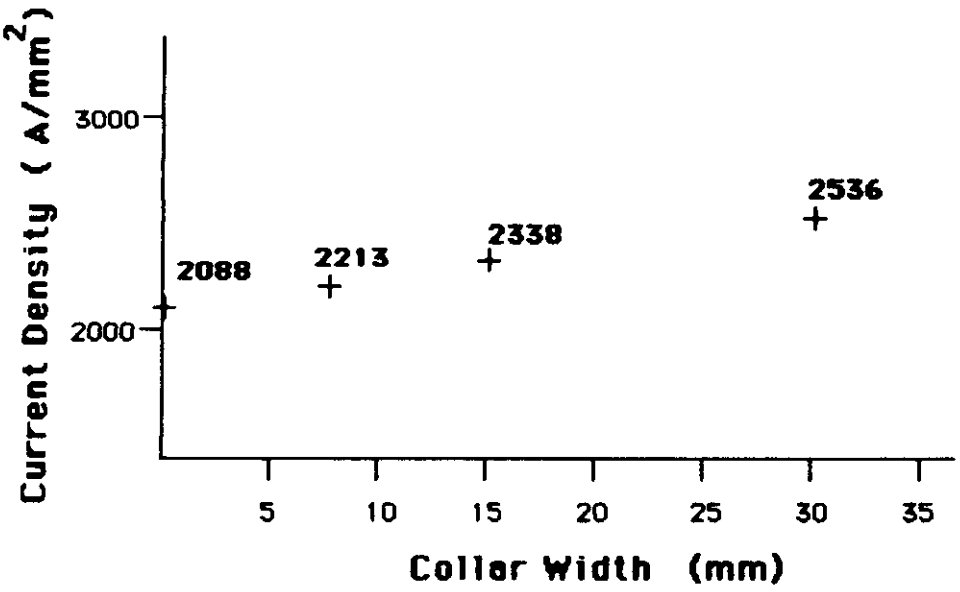

Figure B.6-9. Effect of collar width on superconductor current density.

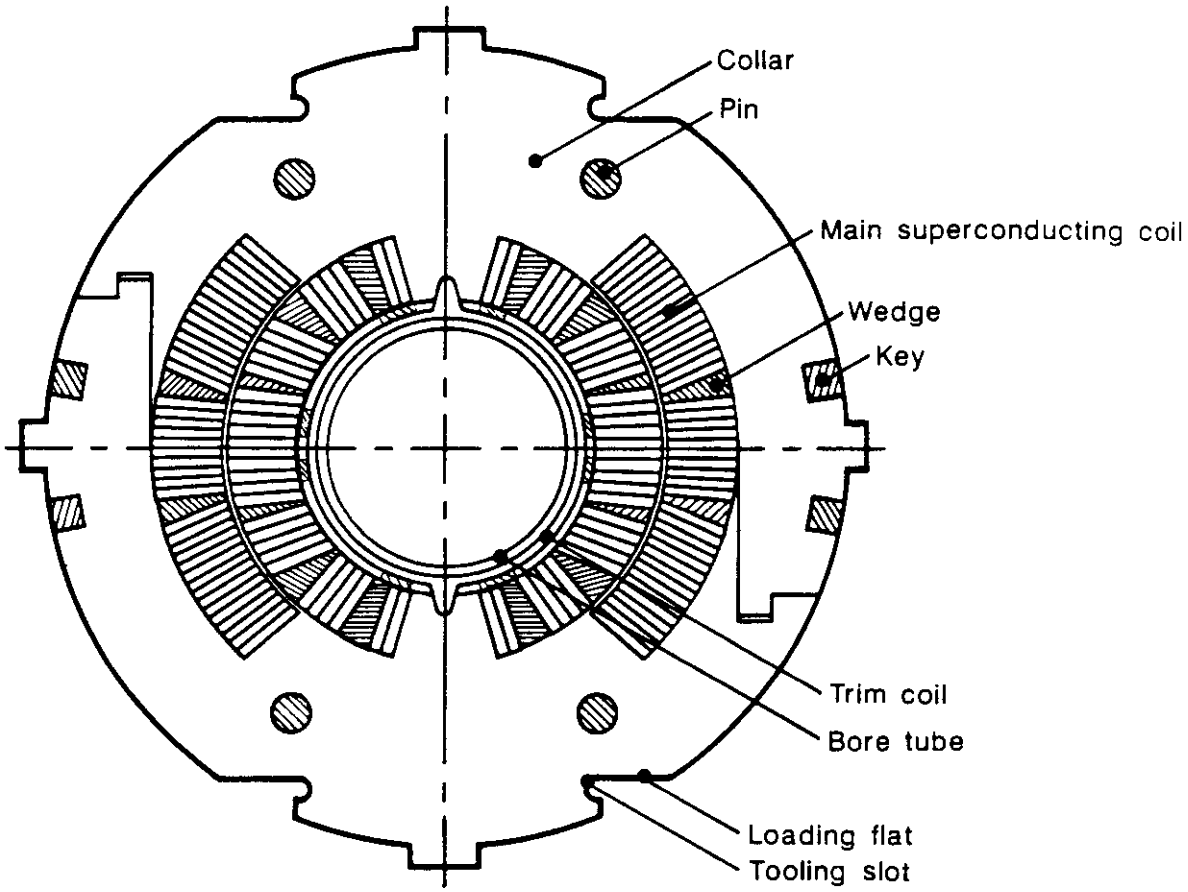

Figure B.6-10. Cross section of dipole coils collared with 15 mm wide stainless steel collars.

B.6.6 Collar Design

The initial calculated deflections indicate that the relative radial motion between the prestressed and the energized condition, for both the 15 mm stainless steel and the 30 mm aluminum collars, was less than 2 mils. Greater than 2 mil deflections were considered to be excessive for both field quality requirements and coil motion with respect to quenches. Therefore, to minimize the field loss, a 15 mm collar was chosen (see Fig. B.6-10). BNL drawing numbered 22-223.02-4 may be consulted for details.

The collar (Fig. B.6-10) is stamped out of 16 gauge (0.059 in. nominal thickness) steel. The two key slots are positioned and sized so that when the collars are bottomed out at the tabs, the coils are over-compressed by 2 mils and a 0.1865 in. key has 2 mils of clearance for insertion. The holes allow for a nominal one mil diametric running clearance for the pins which transfer the force between alternating collars. Symmetry is very important in the collar design. Symmetry insures ease of assembly and proper alignment of the collars as they are stacked up. The position of the holes and the location of the collar tab is symmetric with respect to the vertical center line within 0.001 in. Without this requirement the collars would not properly lock together and the deflections would increase. The external key tabs on the collar register the collared coil assembly in the yoke to an angular tolerance of ± 0.5 milliradians. The key slot on the inner coil post is to provide for keying of the bore tube to the collared coil assembly.

The diameters of the collar and yoke are dimensioned so that the collars do not bear against the yoke and are therefore self-supporting. The overall assembly is assumed to act thermally as stainless steel. Therefore the difference in contraction between the collar assembly and the iron yoke is 1 mil per inch. The following table, using the previously calculated deflections, predicts the radial gap along the axes in mils between the collar and yoke as the magnet is cooled down and then energized. The value for "collar Δ radius" is the actual radial motion the collared-coil assembly is expected to experience for the condition stated in the table. With a collar radius of about 2.2 inches, the net "4 K shrinkage" used to calculate the radial gap is 2.2 mils due to the 1 mil per inch difference in contraction between the collared coil assembly and the iron yoke.

Predicted Radial Gap between Collars and Yoke[a]
(Radial dim. in mils; undeflected clearance 10 mils)

	Vertical		Horizontal	
	Collar Δ radius	Gap	Collar Δ radius	Gap
R.T. prestress	1.3	6.7	1.1	8.9
4 K shrinkage	−6.5	10.9	−6.5	11.1
4 K energized[b]	−1.4	12.3	1.4	9.7

[a]Energized gap always greater than room temperature gap. Therefore collars are always self-supporting.
[b]Energized-room temperature prestress.

B.6.7 Material Specifications

With the selection of the 15 mm collar design, the stress analysis indicates the need for a high strength stainless steel. Prior experience with CBA indicated that the nitrogen-strengthened austentic stainless steel Nitronic 40, also known as 21Cr-6Ni-9Mn, a product of Armco Inc., met the strength required and exhibited very low and stable permeability down through cryogenic temperatures. A newer and cheaper ARMCO alloy, Nitronic 33, 18Cr-3Ni-13Mn, also meets the strength requirements. The reason for the need of a low permeability stainless is because the collars also serve as the coil poles. The poles need to be as non-magnetic as possible. A variation in the material's coefficient of permeability of ± 0.0003 creates a central field error B_0 of $\pm 1 \times 10^{-4}$ at low field by affecting the transfer function [B.6-5, B.6-6].

Nitronic 33 and 40 are covered by specification ASTM A412. Nitronic 40 is also covered by a preliminary report dated March 1983 from the National Bureau of Standards titled *Structural Materials for Superconducting Magnets.* The following table outlines the minimum mechanical properties of the material as called for by these specifications and gives some actual measured results [B.6-7]. The final column is data from the NBS report on average properties at 4 K. The room temperature yield strength of ASTM A412 stainless steel is about twice that of conventional 304 and 316 grades of stainless steels and the ratio between the two types increases to about 3.5 to 1 at 4 K.

ASTM A412 Stainless Steel Mechanical Properties

	Minimum Specified	Actual Measured	4 K Average
UTS	100 ksi	111–115 ksi	240 ksi
0.2% YS	60 ksi	71–73 ksi	180 ksi
Elong. % in 2 in.	40%	45–46%	~5%[b]
Permeability[a]	—	1.0017	1.0017

[a]Nitronic 33 measured at BNL.
[b]NBS Report NBS IR 78-884.

The loading on the collars will cycle over the life of the SSC due to thermal cycles and field strength variations. Assuming a life of 30 years and two cycles per day for each year, the total number of cycles is of the order of 10^4. The number of days of operation per year will actually be less. However, this number does take into account the extra cycles that will occur during the first years due to startup, and during the final years due to wear. Interim results from the NBS report indicate a stress-controlled fatigue life for notched samples at cryogenic temperatures and a maximum stress of 50 ksi to be greater than 10^5 cycles. Several consecutive collars in a collar pack would have to fail before any damage to the coils would be expected.

B.6.8 Measured Results

As of this writing eight 4.5 m long Design "D" collared magnets have been assembled and tested at BNL. Six 1 m long magnets with the same collar have also been assembled and tested at LBL. Additionally, several six inch long, single collar pack models have been assembled at both labs. From all these assemblies, measurements of collar deflections have been taken to compare with those calculated. The collars have also been instrumented with strain gauges to measure coil stresses.

Room temperature measurements of the collars loaded by the coil prestress gave deflections that were greater than those predicted [B.6-8]. Part of the reason for this difference is due to the clearance and tolerances that are necessary to assemble the actual collars that the model did not allow for (i.e., holes, key slots, tabs). This accounts for 2–3 mils radially on the vertical axis and somewhat less on the horizontal axis. The rest of the difference between measured and calculated deflections is due to inaccuracies in the original model, both in the way it was modeled and in the way loads were applied. Measurements of collars assembled at BNL showed that if the collars are not sufficiently supported radially on the sides, then the collars can be yielded during loading. Therefore, the tooling needs to be very stiff to prevent collar yielding.

Cryogenic measurements of collar deflections on the magnets tested at LBL does seem to agree with those predicted [B.6-8]. Both the relative shape of the deflected collar and the magnitude of its deflections between the un-energized and energized states matches the calculated numbers. The table below summarizes these results from both BNL and LBL. Note the differences in the measured deflections due to room temperature prestress between BNL and LBL assemblies. This is due to yielding in the BNL-assembled collar from bending during loading in the press. LBL reports yielding in the keyways of the collars which was not observed in the collars assembled at BNL.

Measured Radial Collar Deflections (mils)

	R.T. Prestress			4 K Energized	
	Measured				
	BNL	LBL	Calculated	Measured	Calculated
Vertical	3.5	7.0	1.3	1.1–2.1	1.4
Horizontal	6.0	3.5	1.1	1.6	1.4

The strain gauge transducers in the coils are able to measure both inner and outer coil stresses in the collared coil assembly, primarily during room temperature assembly. Several magnets, both at LBL and BNL, have had strain gauges calibrated to measure coil stresses at cryogenic temperatures. While there is a high level of confidence in the measured stresses at room temperature, there is considerably less confidence in cryogenic measurements due to less experience with these measurements and thermal offsets.

The plot in Fig. B.6-11 gives a time history of the coil stresses from room temperature assembly through cooldown to 4 K. The most obvious feature of the plot is the large difference in the measured coil stresses between when the collars are loaded in the press and when the collars are keyed and the press force is removed. Coil prestress remaining after the collars are keyed is 2–3 times less than the stress measured when the collars are being pressed. While this does not prevent assembly, it results in coil and collar stresses during pressing that are close to, or at their elastic limit. These stresses can lead to electrical shorts in the coil assembly or yielding of the collars. The maximum remaining prestress in the coils immediately after keying is close to the estimated minimum required at assembly that was presented earlier. This means there is no room to provide for a margin of safety for assembly prestresses which can lead to problems later in the production of large quantities of magnets.

Another area that is of interest in the strain gauge measurements is at cooldown. The transducers show losses of 2–5 ksi in the coils, more than those calculated. If this is true, than the assembly prestress requirements need to be raised. Even though it appears that the prestress in the coils at 4 K is below what is required, the magnets reach operating current with little training and good measured harmonics. The reason for this could be due to the small motions in the coils even with 1/2 of the required prestress as shown in Fig. B.6-12.

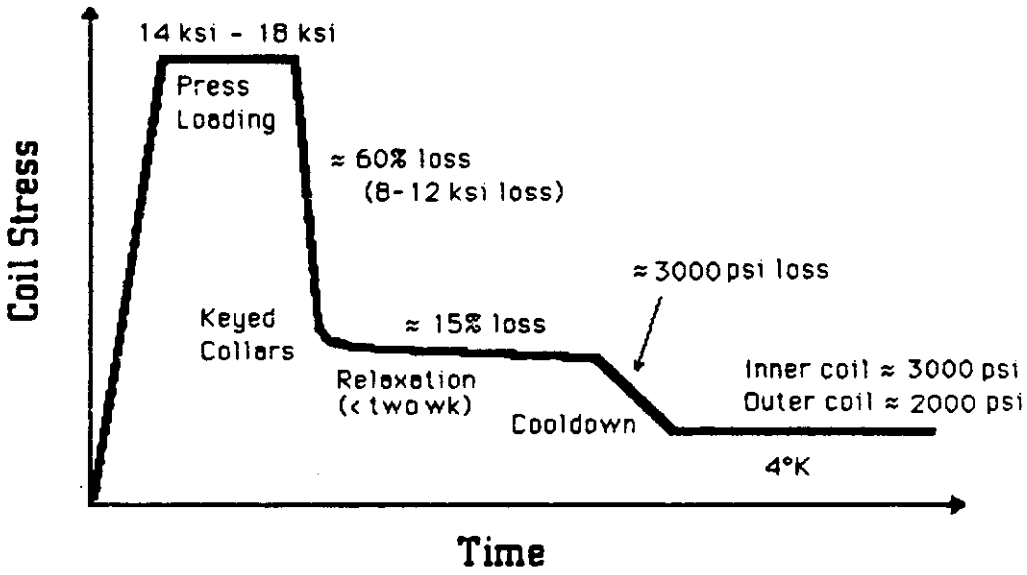

Figure B.6-11. Measured coil loading profile for 15 mm wide stainless steel collars.

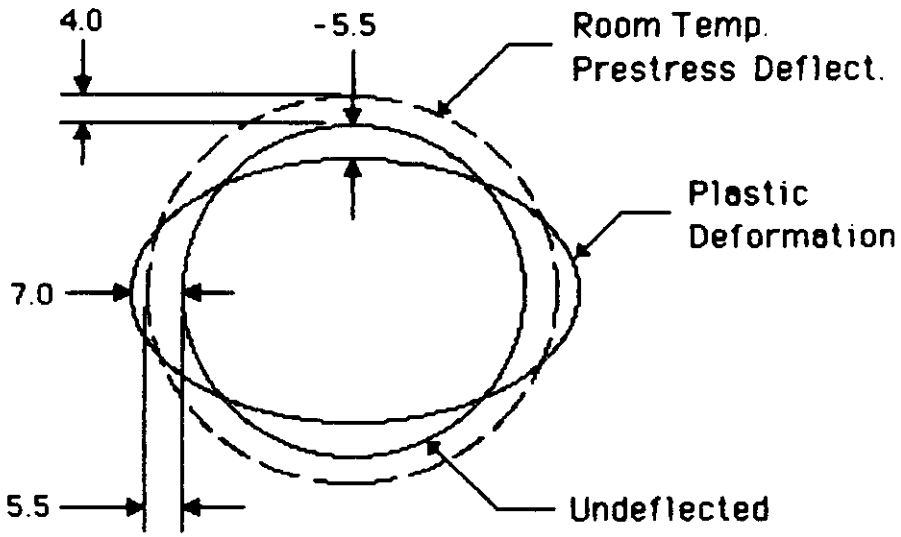

Figure B.6-12. Measured deflections of stainless steel collars.

B.6.9 Assembly Experiences

The assembly procedure and experiences described below are from the 4.5 m Design "D" magnets assembled at BNL. The collar packs are assembled over the coils which have three layers of 5 mil Kapton sheet over them. Between the first and second layer of kapton is placed a 4 mil stainless steel strip heater about two thirds the width of a coil quadrant and the full length of the magnet. The bore tube with its trim package is already positioned inside the coils. The assembly is placed onto a lower cradle which locks on the vertical key tab of the collars to align them down the entire length. This package is then lifted and positioned on the base of the incremental press. The press has an upper cradle which is identical to the lower cradle except in length. It is the length of six collar packs, 36 inches. The cradles serve as the fixtures that transfer the load of the press to the collars during the keying operation. The cradles also serve to restrain the collars during loading. Figure B.6-13 shows a cross section of the collared coil assembly in the cradles and press. The cradles shown in this figure, which will be used in the 16.6 m collar assembly, are stiffer then the cradles used for the first 4.5 m magnets which allowed bending in the collars during loading.

The press is designed to load the collared coil assembly incrementally down the magnet's length. The magnet remains stationary as the top part of the press moves down the length of the magnet guided in the slots machined in the lower platen of the press. The press is capable of applying up to 36,200 lbs. of compressive force per linear inch onto the collar-coil assembly. During the pressing operation with the first magnet, dial indicators were used to measure the deformation of the collars and tooling. These measurements showed that the collars were deformed vertically 20 mils on the radius while being keyed. Horizontally the collars bowed out 5–8 mils on the radius. Experiments with stiffer cradles all but eliminate these deflections during pressing and the resulting yielding in the collars.

Slight rotation in the loaded collars caused the vertical key on the collar packs to grow 2–3 mils. This caused an interference between the key and the mating slot in the yoke. The result was problems in centering the collared-coil assembly vertically in the yoke and closing the two yoke halves over the collars. Yokes for the 16.6 m magnets have wider vertical slots to compensate for this effect.

B.6.10 Further Work

Experience to date has shown that in order to achieve a minimum prestress at 4 K which restrains the coils from motion at the poles, three areas of prestress losses have to be accounted for in order to determine the assembly prestress. The assembly prestress is the coil stress measured after keying. They are: press loading losses, relaxation, cooldown losses.

The press loading losses place an upper limit on the coil prestress after keying. To require greater stress after keying, would mean exceeding the yield limit of both the collars and coils while pressing, and increasing the chances of turn-to-turn shorter in the coils. The losses due to relaxation and thermal contraction place a lower limit on the assembly prestress. To go below this limit would mean the stress remaining in the coils at 4 K would not

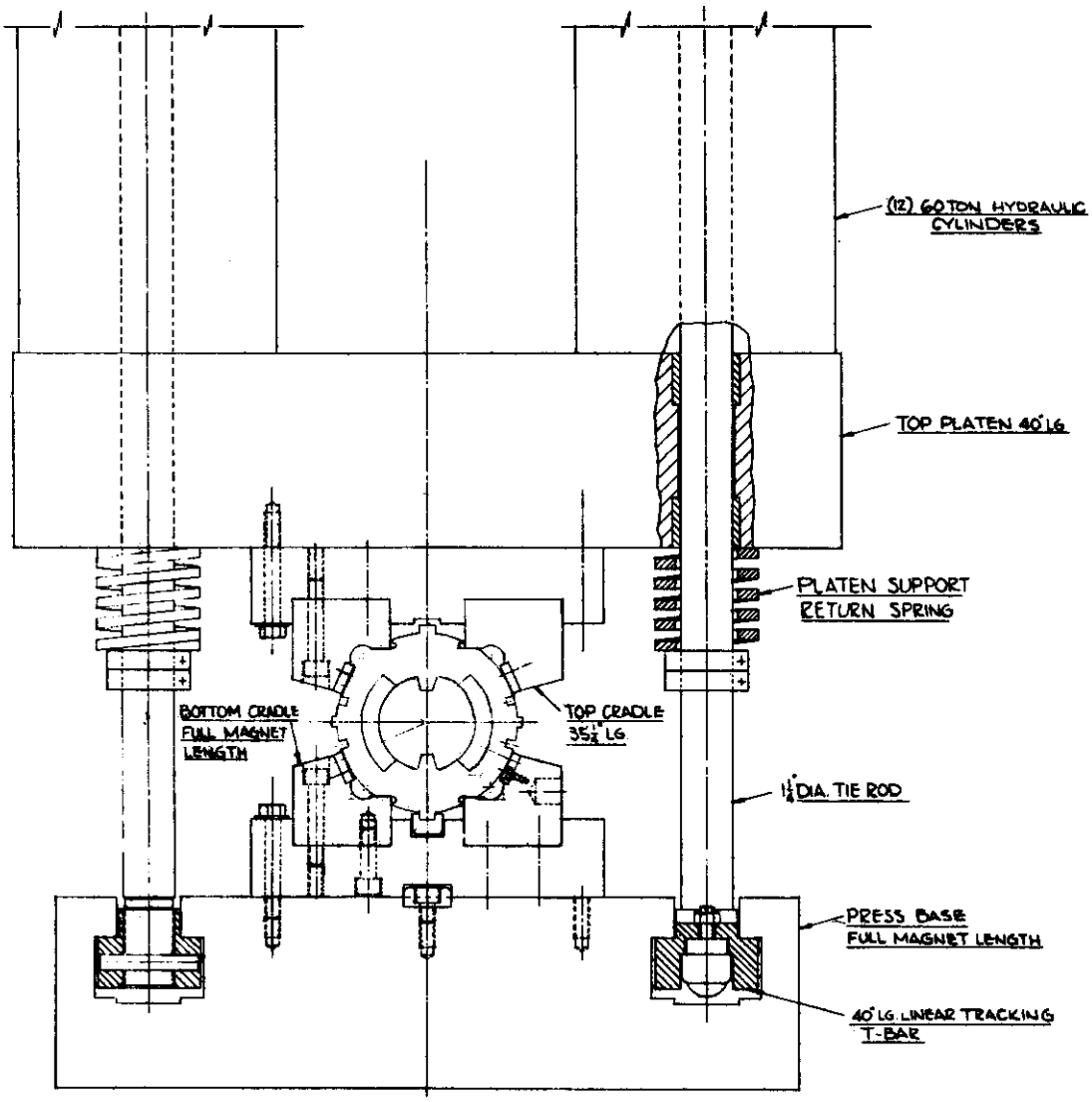

Figure B.6-13. Cross section of coil press for collaring 17 m prototype dipole coils.

be sufficient to restrain the coils from moving at the pole at operating field. The difference between the upper and lower limit is the "assembly window" for assembly prestress. The ongoing work with collars at BNL and LBL is aimed at better defining and/or increasing this window by either verifying or lowering any of the before mentioned losses.

The stress loss after pressing, which accounts for the largest amount of loss, is receiving the most amount of attention. The loss is basically due to a low overall stiffness of the keyed collars. Finite element analysis done at LBL indicates that by welding the collar packs together to prevent rotation around the assembly pins, and at the key slot after assembly onto the coils, makes for a stiffer collar and lowers losses [B.6-9]. Just eliminating any yielding in the collars does not effect stress losses. Experiments at BNL with collars of alternative designs and loading schemes, but of the same 15 mm width, seem to show no appreciable improvement over the current design. Further tests with welded collar packs will be done to verify any improvement in collar prestress losses.

There appears there is little that can be done about prestress losses due to relaxation except to verify the actual losses over long periods of time. It is known that temperature, and possibly humidity, affects the amount of relaxation in the coils over time. Therefore, studies need to be made to properly specify the storage environment so as to either minimize or make consistent the relaxation loss. This will allow for a more accurate specification of the assembly prestress.

Stress losses from cooldown is another area which little can be done in without changing the actual material the collars are made from (i.e., aluminum). However, there is a problem as far as understanding the actual amount of loss. As mentioned earlier, preliminary calculations indicate the prestress loss should not exceed 1500 psi. Strain gauge measurement indicate losses from 2000–5000 psi. While there is considerable doubt as to the accuracy of the measured losses, they need to be remeasured in controlled experiments and verified before a final determination of the assembly prestress can be made. At present, the cooldown losses contribute the greatest amount of uncertainty in determining the assembly prestress.

As an alternative design, LBL is considering an aluminum collar of the same 15 mm width. Calculations by LBL indicate that the increase in prestress resulting from cooldown is more than sufficient to offset the greater press loading losses due to the lower material stiffness [B.6-10]. The result is a larger "assembly window" for prestress. Models need to be made and tested to verify these predictions. While the collar deflections at room temperature should be about the same in the aluminum collars as in the steel collars because of a lower required assembly prestress, the deflections due to Lorentz force loading will increase by a factor of three. It needs to be considered if this deflection is allowable or if it needs to be constrained.

B.6.11 Conclusions

The collars seem to have worked quite well in the eight 4.5 m magnets built at BNL and in the six 1 m magnets built at LBL. At BNL, the magnets trained to the short sample limit in less than five quenches typically at 4.5 K. The eighteen measured harmonics were better then predicted in both their average values and their repeatability between magnets except $a_1 - a_3$ [B.6-11]. The $a_1 - a_3$ differences were due to vertical centering errors of the collars in the yoke. As previously mentioned, the cause of these errors have been identified

and will be corrected in the 16.6 m magnets. However, there are some weak points in the present design that need to be addressed.

Experiments have shown that yielding in the 15 mm wide stainless steel collars can be eliminated by moving the key slots closer together on the collars and to use tooling with sufficient stiffness to prevent the collars from bowing out horizontally during press loading. A new collar cradle which offers this stiffer support has been built and is being used in the 16.6 m magnet assembly. The key slot change will take effect when the next order of collars is made. The first four 16.6 m magnets will use the present design of collars.

In order to make the collars practical for large production runs, the "assembly window" needs to be better defined and made larger. This is being done by addressing the three areas of prestress loss, press loading losses, coil relaxation, and cooldown losses. With improvements in these areas, or the development of an alternative design, the collared-coil design can move from pre-production status to a full production design.

Acknowledgements

The design drawings of the collars and cradles were done by Vic Scotto whose input was invaluable. Experimental data on the mechanical properties of the coils were taken by Ed Baker. Discussion with Mike Anerella provided insight on coil stresses and assembly experiences with the BNL 4.5 m magnets. Discussions with Gerry Morgan on the magnetic design of the magnet are reflected in the section on magnetic considerations. Thanks goes to Ralph Shutt for spending the time to review this paper and to offer constructive criticisms. Discussions and visits with Craig Peters and Ken Mirk from Lawrence Berkeley Laboratory were most helpful in both the design and understanding of the collars.

References

B.6-1. G.H. Morgan, "The One-in-One SSC Dipole with C5 Coils," SSC Technical Note No. 23, Feb. 23, 1985.

B.6-2. R.P. Shutt, "Azimuthal Coil Prestress and Motion in Superconducting Cos θ Magnets, in Particular SSC Dipoles with Collared Coils, and Prestress Losses During Cooldown," SSC Technical Note No. 42, Feb. 10, 1986.

B.6-3. A. Anerella, et al., "Stress Relaxation Studies of CBA and SSC Coil Sections," IEEE Transactions on Nuclear Science, Vol. NS-32, Part 2 (1985).

B.6-4. G.H. Morgan, "Effect of Varying the Coil to Iron Gap in One-in-One Dipoles," Magnet Division Note 114-1, Jan. 7, 1985.

B.6-5. Private communication with G.H. Morgan.

B.6-6. R. Gupta, "Effect of the Steel Collar on the Magnetic Properties of SSC Dipole," Magnet Division Note 153-1, Aug. 5, 1985.

B.6-7. Measured data from material certification reports supplied by Armco Electrical Steel Division.

B.6-8. C. Peters, et al., "Design and Performance of 40 mm, 6.5 T, Collared, Cold-Iron Model Magnets," Lawrence Berkeley Laboratory, submitted to the 1985 Particle Accelerator Conference, Vancouver, Canada.

B.6-9. C. Peters, "Design of 15 mm Collars for the SSC Dipole Magnets," LBL-21030, SSC-MAG-66, Jan. 1986.

B.6-10. *Ibid.*

B.6-11. P. Wanderer, "Summary of Quench Performance and Field Quality Data From 4.5 m R&D Magnets," Feb. 12, 1986, Appendix to SSC Conceptual Design Report.

B.7 Azimuthal Coil Prestress and Motion in Superconducting Cosθ Magnets, in Particular SSC Dipoles with Collared Coils*

R.P. Shutt
Brookhaven National Laboratory

December 4, 1985

In a recent SSC technical note, SSC-N-116, formulas are derived for calculations of coil motions when a "cosθ" dipole is azimuthally prestressed and powered. It is assumed that a distribution of azimuthal Lorentz force components has been calculated from field distributions and currents. Azimuthal stress distributions and minimum prestress to minimize coil motion are calculated, as well as coil motions if applied prestress is less than the minimum value. Angular location of maximum coil motion for different prestress conditions is given. Calculations are also discussed for different elastic moduli of spacers used at and near the magnet poles. For a linear stress-strain relationship in the SSC operating range, and for force distributions, which depend more or less on azimuthal angular location only, coil motions are proportional to the square of the coil radius, and minimum prestress is linearly dependent on radius. Coil motion is dependent on the inverse of the elastic modulus, and minimum prestress is independent of it. Radial pressure exerted by the coil is independent of the radius. Since integrated coil forces are proportional to coil radius, friction effects, therefore, would begin to become important at higher fields for smaller magnets. Since motion decreases with the square of decreasing radius, heat energy produced by friction is much smaller for smaller magnets. Generally, from the point of view of the present considerations, smaller magnets should encounter fewer difficulties than larger ones. For the stainless steel-collared SSC dipole, maximum coil motions vary from approximately 0.002 in. at the poles without prestress to 0.0003 in. to 0.0004 in. at smaller angles, with minimum or more prestress. More than minimum prestress has no direct effect on coil motion but will increase friction forces. Minimum calculated prestresses (at SSC operating temperature) are about 3000 psi. For non-metallic pole spacers (with smaller elastic modulus), coil motions increase only by a few tenths of a thousandth of an inch, which is a small fraction of the expected magnet construction accuracy.

Loss of prestress due to cooldown of coil-collar assemblies has been calculated, also taking into account increases of the elastic modulus indicated by measurements of straight conductor stacks at BNL. If for actual collared magnet coils the average modulus also

*Summary of SSC Technical Note No. 116

increases, coil prestress could be gained rather than lost during cooldown, especially when starting with prestresses which are larger than the required minimum. If the coil elastic modulus remains constant at, say, an indicated value of 10^6 psi, a prestress loss of 800 psi is found for stainless steel collars, and a gain of 500 psi for aluminum collars of the same dimensions. For this condition the average stress in the 15 mm wide collar return leg is 7400 psi at room temperature, if one requires 5000 psi prestress for the inner and 4700 psi for the outer coil at operating temperature. For aluminum collars the return leg stress would be 5700 psi which would seem quite acceptable. When cold, the return leg stress would be 6400 psi for either material.

Finally, a procedure is given for considering prestress conditions when the stress-strain relation for coils is non-linear, which will be especially the case for low stress. Calculations will be performed at a later date.

Relevant and illuminating discussions with R. J. LeRoy were highly appreciated.

B.8 SSC "Local" Sextupole Trim Coils

P. Wanderer
Brookhaven National Laboratory

February 14, 1986

B.8.1 Summary

Magnetization currents produce systematic, allowed multipoles in cosθ magnets. Magnetization effects will be largest at SSC injection, and it is planned to correct the sextupole term "locally" with trim coils placed inside the bore of the dipoles. These trim coils can also be used to correct residual sextupole terms in the dipole and to compensate for saturation effects in the iron.

Four 4.5 m early prototype trim coils have been tested as part of the SSC magnet R&D program. The coils were manufactured by the Multiwire Corporation using techniques developed for printed circuit applications. These trim coils are sufficient to correct the sextupole at all fields with a wide safety margin. The allowed and unallowed trim coil harmonics are satisfactory, based on a comparison with dipole magnet tolerances. It is possible to meet the 0.1 mm tolerances for positioning the trim coil in the dipole. Overall, some further R&D work is needed, but the performance of these first four Multiwire trim coils is quite satisfactory.

B.8.2 Sources of Systematic Sextupoles

Magnetization

It is assumed that the NbTi will have 5 micron filaments. The sextupole due to magnetization is largest at the SSC injection field, which is 0.3 T for Design D magnets. The sextupole (b_2) has been calculated by M. Greene to be -4.7 "units" [B.8-1]. (As usual, a "unit" is the multipole field at 1 cm, multiplied by 10^4/Bo.)

In addition to the mean sextupole due to the magnetization currents it is necessary to estimate the variation since, at low fields, it will increase the variation already present from construction errors. There are two sources of this variation in magnetization sextupoles: the magnet-to-magnet variation in critical current J_c and the variation in J_c due to periodic changes in the temperature of the helium. For this note, the variation in critical current is taken to be 10% (σ), somewhat smaller than the value obtained from measurements of the 800 Tevatron dipoles [B.8-1] but very conservative with respect to the HERA contract, which sets 2% as a goal. (The HERA contract assumed that the individual wires for a cable

are selected to obtain a fixed critical current in the cable, as was done in the latter stages of work on CBA.) Thus, the variation in b_2 due to differences in the critical current will be about 10% $\times$ 4.7 = 0.5 units.

The variation due to the saw-tooth change in the helium temperature between the SSC recoolers is much smaller. The SSC Reference Design Study (RDS) gives the maximum temperature change as 0.2 K. For small changes in the helium temperature near 4.5 K, the variation of critical current with temperature is linear and the following relationship holds: $d(J_c)/J_c$ = 0.1 dT(K). Since the magnetization sextupole is proportional to J_c, a $\pm$ 0.1 K variation in temperature leads to a 1% variation in the magnetization b_2 of -4.7 units. The resultant variation, 0.05 unit, is small and its effects are further reduced by the high periodicity of the effect [B.8-2]. The effect of a "hot" cell of magnets, where the temperature excursion may be larger due to a locally poor vacuum, is larger but still small [B.8-3].

Iron Saturation

If the dipoles do not have zero sextupole at maximum field, trim coils will be needed to bring the sextupole to zero. (Chromaticity adjustments are made with lumped coils in the spool pieces.) For Design D magnets a change of 1.9 units in the sextupole over the full range of excitation due to saturation of the iron is calculated [B.8-4]. This can be reduced by the use of an elliptical iron aperture. Even if saturation effects can be eliminated entirely, however, uncertainty in the built-in sextupole (discussed below) will limit our ability to obtain zero sextupole at 20 TeV.

Variation in saturation effects will increase the overall variation in sextupole at 20 TeV, but this effect can be made arbitrarily small by shuffling different heats of the iron. Because shuffling is not free, it is worthwhile to examine the CBA experience with unshuffled iron. Possible effects of saturation variation have been extracted from the data by comparing the widths of the sextupole distributions of the field quality magnets at low field and at full field. At full field the b_2 distribution has a total σ of 2.3 units and at 18 kG σ is 1.9 units, implying a variation in saturation, yoke weight, or some other property at high field of 1.3 units. (That is, adding 1.3 to 1.9 in quadrature gives 2.3.) The saturation change in b_2 over this interval is 54 units. Thus, the saturation σ is at most 1.3/54 = 2.4% of the saturation mean. Applied to Design D magnets, 2.4% of a saturation b_2 of 1.9 units is negligible. (Interestingly, the σ of integral Bdl was much smaller, 0.34%. This distribution is also affected by the iron saturation.)

More generally, the saturation properties of iron are controlled only by the number of iron atoms and, thus, the weight of the yoke and the percentage of impurities (not the details of the iron processing, as at low field). The most important impurity is carbon, but for CBA the low field specification for the carbon content was tighter than the specification needed at high fields. However, other impurities are also present, and the CBA hoped-for specifications on at least some of these were not accepted by the vendor.

Dipole Construction Errors

It is necessary to include construction errors in this discussion because they set the scale for evaluating the size of the magnetization effects. It is useful to begin by estimating the residual systematic sextupole which is present because of unknown differences between the design and construction of the coil. For many reasons there is likely to be at least one

iteration in the coil cross section. Based on the CBA experience with such an iteration [B.8-5], it can be assumed that the sextupole will be zero at high field within ± 4 units. (It is desirable to minimize the sextupole at high field because this minimizes the J_c requirements for a "local" trim coil.)

A large effort has been made to estimate the rms variation in multipoles due to construction errors in SSC cosθ magnets. Three independent estimates have been made. They are discussed in detail in the Aperture Workshop report [B.8-6]. The estimated variation in b_2, 2.01 units, is somewhat larger than the results obtained from six 4.5 m SSC Reference Design D magnets, for which a σ of 1.24 units was obtained [B.8-7].

B.8.3 Results From 4.5 m SSC R&D Trim Coils

Trim Coil Description

Two different types of externally-powered trim coils have been tested in 4.5 m-long Reference Design D dipoles. The first three trim coils tested were wound by hand around the appropriate spacers placed on the cold bore tube. The coils were secured to the bore tube with epoxy-impregnated Kevlar, as was done for CBA trims. The trim coils were positioned in the dipole using the same methods as for the Multiwire trim coils, described below.

Four trim coils manufactured by the Multiwire Corporation have also been tested. These trims take advantage of an industrial process which is an offshoot of printed-circuit technology and allows wires to be placed in a layer of fiberglass and epoxy with greater accuracy (± 0.001 in.) than can be achieved with the method used for the first trims. The wires are bonded to a flat rectangular section of substrate as shown in Fig. B.8-1 and secured to the bore tube with epoxy-impregnated Kevlar. Accurate positioning on the bore tube is achieved by positioning slots cut in the substrate onto guides attached to the bore tube. The coils are keyed to the dipole collars at the top and bottom (Fig. B.8-2). Spacers between the trims and the main coils limit flexure during operation.

Primarily, the results presented below will be those from the Multiwire trim coils because these coils were manufactured with mass-production techniques. In certain instances, results from the hand-wound coils will also be presented.

Systems Considerations

The requirements imposed on SSC controls and cryogenic systems are quite small. The tracking of the dipole by the trim need not be changed, once it has been determined, and 0.0001 accuracy is sufficient. A single cryogenic loop already has 43 other trim circuits. The leads add 0.4% to the 4.5 K cryogenic load and nothing to the 80 K load.

Trim Coil Quench Results

Trim coil quench currents have been determined at three values of the dipole field: injection (0.3 T), midfield (2 T), and close to peak field (5.8 T). Maximum trim coil operating currents have been determined from these results, assuming bipolar operation of the trims. The hand-wound trims operated at more than five times the required current in dipole fields above 6 T. The results obtained from the fourth multiwire trim coil, and a comparison with the required currents, are given in Table B.8-1. The quench current at

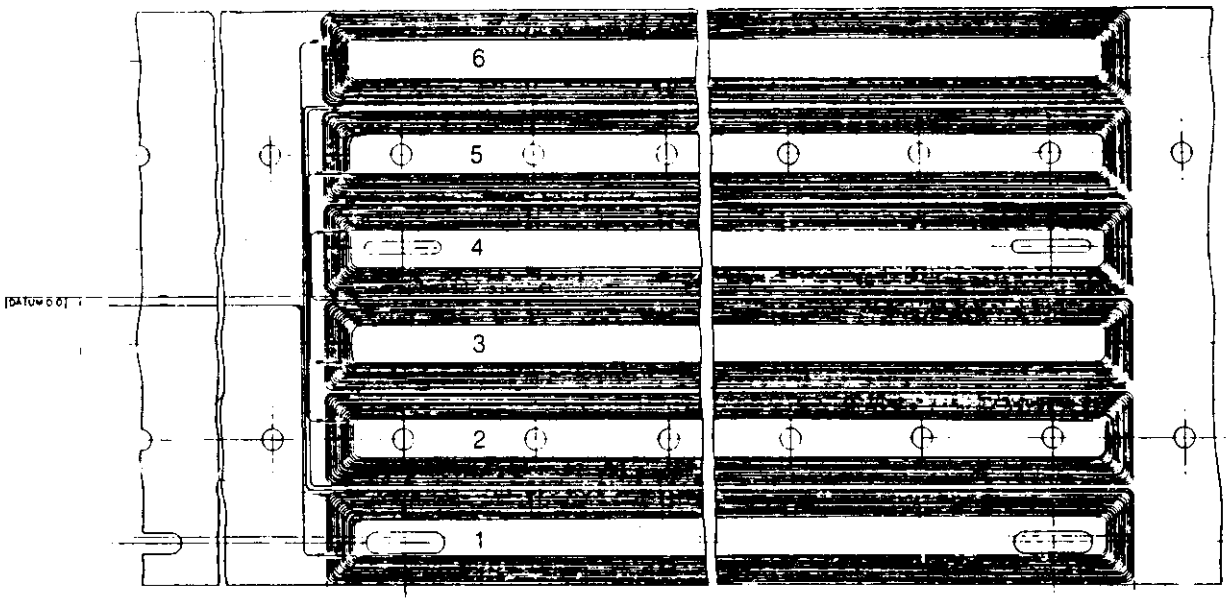

Figure B.8-1. Sextupole trim coil pattern produced by high speed, automated device.

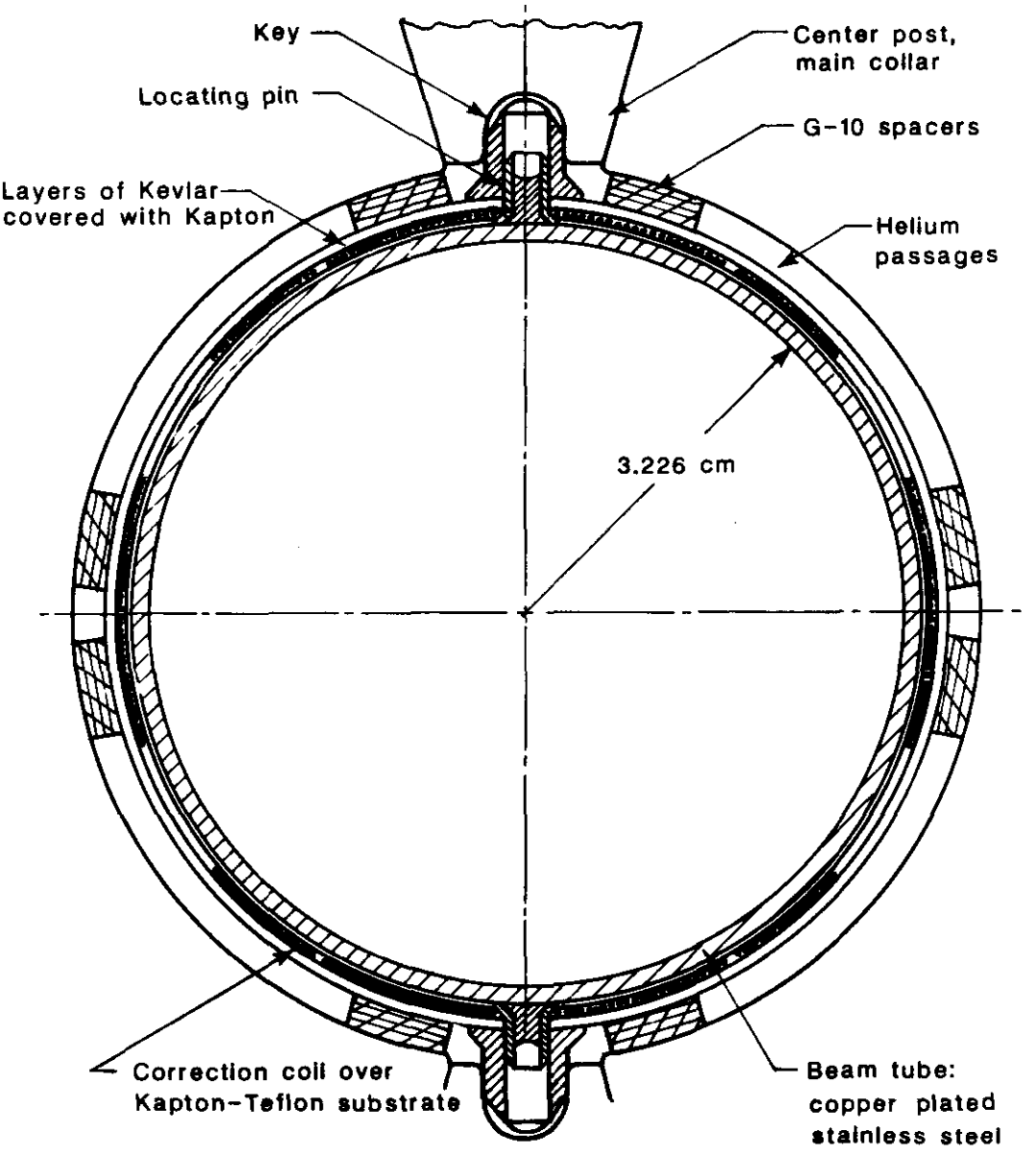

Figure B.8-2. Dipole bore tube assembly, including sextupole trim coil.

5.8 T is at the short-sample limit. The trim coil operates with a large safety margin at all dipole fields. (At 5.8 T, the trim coil exceeded 10 A after one quench; a number of additional quenches were required to reach the short-sample limit. Also, during testing of this coil it was discovered that the heat leak from the "warm finger" of the measuring coil had a significant effect on the trim coil quench currents. Quench data from the first three multiwire trims suffer from the same defect and are not reported here. The data given in Table B.8-1 were taken with the warm finger removed.)

Table B.8-1

	Trim Coil Current (A)	
B_o (T)	Maximum achieved	Required
0.3	66	0.3
2	34	2
5.8	16	4

Trim Coil Multipole Results

This section discusses first the allowed harmonics (b_2,b_8), then the unallowed harmonics which result from trim coil placement errors, and then the remaining unallowed multipoles, which have been analyzed through the 18-pole. In the absence of an explicit list of sextupole tolerances, the multipole variations expected from the dipole are taken as the point of reference.

The mean value of the transfer constant is 5.57 ± 0.09 G/A at 1 cm. The typical sextupole correction is 5 units of sextupole, and the 1.5% rms variation in the transfer constant is much smaller than the magnet-to-magnet variation due to construction errors in the dipole. Hence the variation of the trim coil transfer constant is satisfactory.

The normal 18-pole term, b_8, is the next allowed multipole. The amount of b_8 produced is small, about 0.005 units at the maximum trim coil operating current over the whole range of dipole field. This is negligible in comparison to the estimated dipole construction tolerances of 0.02 units.

Sextupole trim coils which are not correctly positioned in the dipole field produce normal and skew quadrupole and skew sextupole terms. An rms construction tolerance of 0.1 mm for centering and for rotation at a 17 mm radius generates about 0.2 units of each of these three multipoles. This value is small compared with the value of about 0.7 units expected for the dipoles themselves and is thus a useful benchmark. On average, the centering and angular errors in the first three Multiwire trims were 1-1/2 to 2 times larger than 0.1 mm. The placement of the fourth Multiwire trim, which had more accurately punched positioning slots, was better than the 0.1 mm benchmark, as were the hand-wound trims. Thus, trim coil placement methods are expected to be satisfactory.

The average values of the remaining unallowed multipoles are given in Table B.8-2, where they are compared to the rms multipole values expected from dipole construction errors [B.8-6]. In nearly all cases, the trim coil multipoles are much less than those of the dipole. In two cases (a_4,b_5) the trim coils would increase the widths of the distributions by about 25%. This should be satisfactory.

Table B.8-2

Multipole	Trim Coil Average ($10^4/B_o$)	Dipole rms Width ($10^4/B_o$)
a_3	0.26	0.69
a_4	0.10	0.14
a_5	0.02	0.16
a_6	0.02	0.034
a_7	0.02	0.030
a_8	<0.01	0.006
b_3	0.24	0.35
b_4	0.02	0.59
b_5	0.045	0.059
b_6	0.02	0.075
b_7	0.01	0.016

References

B.8-1. E. Fisk and R. Hanft of Fermilab plotted b_2 (440A)-b_2 (4 kA) to remove construction errors from the data and obtained σ/mean = 15%. (Private communication.) A plot of this difference by magnet number shows step-wise changes throughout the production run, in addition to the expected magnet-to-magnet differences.

B.8-2. P. Limon, private communication.

B.8-3. The hottest "hot cell" reduces J_c by the 25% margin allowed in the RDS so that the magnets are at the short-sample limit at 20 TeV. This reduces the magnetization b_2 by 25% to 5.6 units. Taking the difference between -7.5 units and -5.6 units to be the full-width of the "distribution," the "hot" cell σ is a factor of 2.4 lower, or 0.8 units. When the 0.8 units are taken in quadrature with the other sources of variation in b_2, the overall σ is increased less than 10%.

B.8-4. G. Morgan, BNL SSC Technical Note No. 23.

B.8-5. For CBA, the difference between the design and measured values for the ten field quality magnets was 0.8 ± 1.8 units. The A′ cross section shifted the systematic sextupole 25 units from that of the field quality cross section. The difference between the design and measured values for five A′ magnets was 1.9 ± 1.5 units. Thus the offset between design and measured was the same for the two cross sections within 1.1 ± 2.3 units, the limitations being statistical. Hence from CBA we learn that we can maintain a constant value for the difference between design and measured within about 3 units of b_2. This difference will be somewhat larger for Design D magnets because the smaller aperture will lead to larger rms errors and increase the uncertainty in the average measured b_2. Also, there are limitations imposed on the design value of b_2 by the need to have an integral number of turns and the demand that all systematic multipoles be small. (As an example, the PK15 design reduces the b_8 present in the C5 design now used for Reference Design D magnets without increasing the other harmonics, but at the cost of central field.) With these points in mind, the uncertainty in the systematic sextupole is estimated to be ±4 units. (In order to examine changes in the cross section only, CBA data taken with a 30 in. measuring coil have been used. Also, Fernow's calculations TN-337 and TN-403 have been corrected to take into account the shims actually used in the coils.)

B.8-6. H. E. Fisk et al., Magnetic Errors in the SSC, SSC-7 (April 1985, unpublished).

B.8-7. P. Wanderer, appendix titled "Summary of Quench Performance and Field Quality Data from 4.5 m R&D Magnets."

B.9 Magnet Bus Work and Interconnections

M. Shapiro
Brookhaven National Laboratory

March 1, 1986

B.9.1 Main Bus Lead Assembly

The SSC main bus lead assembly extending through a magnet is located at the top of the yoke, which has a cutout to accept the lead assembly. The assembly cross section is as shown in Fig. B.9-1. The two main leads are each composed of a single superconductor cable, laminated with a copper bar which serves as the quench protection bus. A corner of the copper bar is chamfered to provide a helium passageway for cooling the assembly. The amount of copper cross section required for a main bus lead has been determined and is described in the BNL Magnet Division Note 112-9 (SSC-MD-86), *Design of SSC Internal Main Electrical Bus* by J. G. Cottingham. A diode bypass bus is located above the main bus members and is a solid copper bar with the configuration shown. The bus assembly is housed in a duct fabricated of fiberglass-reinforced polyester resin. A minimal clearance fit of parts within the duct is maintained in order to reduce motion caused by magnetic fields. Computations have shown that the minimum allowable electrical surface conduction creep length is 0.20 in. This minimum distance is maintained throughout the bus. The duct slides freely within the yoke in order to accommodate changes in length due to temperature variations. Additional insulation is provided by Kapton wrapping each copper-to-superconductor assembly over its complete length.

The region between magnets is 23 3/4 inches long and is utilized for interconnections for the main and trim bus leads. For monitoring purposes a voltage tap is placed on the bus. It is routed via a ceramic feedthrough from cryogenic to vacuum to ambient environments, as shown in Fig. B.9-2. The feedthrough has a 5 kV electrical standoff rating.

Heat load calculations for the voltage tap show that the expected load for 10,000 magnets is 32.3 W, an insignificant contribution.

B.9.2 Main Bus Flexible Lead Joint

In order to prevent damage to the main leads due to thermal contraction during cool-down, a flexible lead joint is spliced to each main lead in the region between magnets. The joint is "U" shaped and consists of a series of thin (0.020 in. thick) copper strips sandwiching the superconductor bus. The cross section of the copper strips matches that of a main copper bus. Figure B.9-3 indicates approximate spacing of magnets and location of joints.

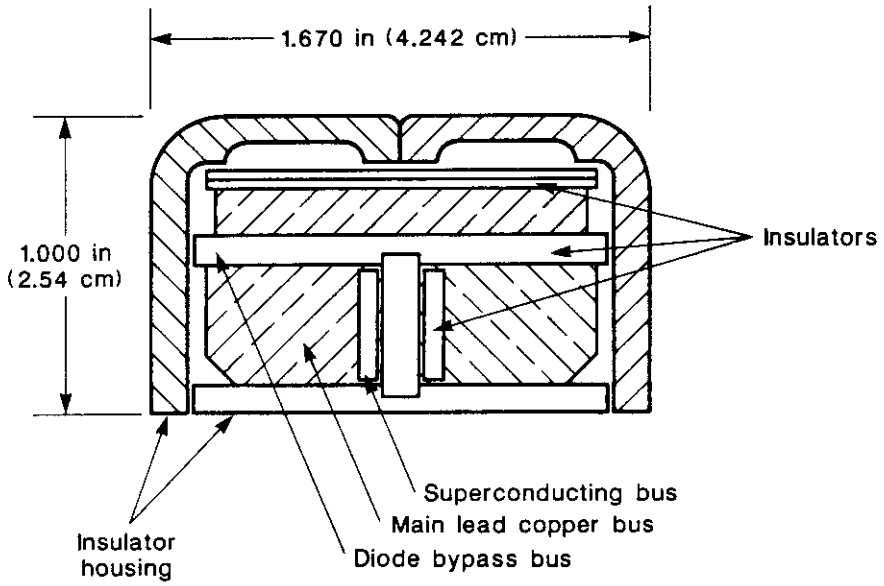

Figure B.9-1. Cross section of main dipole electrical bus.

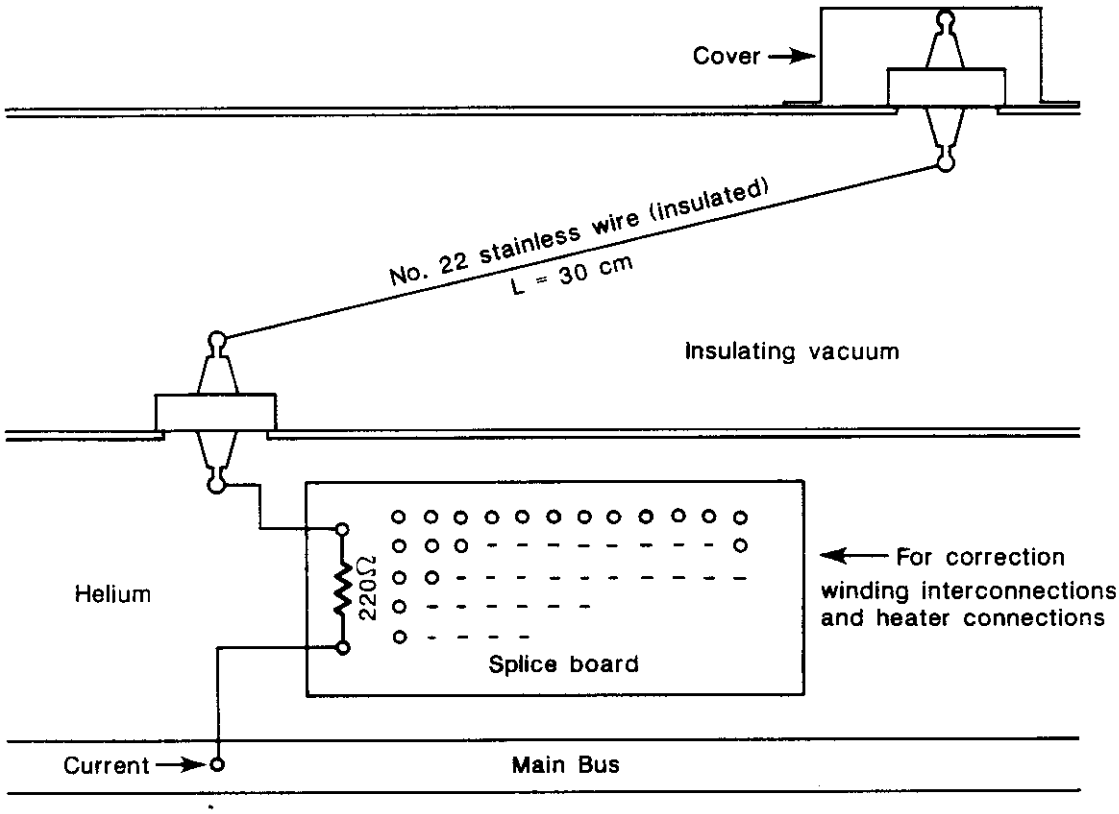

Figure B.9-2. Scheme for routing voltage tap from cryogenic to ambient temperatures.

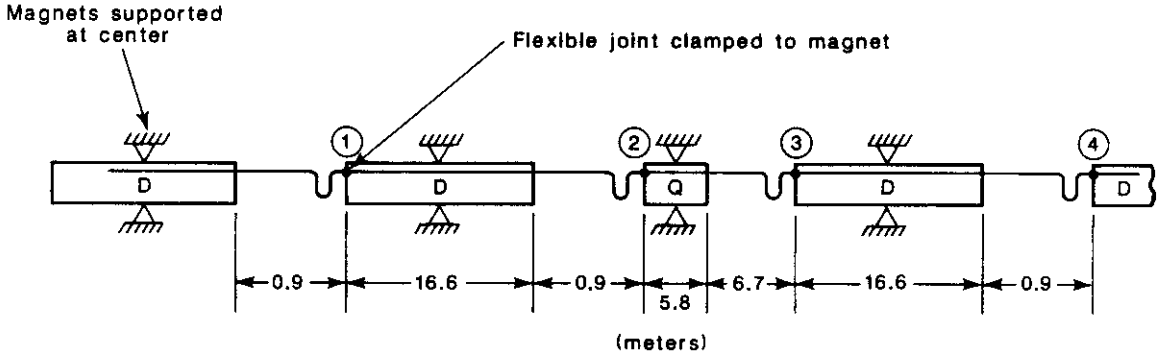

Figure B.9-3. Location of main bus flexible joints along magnet string.

The motions to be absorbed by the joints are determined by analysis of either the contraction or expansion of the leads due to cooldown or warmup. For example, analysis of the contraction mode indicates that the net motion to be absorbed between points (1) and (2) (Fig. B.9-3) is typically 1.60 in., between (2) and (3) 2.24 in., between (3) and (4) 2.25 in.

By pre-springing the joint, that is, compressing it at room temperature to one half of the net motion, the stress developed is halved. Therefore, the maximum flexible joint motion in each leg is approximately ± 1.125 in. with a total motion of 2.25 in.*

The electromagnetic forces to which the flexible joints are subjected must also be considered. Thus, for 5 in. between adjacent joint conductors and 6500 A main lead current, the force is 0.38 lb/in. The interaction of a stray magnetic field at the magnetic end region and the current carrying conductor will result in another force on the joint. A computer analysis of the end region for a 3.2 cm aperture magnet has shown that the average magnetic field in the region in question is 0.02 T. Assuming that the field is oriented for a maximum force on the flexible joint, the force in question is 0.74 lb/in. Adding the two forces results in a maximum possible force of 1.12 lb/in. In order to limit lateral deflections due to the forces discussed each flexible joint is enclosed in a rigid housing.

B.9.3 Trim Lead Bus

The trim lead bus is located in a yoke cutout at the bottom of the magnet and consists of four bundles of superconducting, individually insulated wires. Each individual trim wire is the same type as was used for this purpose in the Colliding Beam Accelerator (CBA) and known as "9 around 1" wire. Each wire is color coded, eight wires in a bundle. At a magnet end the group of bundles are tied together and formed into a thermal expansion loop. The loop is routed along the flexible lead joint but insulated from it. The wires are soldered to a termination board after the loop.

Some correction windings are connected to power leads at mini-lead pots located at the spool pieces. The remainder of the correction windings are connected to regular lead pots at appropriate locations in each sector.

B.9.4 Quench Protection Diode Assembly

Each magnet half cell, composed of five dipole and one quadrupole magnets, contains one protective diode assembly for the dipoles and one for the quadrupole. In the event of a quench the current will be diverted through the diode, preventing damage to any element in the half cell. The diode assemblies are mounted in the helium containment bellows at the spool pieces.

An analysis was performed to determine the amount of copper required for the diode heat sink and is based upon the temperature of the diode not exceeding 448 K. Additional data and assumptions are

1. SSC "worst case" current decay time constant is 40 s, one switch malfunction.
2. $I_{max} = 6500$ A.
3. Specifications for a Westinghouse type RA20 diode.
4. Negligible heat transfer to helium.

*Stress and fatigue considerations are discussed below.

5. The thermal impedance between the diode and copper is 0.02 C/watt.

The results of the analysis indicate that a nine pound copper heat sink will be satisfactory.

B.9.5 Quench Protection Heaters

If a quench is initiated within a coil a distributed "normal zone" must be quickly induced. This is accomplished by accelerating the quench with the use of heaters. The heaters are placed along the coil length in four locations on the outer surface of each outer coil segment. Each heater is fabricated from 0.004 in. thick by 0.770 in. wide stainless steel strip and has a reduced cross section every 12 in. that forms the resistive elements. The heaters are terminated at the magnet end plates.

The heaters are connected into two circuits for each half cell. Connections between the heater leads are made on a termination board located in the interconnecting bellows and the leads are brought out to ambient temperature at the quadrupole magnet locations.

B.9.6 Flexible Lead Joint Stress and Fatigue Study

As previously discussed, a lead joint must be capable of absorbing the expansion or contraction of a main bus. The total lead movement has been previously shown to be 2.25 in. This will be equally divided between the two legs of the flexible joint as shown in Fig. B.9-4. Each leg thus shifts 1.125 in.

By pre-stressing the joint, that is, preloading it at assembly by half the amount of its total movement, the stress in the joint will be minimized. The maximum deflection in each leg from its unstressed position will be 1.125/2 = 0.562 in. Including a margin of safety, the value of 0.625 in. is adopted.

Maximum stress in the joint will occur at the location of maximum moment, which is at the center of the bottom bend, at Section A-A of Fig. B.9-4. This region is not soldered together so as to allow the copper strip members to slide more freely, thereby reducing stress.

Treating the joint as an elastic frame and using the "dummy load energy method" (Ref. B.9-2, pp. 466–468) shows that the deflection at the point of applied load, Δ (in.), is given by

$$\Delta = 224.011 \frac{P}{EI}$$

where p = force on joint due to main bus contraction or expansion (lb), E = modulus of elasticity of joint material (lb/in.^{2}), and I = moment of inertia of cross section (in.^{4}).

As previously stated, the region of maximum moment is not soldered together. However, the copper strips and superconductor cable are soldered together at adjacent regions. To determine the structural characteristics of the joint due to deflection, two extreme scenarios of rigidity were studied and the results "averaged."

The first scenario assumed that the copper strips and superconductor are soldered together in the region of highest stress. In this case, using reasonable parameters for calculating E and I, one obtains $EI = 2.46 \times 10^4$ lb · in.^{2}, and, since $\Delta = 0.625$ in. (by

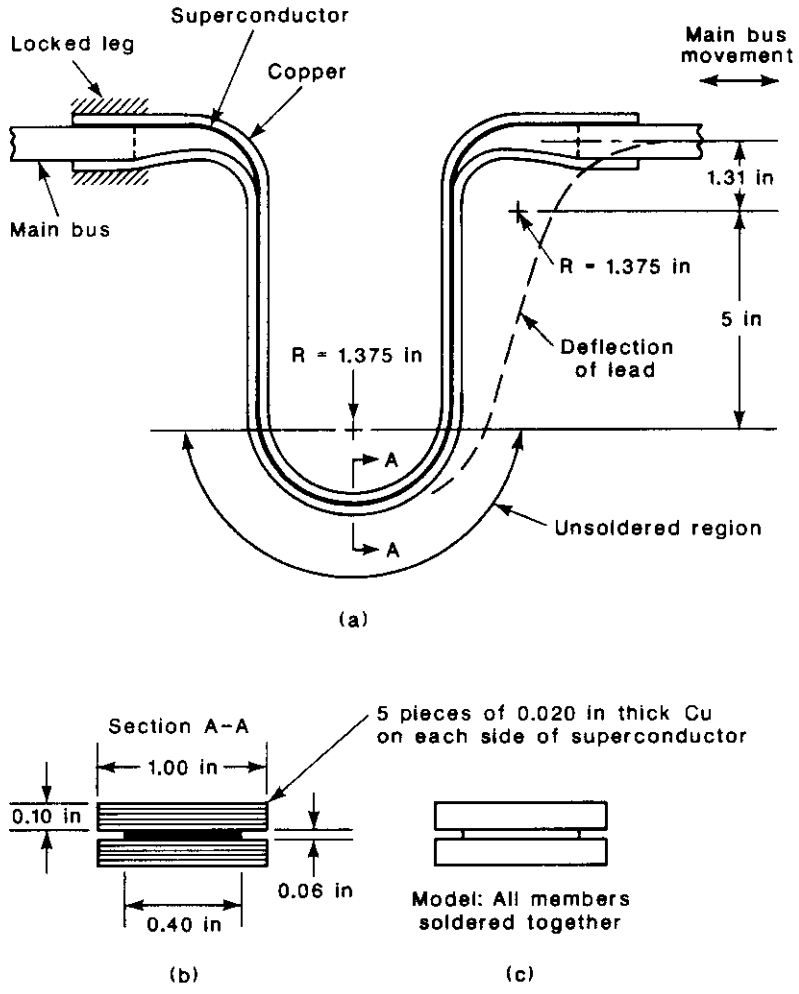

Figure B.9-4. Details of flexible lead joint assembly.

preloading the joint), p = 68.6 lb. From this one obtains a maximum stress, S, of 48,000 psi. (I of the superconductor is ignored compared to that of copper.)

The second scenario assumed that the copper strips and superconductor are not soldered together. Now, a similar calculation gives p = 0.32 lb, and a maximum stress of 3,700 psi. Although the actual amount of rigidness of the lead components is difficult to ascertain, an "average value of maximum stress" will give some indication of the degree of stress in the joint: S(average) $\approx$ 26,000 psi. Using fatigue stress values vs. fatigue cycles for hard, ETP copper from Ref. B.9-4, shows approximately 100,000 cycles to failure at 26,000 psi. This is far in excess of the estimated cooldown cycles required for a magnet during the machine lifetime (3000) and should also provide sufficient margin of safety due to the uncertain structural rigidity of the joint.

References

B.9-1. Selected Cryogenic Data Notebook, 1980, Vol. 1, p. 1X-G-1.

B.9-2. *Advanced Mechanics of Materials,* Seely and Smith, 1952, pp. 466-8.

B.9-3. Properties and Selection of Metals, *American Society for Metals Handbook,* p. 1008.

B.9-4. D. Steinberg, *Vibration Analysis for Electronic Equipment,* p. 445.

B.10 Quench Experiments on a 1-m SSC Model Dipole

W.V. Hassenzahl
Lawrence Berkeley Laboratory

March 1986

This report describes the results of a series of heater-induced quenches on the 1-m long SSC model dipole D-12C-7 constructed at LBL. Test results of the following types are described.

- Quench propagation velocities – axial
- Rate of temperature rise in the conductor

The primary purpose of these tests was to measure quench velocities at a variety of locations and for several currents/fields which can be used to refine the quench predictions for longer magnets.

The D-12C-7 dipole has the proposed SSC Design D conductor and winding cross section. The insulation is the BNL combination of glass and Kapton and is similar to that considered for the final SSC dipole.

B.10.1 Experimental Arrangement

The SSC model magnet D-12C-7 was instrumented with three heaters and a special set of voltage taps. The positions of the relevant voltage taps and heaters are shown in Fig. B.10-1 and the configuration of voltage taps, data acquisition channels and heaters are described in Table B.10-1. The lengths of the regions between voltage taps is indicated for those regions where quench velocities are calculated.

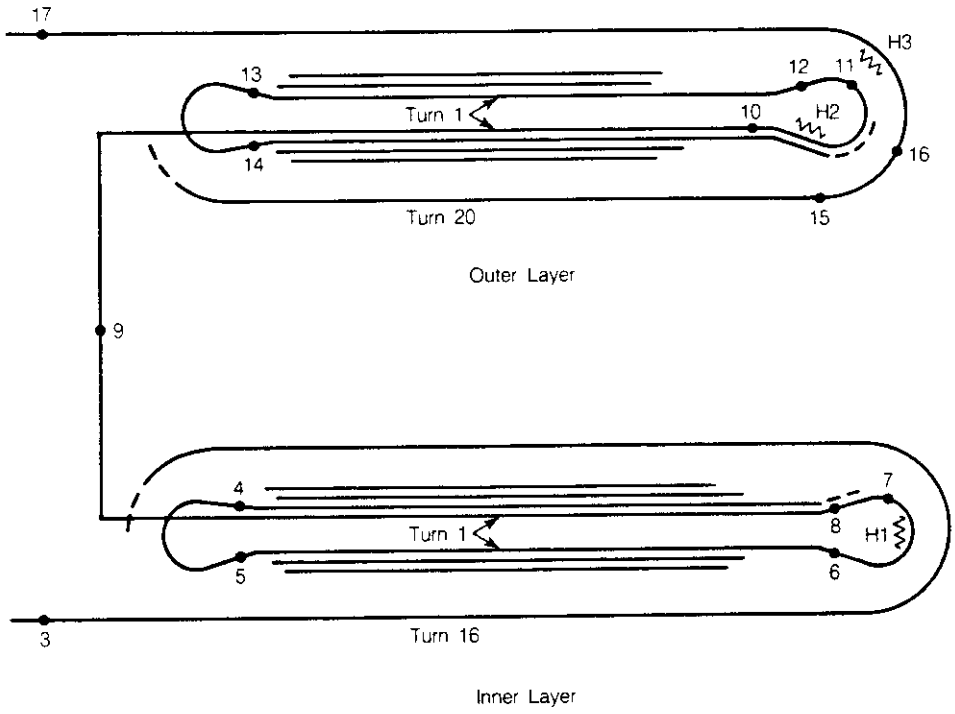

Figure B.10-1. Voltage tap and heater arrangement for model dipole D-12C-7.

Table B.10-1
Voltage Tap, Channel, and Heater Distribution

Taps	Channel No.	Volts, f.s. (V)	Length (cm)	Heater No.
T3-T4	6	50	—	—
T4-T5	7	5	24.31	—
T5-T6	8	5	74.78	—
T6-T7	9	5	—	1
T7-T8	10	5	4.85	—
T8-T9	11	5	—	—
T9-T10	12	5	—	—
T10-T11	13	5	—	2
T11-T12	14	5	5.0	—
T12-T13	15	5	74.80	—
T13-T14	16	5	18.92	—
T14-T15	17	50	—	—
T15-T16	18	5	5.0	—
T16-T17	19	5	—	3

B.10.2 Longitudinal Quench Propagation

Some of the quenches induced in the coil were monitored with our high speed data acquisition system. Some typical curves of the voltages in these events are shown in Figs. B.10-2(a) and B.10-2(b), which are from File D12C7020. The abscissa on these graphs is the time in milliseconds before the quench trigger energized the energy extraction system. To obtain these data, a delay of about 100 ms was introduced between the quench detection and the extraction trigger. In Fig. B.10-2(a) the voltage in the region with heater No. 1, channel 9, begins to rise at -103 ms. The break in this curve at -101 ms shows propagation of the normal region into channel No. 8 [see Fig. B.10-2(b)], and the one at -93 ms reflects propagation into channel No. 10. The inflection in channel No. 10 at -89 ms shows the normal region propagating on into channel No. 11.

Since we know the length of the conductor monitored by channel No. 10 is 0.050 m, and the time to cross it is 0.003 s, the quench velocity is about 17 m/s. Using similar results from other channels and quenches, we obtain the data summarized in Tables B.10-2, B.10-3, and B.10-4.

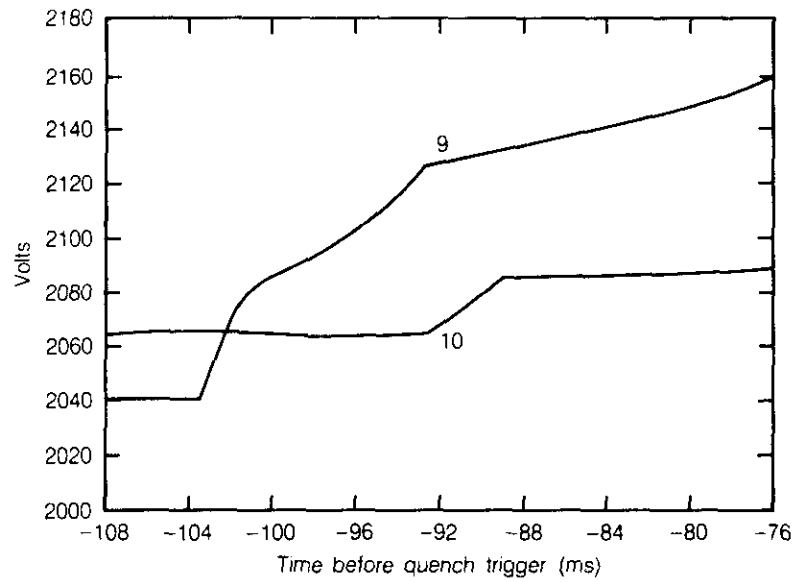

Figure B.10-2(a). Voltage vs time for 6500 A quench in inner coil layer of model dipole D-12C-7.

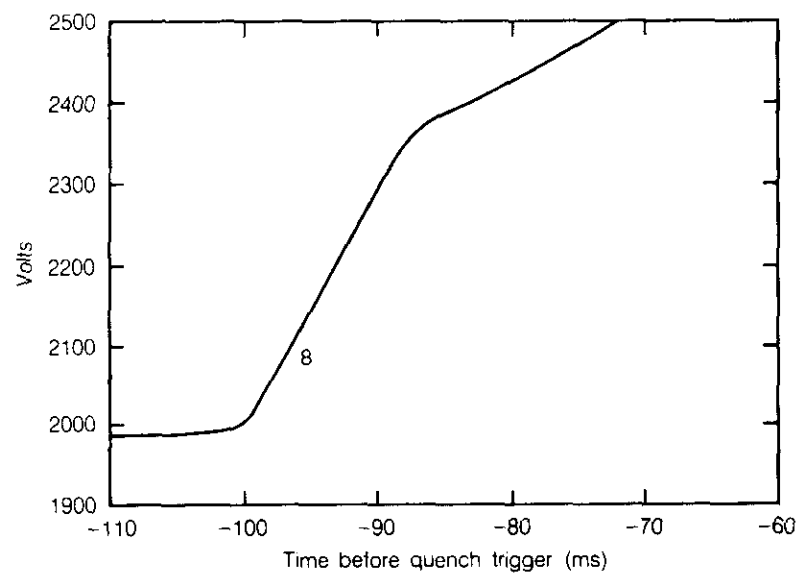

Figure B.10-2(b). Further data on 6500 A quench in inner coil layer.

Table B.10-2
Quench propagation velocities in the axial direction for the outer conductor in the second layer—at the end. The magnetic field is small here, but not known exactly. Perhaps 1 T.

Current (A)	Channel No.	Length (cm)	Δt (ms)	Velocity (m/s)
6000	18	5.0	3.8	13.1
6500	18	5.0	3.6	13.9

Table B.10-3
Quench propagation velocities in the axial direction for the inner conductor in the second layer—at the end. The magnetic field is about 5 T in the straight section* at peak current of 6.5 kA and is probably down to about 3 T at the area of the heater.

Current (A)	Channel No.	Length (cm)	Δt (ms)	Velocity (m/s)
4500	14	5.0	3.2	15.6
	16	18.9	10.0	18.9
6000	14	5.0	1.7	29.4
	15	74.8	14.4	51.9
	16	18.9	3.3	57.3
6500	14	5.0	1.4	35.7
	15	74.8	11.2	66.8
	16	18.9	3.3	57.3

*Note that the training and short sample quenches in this magnet were in the inner turn of this layer—indicating the conductor is near short sample here.

Table B.10-4
Quench propagation velocities in the axial direction for the inner conductor in the inner layer. The conductor is near critical current at 6500 A.

Current (A)	Channel No.	Length (cm)	Δt (ms)	Velocity (m/s)
4500	8	74.78	6.0	12.5
	10	4.85	5.0	9.7
6000	8	74.78	19.2	38.95
	10	4.85	2.2	22.0
6500	8	74.98	13.2	56.6
	10	4.85	3.0	16.2

The rise in voltage in channel No. 10 after −89 ms and in channel No. 9 after −93 ms is due to Joule heating in the conductor and will be discussed in some detail below. The real signals have voltage spikes that are generally thought to be noise in the data channels rather than power supply or magnet induced, though some spikes caused by conductor motion have been seen.

B.10.3 Temperature Rise During a Quench

By observing the conductor in one of the short regions after the quench front has passed it, we can monitor the temperature development with time. As an example, the data from channel No. 14 in data file D12C7021, which was for a 6500A quench in layer 2, is shown in Fig. B.10-3. The quench velocity was 29 m/s. This channel is quite short so we assume the temperature across it is uniform. (There may actually be a gradient, but it should be small as the transition time of the quench across this segment is about 1.7 ms.)

The temperature is estimated by first determining the resistance of the segment from the channel voltage, and the current, which is steady at 6500 A. The temperature is then found by comparing the resistance of the segment to a known curve of resistance vs. temperature.

The estimates of voltage, temperature, etc., vs. time are given in Table B.10-5, and finally the development of the temperature as a function of time is given in Fig. B.10-4. Note again that the current has remained steady during this time so it should be possible to compare this curve to a prediction of a quench in an SSC magnet of arbitrary length.

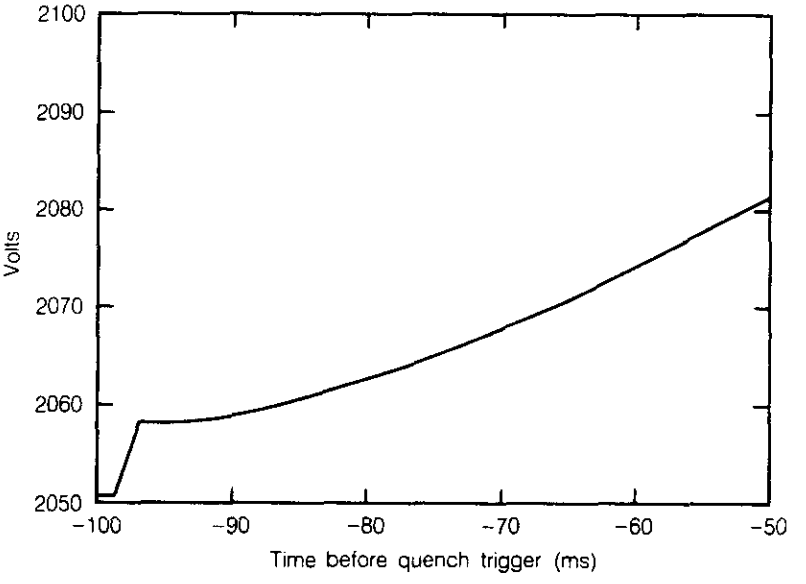

Figure B.10-3. Quench event (6500 A) in outer coil layer of model dipole D-12C-7. The voltage rise after −97 ms shows the temperature increase in this 5 cm long section.

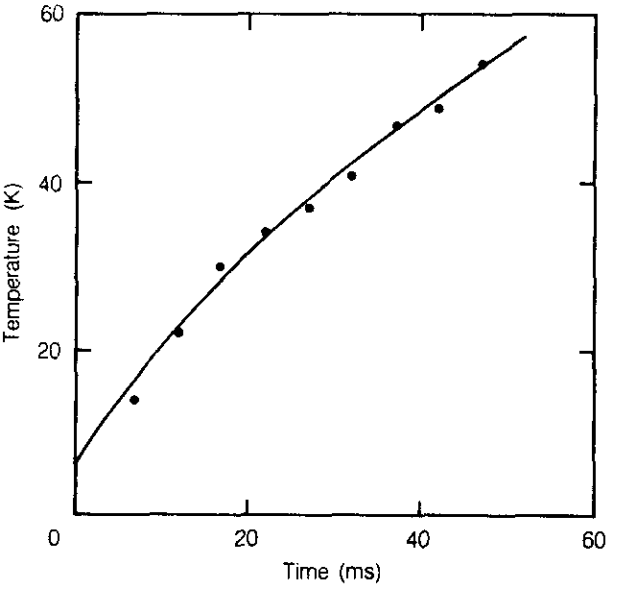

Figure B.10-4. Temperature development in Section 14 of model dipole during a 6500 A heater-induced quench.

Table B.10-5
Determination of quench temperature in 5 cm long channel No. 14, file D12C7021; a 6500A heater induced quench. Note that the resistance is constant up to about 15 to 20 K so the early temperature induction is ambiguous.

Time (ms)	a to d (No.)	a to d (Δ No.)	Voltage (mV)	T (K)	Δt (ms)
−97	59.5	8.0	19.5	6.0	0
−95	58.5	8.0	19.5		2
−90	59.0	8.5	20.7	14.0	7
−85	60.0	9.5	23.2	22.0	12
−80	63.0	12.5	30.5	30.0	17
−75	65.0	14.5	35.4	34.0	22
−70	67.0	16.5	40.3	37.0	27
−65	70.0	19.5	47.6	41.0	32
−60	75.0	24.5	59.8	47.0	37
−55	77.0	26.5	65.0	49.0	42
−50	81.0	30.5	74.5	54.0	47

The temperature rise during 1.7 ms is about 3 K at the beginning of the quench and less than 2 K later. This sets a maximum for the temperature difference across the segment so the assumption of a constant temperature gave reasonable results and the error in the curve due to a temperature gradient can only be about 1 K.

B.10.4 Change of Quench Velocity with Time

The development of quench velocity with central quench temperature is given by

$$V_q = \frac{I}{C}\,\frac{\sqrt{k\rho}}{\theta_c}\left[\frac{(\theta_m - 2\theta_c)}{(\theta_m\,(\theta_m - \theta_c))^{1/2}}\right]$$

where I is the current, C is the specific heat, θ_c is the difference between the critical temperature and the bath temperature, θ_m is the difference between the maximum temperature in the quench region and the bath temperature, k is the thermal conductivity, and ρ is the normal resistivity.

The term in [ ] is usually dropped in the analysis, because it approaches 1.0 as the central quench temperature approaches 20 K. This term predicts, from first principles, an accelerating quench front. The peak velocity is reached in 10 to 15 ms for the quench described in Table B.10-5 and Figs. B.10-3 and B.10-4. A somewhat longer time is required for lower temperature quenches.

Based on previous analyses of quenches in dipoles of the SSC Design D type, it appears that if the quench velocities are as high as observed here, the magnets will be safe with

single or at most double diode protection. To assure safety in all conditions, however, it is necessary to assess some "worst case" scenarios. There appear to be three quench initiation regions that may lead to hot quenches. These are

1. The outer turns of layer 2 at the magnet ends where the field is low.
2. The superconductor that is a connection between magnets and/or between a magnet and the associated shorting diode.
3. The pole turn of layer 1, due to the wedge between turns 3 and 4.

Item 1, and to a certain extent 2, can be studied in 1-m model magnets. The relevant data could be obtained on D-12C-7, for example. Item 3 may not be able to be tested unambiguously in a 1-m model because the relative axial and transverse velocities may allow turn-to-turn propagation at the ends of the magnet to produce a normal region at the center of the turn before the quench propagates across the wedge.

Further work will also be required to give exact results on the turn-to-turn propagation time. Though the data indicate they are about 4 to 7 ms per turn at high fields, this should be confirmed with some more direct measurements. These data could also be obtained on D-12C-7 if it is retested and if some voltage taps are moved.

B.11 Results from Heater-Induced Quenches of a 4.5 m Reference Design D Dipole for the SSC

G. Ganetis and A. Prodell
Brookhaven National Laboratory

February 6, 1986

B.11.1 Experimental Setup and Procedures

Quench studies were performed using a 4.5 m long Reference Design D Dipole, SLN-012, for the SSC. Eight pairs of voltage taps were installed at the locations on the right side of the inner coil of the magnet as shown in Fig. B.11-1. "Spot" heaters to initiate magnet quenches were centrally located between the voltage taps of 4 of these pairs on the mid-plane turn of the inner coil, as indicated in Fig. B.11-1. A redundant array of voltage taps and heaters was also installed on the left side of the inner coil. The temperature rise of the magnet conductor during a quench was determined by measuring the resistance of the conductor cable in the immediate vicinity of the quench, which, in turn, was obtained from observations of the magnet current and voltage. The temperature of the conductor was then determined by comparing its resistance to an R vs. T curve appropriate for the conductor. Longitudinal and azimuthal quench propagation velocities were measured by knowing the distances between pairs of voltage taps and observing the times when a voltage signal would appear at the several pairs of voltage taps. The "spot" heaters used in these studies were similar to those described in SSC Technical Note No. 38.

Prior to beginning the heater-induced quenches, the left voltage tap on turn 3 failed and the voltage taps were reassigned as indicated by (7) and (8). With this rearrangement, since the voltage taps for (7) could not be tightly twisted, the voltage signals from (7) had substantial noise from voltages induced in the loop formed by the leads. After a number of heater-quenches had been induced in the magnet, the voltage taps indicated by (5) failed and taps were reassigned to positions shown in Fig. B.11-1 by (5)* and (8(1))*.

B.11.2 Temperature Rise

To obtain the highest temperature to which the conductor could be raised by a magnet quench, the first heater quenches were made at a constant bath temperature of 4.5 K at different values of magnet current to determine the current, I_m, at which $\int I^2 dt$ was a maximum. The curve for heater 6, H6 on Fig. B.11-1, at 4.5 K is shown in Fig. B.11-2. From this curve, it was determined that $\int I^2 dt$ was a maximum when I_m was about 64% of the

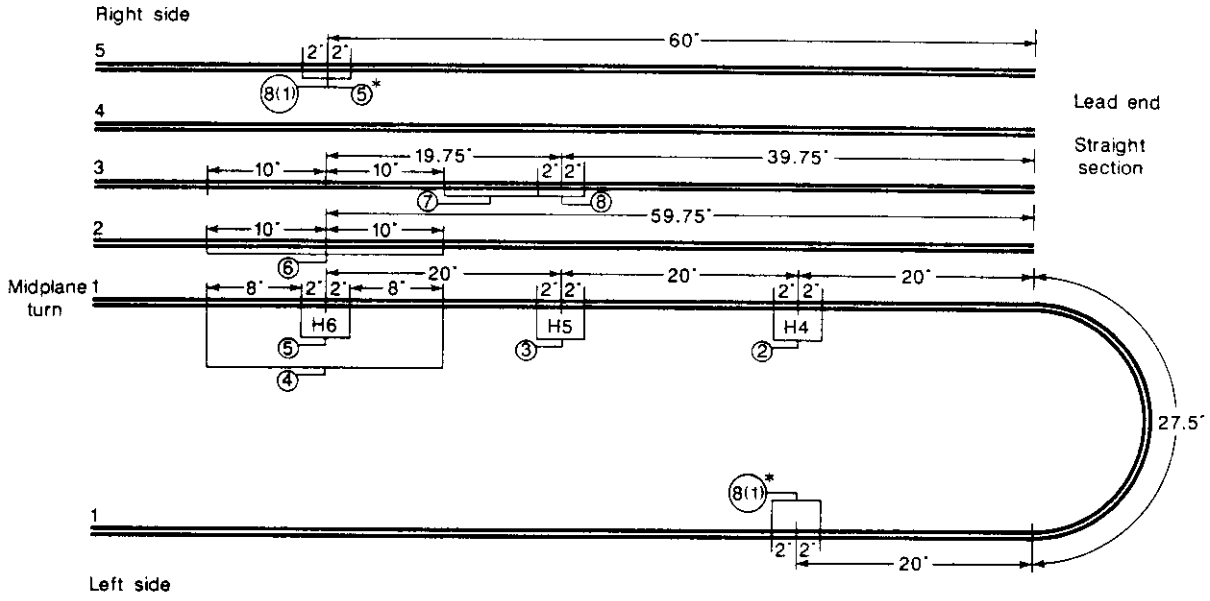

Figure B.11-1. Location of spot heaters and voltage taps on inner magnet coil.

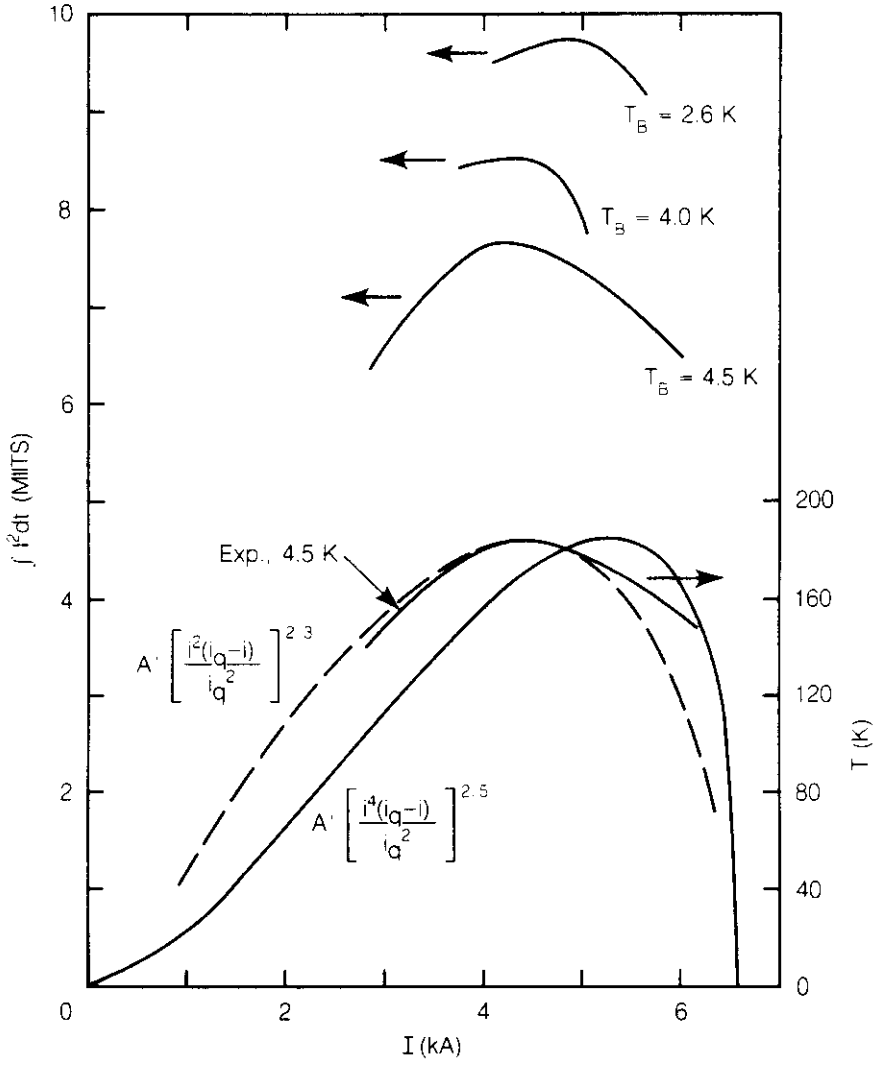

Figure B.11-2. $\int I^2\,dt$ and maximum conductor temperature vs. magnet current.

non-heater induced quench current, I_q, of the magnet. Similar curves, shown in Fig. B.11-2, were obtained at helium bath temperatures of 4.0 K, and 2.6 K to verify that the relationship, $I_m = 0.64\ I_q$, was maintained as the bath temperature was reduced and the quench current, I_q, increased. A plot is also drawn in Fig. B.11-2 of the maximum temperatures to which the section of conductor cable was raised when a quench was initiated by heater 6 as a function of magnet current at a helium bath temperature of 4.5 K. The profile of this plot follows very closely that of the curve of $\int I^2dt$ versus magnet current, indicating again that at the higher magnet currents the quench velocities are increasing rapidly.

The temperature rise of the conductor cable during a heater-induced quench was measured by monitoring the magnet current and voltage across the sections of cable where the heaters were fired and following the procedures described in SSC Technical Note No. 38. The curve in Fig. B.11-3 illustrates the temperature rise of a section of conductor where a heater quench was initiated as a function of $\int I^2dt$. Experimental points obtained from measurements made when heaters 4, 5, and 6 (see Fig. B.11-1) were fired all fell close to the curve shown in the figure. The highest uncorrected conductor temperature achieved at 2.6 K was about 285 K.

B.11.3 Longitudinal and Azimuthal Quench Speeds

Measurements were also made of longitudinal and azimuthal quench velocities by determining the distance between pairs of voltage taps, and by recording the time when a voltage signal would appear at the several pairs of taps after a heater quench had been initiated at a particular location. Observations of the voltage versus time traces for the several pairs of voltage taps also yielded information from which velocities could be measured. An initial change in slope of a voltage trace occurs when a quench begins in or propagates into the region or between two voltage taps, followed by a second change in slope when the quench front propagates to one or both of the voltage taps. The slope after the first change depends on $\Delta\rho$ and Δl in the relationship R = ρl/A as the quench front propagates between the voltage taps of a pair, while that after the second change depends only on $\Delta\rho$,l becoming constant as the quench front propagates beyond the voltage taps of a pair. From these slopes, the "hot spot" correction to R and thus to T was also obtained which amounted to an increase in the conductor temperature of approximately 10 K, making the highest temperature observed in these studies about 295 K.

Figure B.11-4 shows plots of longitudinal quench velocities as a function of magnet current determined between locations (4) and (3), and (3) and (2) on the midplane turn when heater H6 was used to initiate a quench. The curves illustrate how rapidly the longitudinal quench velocity increases with increasing magnet current at the higher current levels. The longitudinal quench velocities along the midplane turn obtained by these measurements do not give clear evidence of an acceleration component. Any indication of such a component, from a limited number of measurements, appears only at magnet currents above about 5.0 kA. At magnet currents below 5.0 kA, the measured velocities in every case but one show a small deceleration component. In addition, three measurements made at 2.6 K at different magnet currents of the velocity from (2) to (8(1))* around the end of the magnet yield velocities less than those from (4) to (3) when heater H6 was fired.

The azimuthal quench velocities between the first and second turns, locations (4) and (6), and the second and fifth turns, locations (6) and (8(1)), obtained when heater H6 was

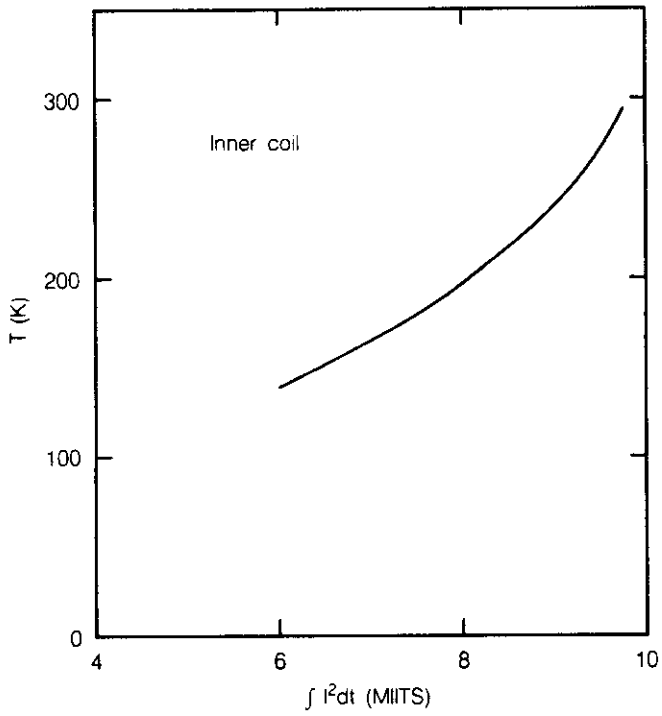

Figure B.11-3. Conductor temperature vs. $\int I^2\,dt$.

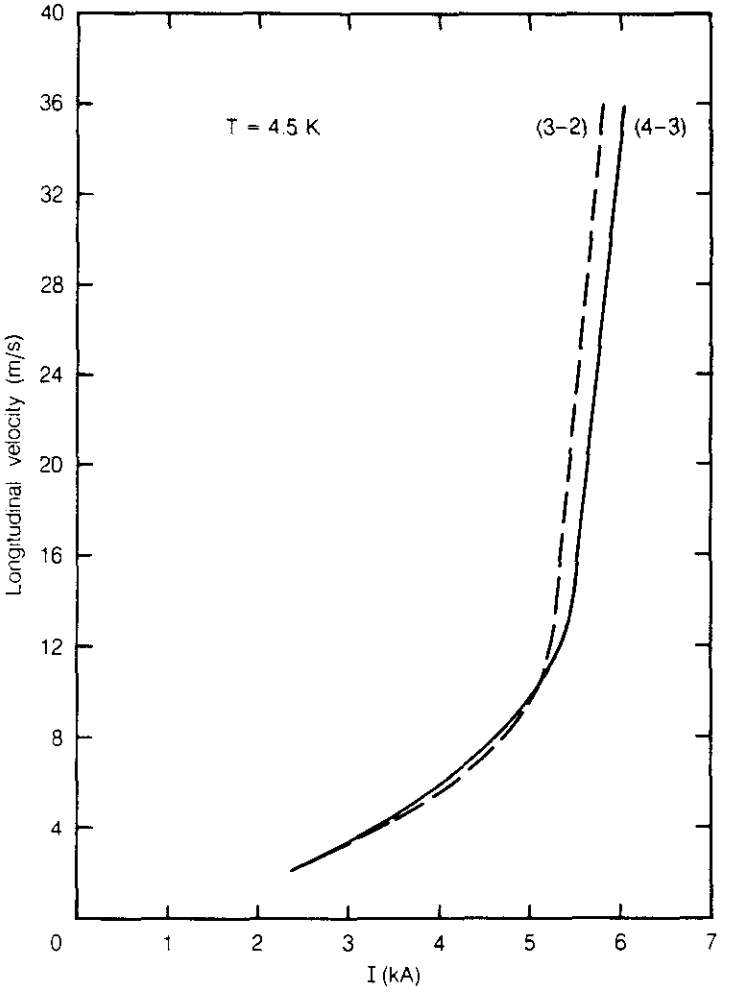

Figure B.11-4. Longitudinal quench velocity vs. magnet current.

used are shown as a function of magnet current in Fig. B.11-5. The azimuthal quench velocities increase rapidly with magnet current and it is this rapid increase, together with that of the longitudinal velocities, which cause both $\int I^2 dt$ and T to peak and then begin to decrease as the magnet current increases, as alluded to above. A comparison of the azimuthal velocities determined from these measurements indicates the presence of an acceleration component which increases rapidly above a magnet current of about 4.0 kA as the magnet current increases.

B.11.4 Effects of Magnet Current

The effect of the dependence of the azimuthal and longitudinal quench velocities on the magnet current can be illustrated by describing the early partial profile of the quench front in several ranges of magnet current. Referring to Fig. B.11-1, using heater H6 to initiate a magnet quench, at magnet currents above 5.0 kA, the quench front reaches location (8(1)) on the fifth turn before it travels longitudinally to location (3). At magnet currents between 4.8 and 4.9 kA, and still using heater H6, the quench front propagates longitudinally to location (3) and next reaches location (8(1)). At magnet currents from 4.5 to 4.7 kA, the quench front propagates first to location (3), then to location (7), and then to (8(1)). From a magnet current of 3.0 kA to 4.3 kA, the quench front reaches locations (3), (7), (8), and (8(1)) in order. At all magnet currents, the quench front propagates longitudinally to location (2) and then (8(1))* after having reached all other indicated positions. Generally, then, at high magnet currents the profile of the quench front shows a peak azimuthally (5 turns) and a relatively narrow base longitudinally. As the magnet current is decreased, the longitudinal base broadens while the azimuthal peak decreases. A more complete profile of the quench fronts could be obtained by a detailed analysis of the data obtained in these studies.

Figure B.11-6 shows the temperature profiles as a function of time at the several locations designated by the number next to each curve, when heater H6 was used to initiate a quench.

Figure B.11-7 shows curves of the magnet current and the quantity $\int I^2 dt$ as a function of time when heater H6 was used to initiate a quench. The time constant of the magnet current decay is about 520 milliseconds. The quench front reaches all locations except (8(1))* before there is any significant decrease in magnet current, and reaches location (8(1))* after the current has decreased by about 15 per cent.

As was mentioned above, at a helium bath temperature of 4.5 K, the quantity $\int I^2 dt$ and the temperature to which the conductor was raised, T, during a quench reached maxima at a magnet current which was about 64% of the non-heater induced quench current, I_q, for the inner coil of the magnet. The usual statement that T is a maximum at $I = 0.8\, I_q$ follows from the dependence of T_{max} on I in the relationship

$$T_m = A' \left\{ \frac{E_m i^4 |i_q - i|}{i_q^2} \right\}^{2/5}$$

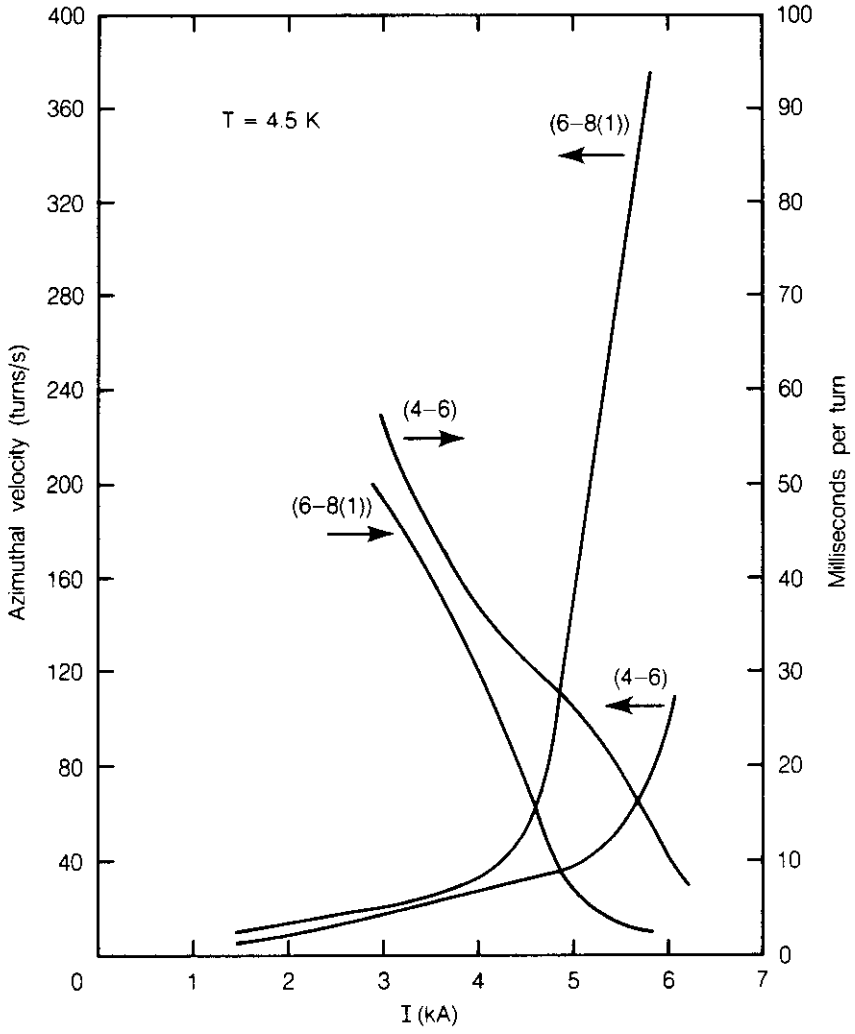

Figure B.11-5. Azimuthal quench velocity vs. magnet current.

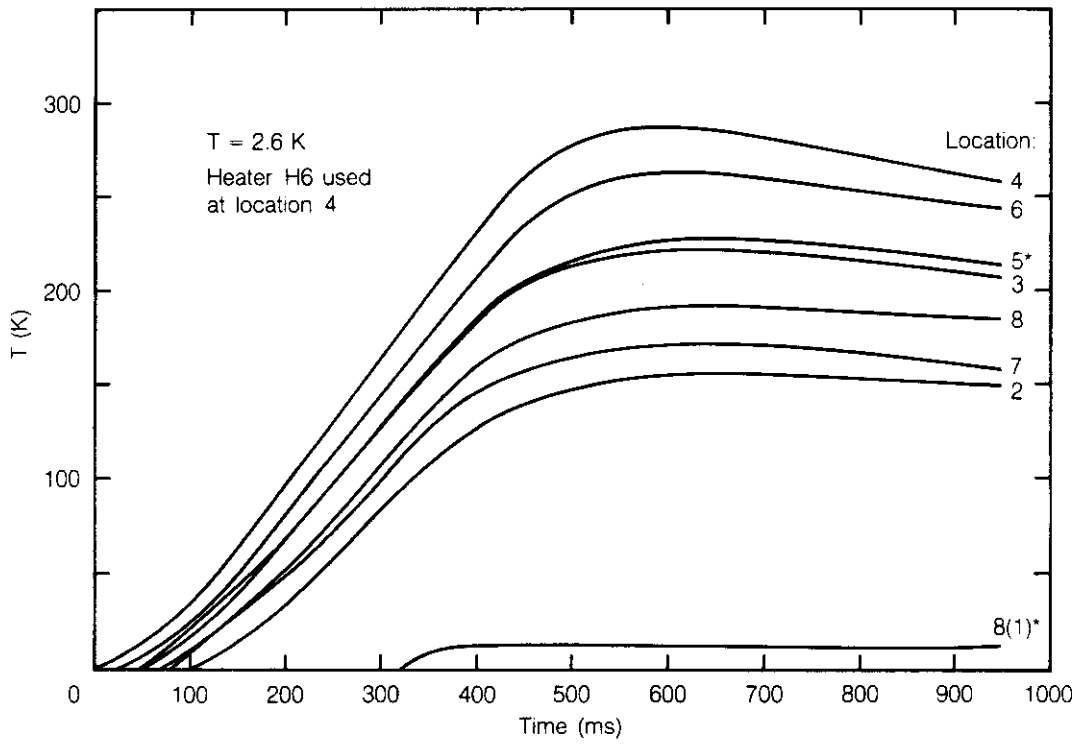

Figure B.11-6. Temperature profile vs. time.

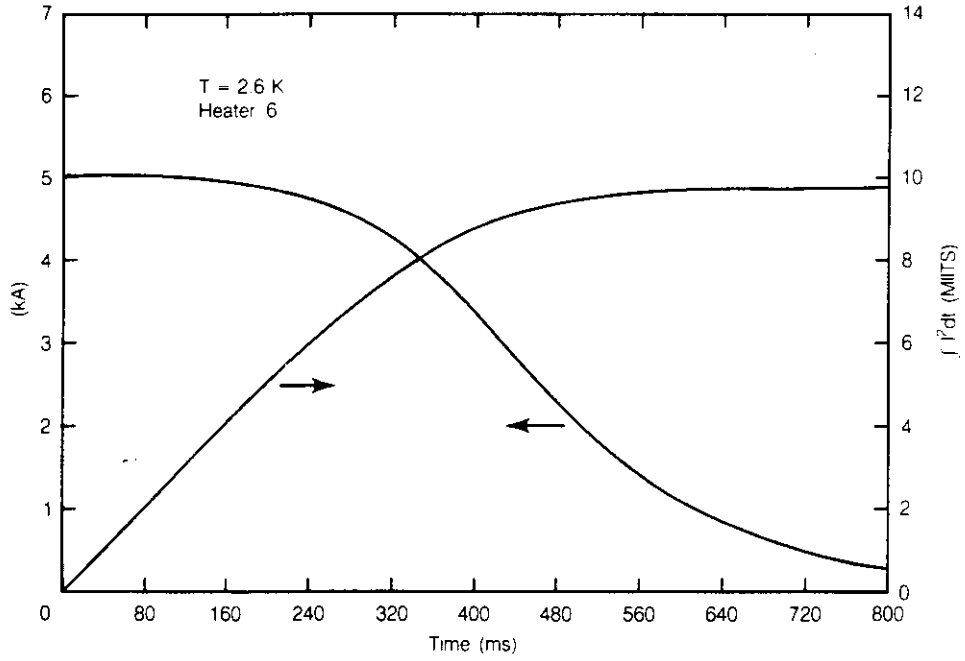

Figure B.11-7. Magnet current and $\int I^2\,dt$ vs. time.

It is interesting to note that a different dependence of temperature on current, for example,

$$T_m = A' \left\{ \frac{E_m i^2 [i_q - i]}{i_q^2} \right\}^{2/3}$$

gives T as a maximum at $I = 0.67\, I_q$, and that a preliminary look shows that this relationship gives reasonable fits to the experimental data.

B.12 Results Using the Active Quench Protection Strip Heaters Installed on SNL008

G. Ganetis and A. Prodell
Brookhaven National Laboratory

January 16, 1986

B.12.1 Procedures

Measurements were made on the SSC Reference Design D dipole magnet SLN008 to study quench behavior of the magnet when active quench protection strip heaters were used to initiate quenches. The strip heaters, their arrangement and installation were essentially as described in Magnet Division Note 107-9 (SSC-MD-822) with the exception that the distances between the heaters on the 12 heater array proposed for the SSC long magnets had been shortened so that 12 heaters per strip were also employed for the 4.5 m long magnet tested.

Only three of the strip heaters and combinations of these heaters were used during the tests. In the first series of tests, the magnet current was set at 4.5 kA, the current at which previous studies had indicated the quantity $\int I^2 dt$ was a maximum. A capacitor bank with a capacitance of 0.0465 farads was charged and them discharged through a strip heater with the charging voltage being increased progressively until a magnet quench was initiated. The time interval between when the voltage was applied to the strip heater and when the magnet quench was initiated was measured as was the time interval between when the voltage was applied to the strip heater and when the voltage across the magnet coil that had quenched reached 3 volts. After the lowest charging voltage at which a quench could be initiated was determined, the "threshold voltage," the voltage was increased in a number of steps until no substantial change in the times being measured was observed.

B.12.2 Results

Figures B.12-1, B.12-2, and B.12-3 show plots of the times measured as a function of the voltage applied to the strip heater when heaters #1, 2, and 3 were fired singly. The quantity $\int I^2 dt$ is also plotted as a function of the applied voltage. It is apparent that the times measured decrease rapidly at first as the voltage is increased from the threshold voltage to values in the range of 250 to 300 volts, beyond which range the rate of decrease is much smaller and approaches a constant value. A similar statement may be made about the $\int I^2 dt$ vs. heater voltage curves.

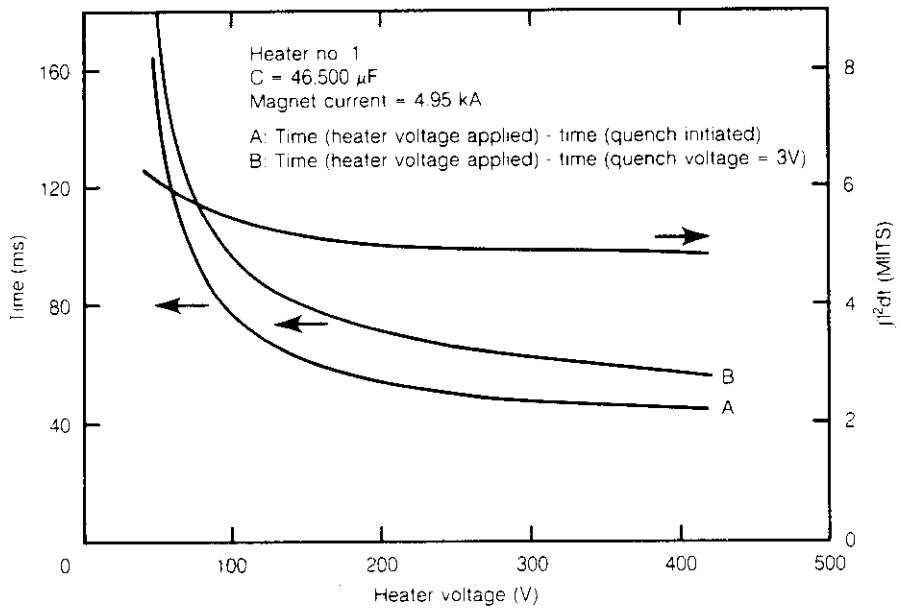

Figure B.12-1. Measured times and $\int I^2\,dt$ values vs. applied heater voltage.

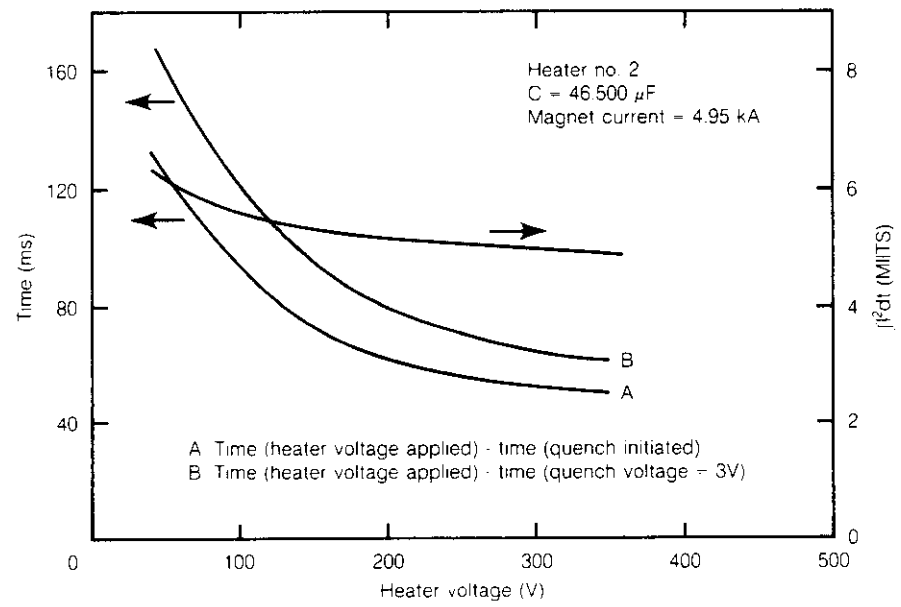

Figure B.12-2. Measured times and $\int I^2\,dt$ values vs. applied heater voltage.

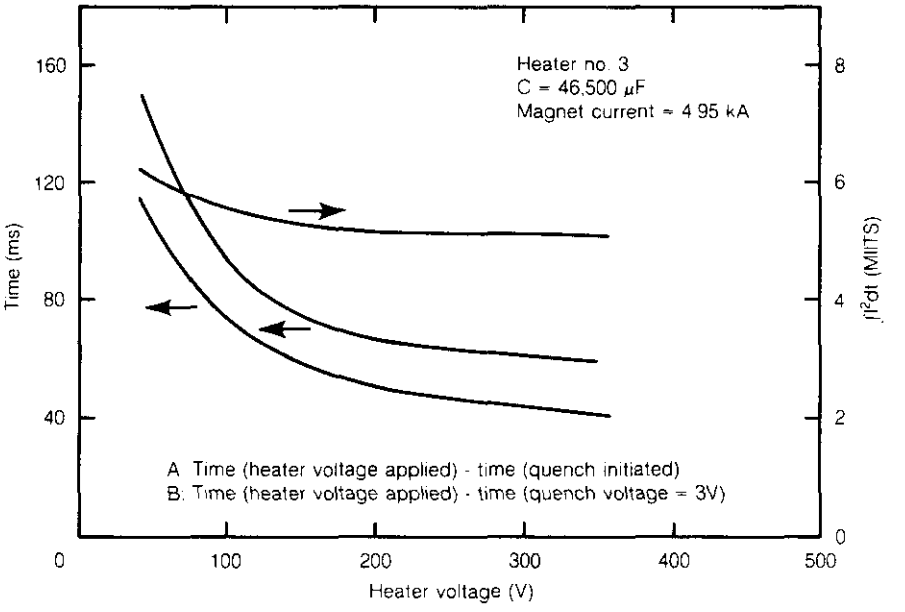

Figure B.12-3. Measured times and $\int I^2\,dt$ values vs. applied heater voltage.

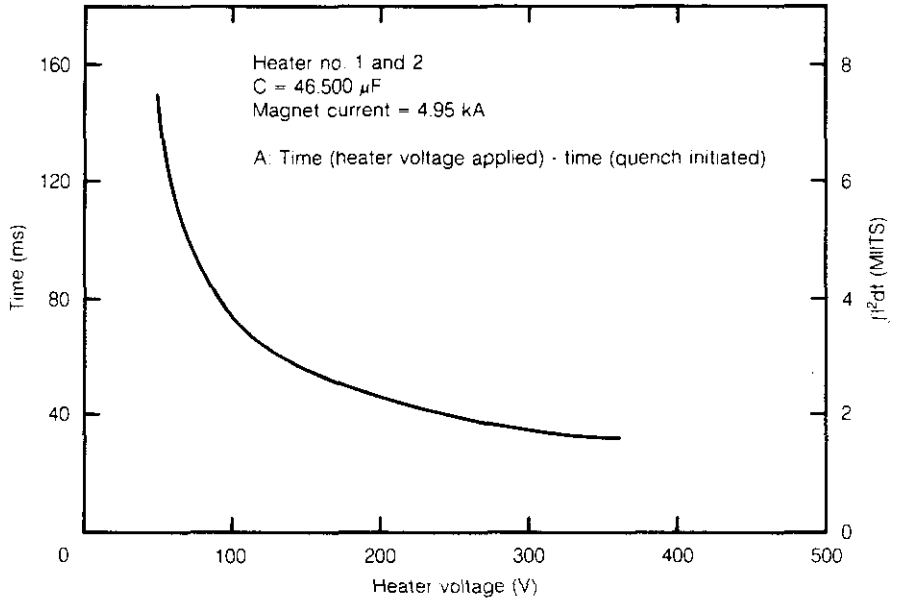

Figure B.12-4. Time from voltage applied to quench initiated.

Curves for the time interval between heater voltage applied and quench initiated are shown in Figs. B.12-4 and B.12-5 for heater combinations (1+2), and (2+3) which were pulsed together in pairs. Since the voltages across the magnet coils which were being quenched were bucking, it was not possible to obtain accurately the times at which 3 volt quench signals developed.

Figure B.12-6 shows the plots for the heater combination (1+3) where the quench voltages were not bucking. Although the curve for the times between heater voltage applied and quench initiated is similar to those for the single strip heaters, the time between quench initiated and a quench voltage of 3 volts were smaller than those for the single heater tests, as expected.

Figure B.12-7 shows the curves for the heater combination (1+2+3) where two voltages were additive and one was bucking.

The curves shown in Fig. B.12-8 are from measurements made by varying the capacitance while setting the charging voltage each time at 275 volts. The magnet current for each of these quenches was 4.95 kA. As can be seen from this figure the times become dependent on the capacitance, and therefore the energy discharged in the heater, only at low values of the capacitance.

Figure B.12-8 and the previous figures indicate that the times to initiate a quench, and to achieve a quench voltage of 3 volts, are strongly dependent on the voltage applied to the strip heater for the lower values of the applied voltage, with this dependence weakening as the value of the voltage is increased. Presumably this dependence is related to the power level applied to or the initial "kick" given to the heater. The heater acts like a fuse, but once a quench has been initiated the heating effects are rapidly dominated by the magnet discharging through the increasingly resistive conductor.

These figures also show that the time interval between the initiating of a quench and the quench voltage reaching 3 volts approaches a constant limiting value as the strip heater voltage is increased, which value probably depends primarily on the quench front velocities, which in turn are dependent on the magnet current. The increase in this time as the strip heater voltage is decreased, probably relates to the initial conditions of temperature and length of the conductor that is first driven normal by the heater.

Figure B.12-9 shows plots of times and $\int I^2 dt$ as a function of magnet current with a capacitance of 0.046 F and 275 volts being used to activate strip heater #1 for each of several magnet currents. The time interval between the heater voltage applied and quench initiated decreases as the magnet current is increased, because the thermal margin of the conductor decreases as the magnet current approaches the "natural" quench current. The interval between the two time curves also decreases with increasing magnet current, an indication that the time between the initiation of a quench and a measured quench voltage of 3 V is dependent on the quench front velocities which are increasing as the magnet current increases..

Curves of magnet current versus time and $\int I^2 dt$ versus time are plotted in Fig. B.12-10 for the three cases where 1, 2, and 3 strip heaters are powered using a capacitance of 0.0465 F and a voltage of 275 volts. As expected, the time constant of the current decay decreases as the number of heaters used increases, indicating that more of the magnet conductor becomes resistive as more heaters are brought into play. The effect of the shorter time constant on $\int I^2 dt$ is noticeable, the use of 3 heaters reducing the value of $\int I^2 dt$ by about 14 per cent below that measured when one heater was used.

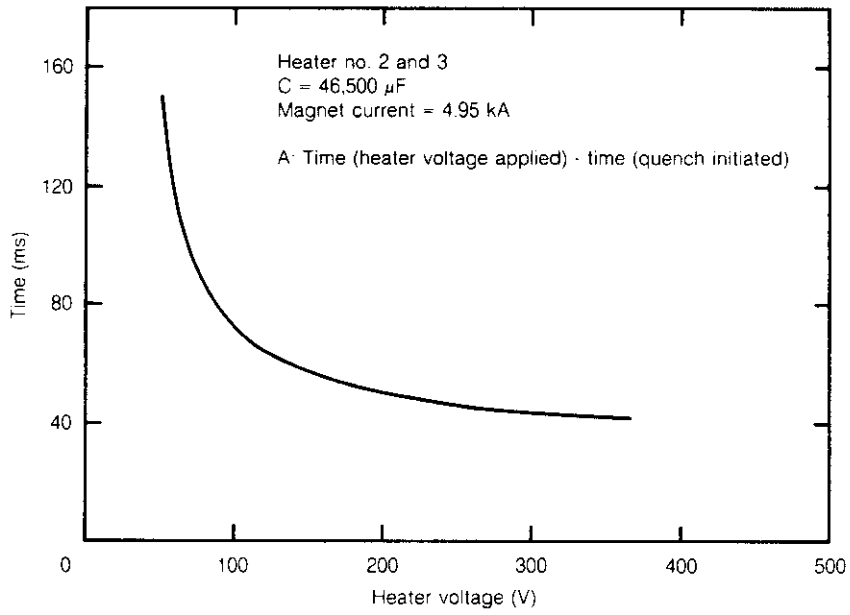

Figure B.12-5. Time from voltage applied to quench initiated.

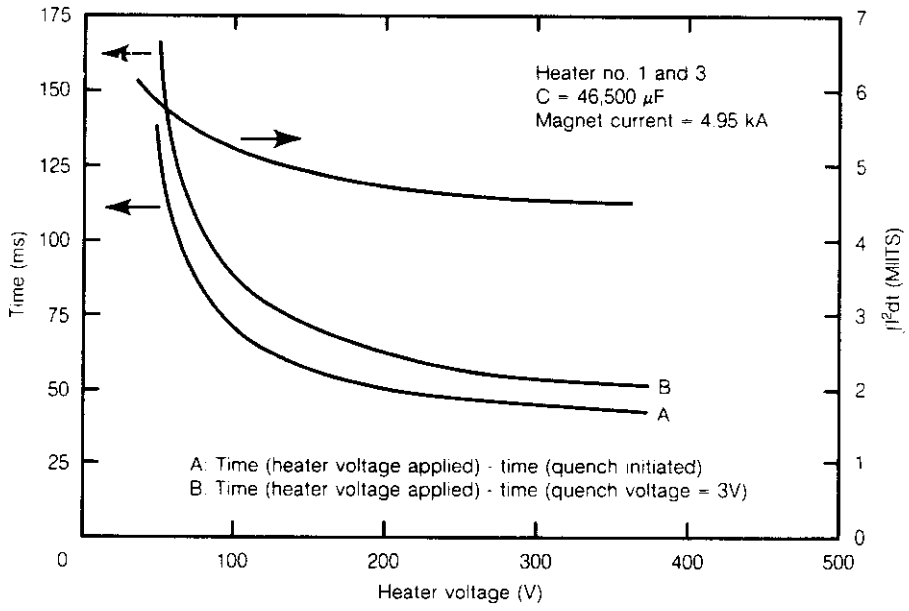

Figure B.12-6. Time from voltage applied to quench initiated, or to 3 V quench voltage.

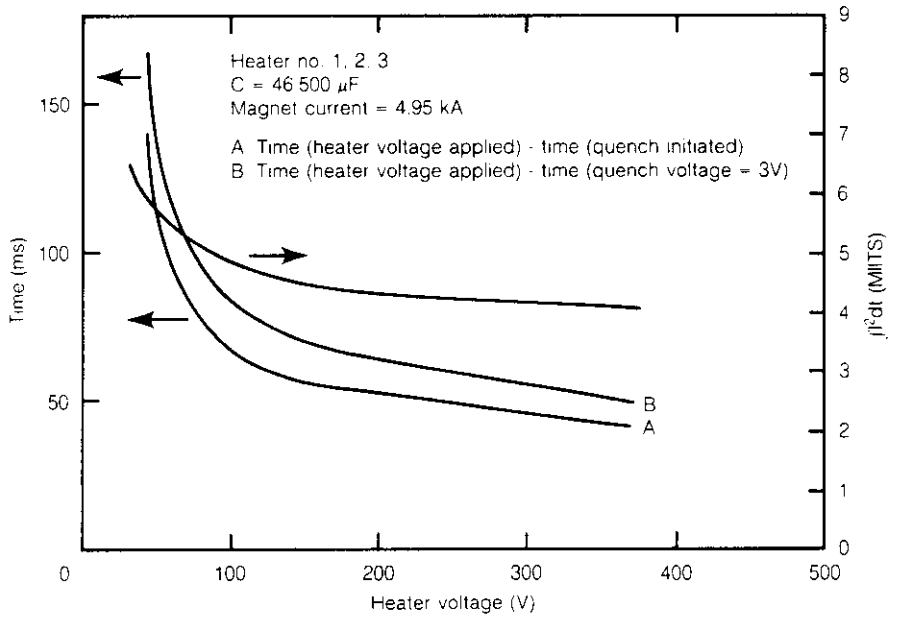

Figure B.12-7. Time from voltage applied to quench initiated, or to 3 V quench voltage.

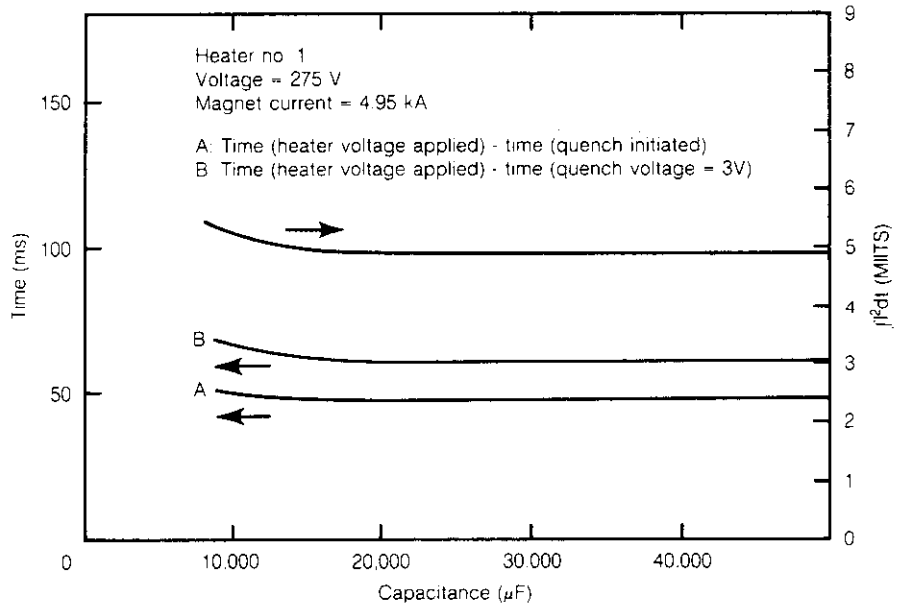

Figure B.12-8. Effects of varying capacitance with constant charging voltage.

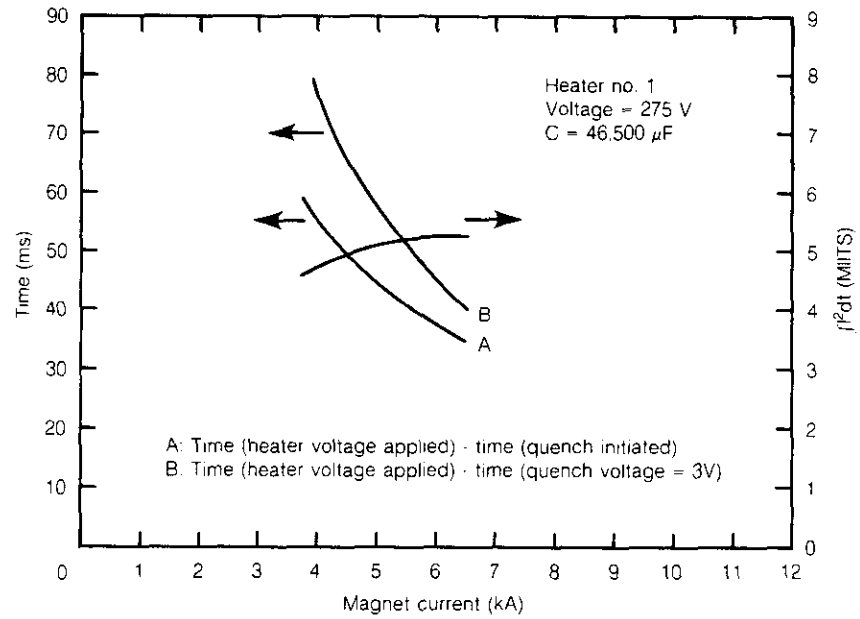

Figure B.12-9. Times and $\int I^2\,dt$ vs. magnet current.

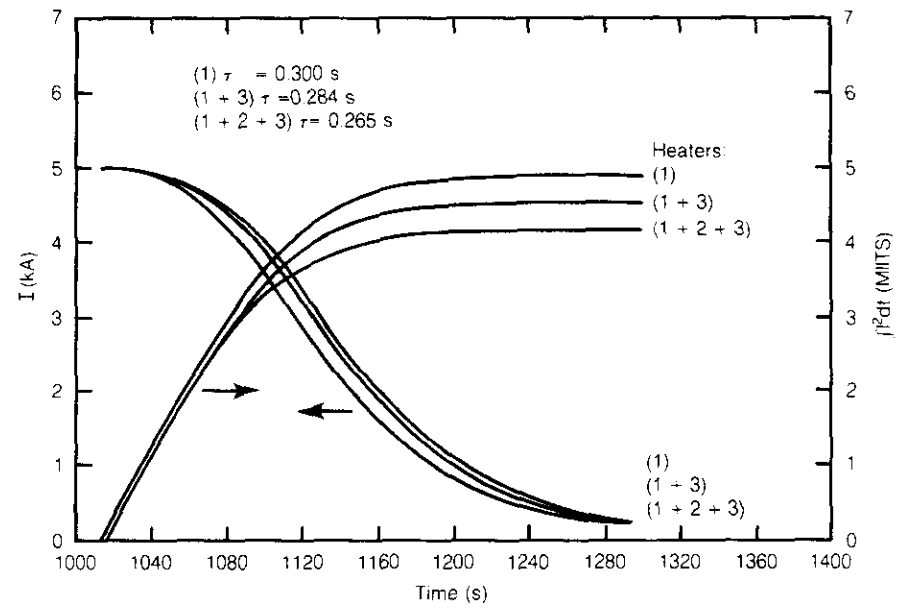

Figure B.12-10. Magnet current and $\int I^2\,dt$ vs. time.

B.13 Cryostat

Fermilab Staff
Fermi National Accelerator Laboratory

March 1986

B.13.1 Introduction

The cryostat must permit proper magnetic functioning of the magnet housed within it, provide low thermal loads to the refrigeration system, operate with high reliability and be capable of being produced on a mass production basis at a low cost. The development of the cryostat design took advantage of the extensive experience gained in the design, construction and operation of the Fermilab Tevatron superconducting magnet system [B.13-1], which includes approximately 1000 superconducting magnet-related devices.

The SSC cryostat differs, however, in two fundamental ways from the cryostat used in the Tevatron magnets. In the Tevatron heat generated in the coil system from ramping (one cycle per minute) accounts for half of the refrigeration load. The SSC, on the other hand, will ramp very slowly and at most a few times a day. The heat load due to ramping will be negligible compared to the static heat load. The operating cost of the SSC will, therefore, decrease by an amount proportional to the static heat load. The design of the SSC cryostat reflects the emphasis on a low heat load. The SSC cryostat is also designed to have much lower resistance to the flow of cryogens than was necessary in the Tevatron. Initial SSC costs can be greatly reduced by having a few widely spaced refrigerators. The SSC cryostat must therefore accommodate large-diameter cryogenic piping of circular cross section.

The development of the cryostat design relied heavily on the previous magnet and refrigeration system design efforts of the SSC program. Included was the work on the iron-less $\cos\theta$ dipole magnet for SSC Reference Design B [B.13-2]. The cryostat effort involved extensive analytical and experimental studies of cryostat components and systems, much of which were generic in nature and thus apply to the design effort for the high field SSC dipole subsequently chosen.

Following the SSC magnet style selection, the cryostat program [B.13-3] focused on the extension and improvement of the Cost Design cryostat, with a major near-term goal being the design, construction and evaluation of several full length (16.6 m magnetic length) magnet models.

B.13.2 Design

Design Requirements

The general cryostat design requirements are given in Table B.13-1. Conditions that control and affect the design include magnet transportation and installation, as well as transient, steady-state and upset operating conditions. Component design issues include fluid flow, material performance, structural integrity, displacement (elastic and creep), thermal performance and thermal contraction. Functional trade-offs were employed to optimize the effectiveness of each component as it relates to the overall, long-term performance of the integrated magnet system.

Table B.13-1
General Cryostat Design Requirements

- Environment compatible with required magnetic performance
- Low thermal loads to the refrigeration system
- Structurally sound relative to shipping and operational loads
- Transportation and installation/removal ease
- Mass producibility
- Low cost

Design Approach

In order to provide a focal point and reference source for the cryostat design effort and to establish and promote the essential and regular communication between accelerator designer, magnet designer/builder and accelerator operator/user, detailed cryostat design criteria [B.13-4] were developed. They resulted from the efforts of physicists, engineers, and magnet builders, and involved the SSC Central Design Group, national laboratories, and industry. The criteria are subject to continuing review, development and expansion. The contents of the cryostat design criteria are listed in Table B.13-2.

Table B.13-2
Cryostat Design Criteria

- Interfaces
- Tunnel installation
- Magnetic function
- Position control
- Structural loads
- Vacuum system
- Cryogenics
- Design life and operating cycles
- Radiation environment
- Storage/installation environment
- Instrumentation
- Repairs
- Design and analysis
- Material properties
- Suspension system
- Failure mode analysis

The design process produced component and system designs by concept development, complemented by analytical studies of performance, safety, etc. The process factored in manufacturability, tooling, quality, cost, etc. The design effort was augmented by an experimental program, which evaluated components such as suspension units, multilayer insulation, etc., and complex assemblies such as the magnet cold mass, full-length functional magnetic models, etc. This program has added greatly to the confidence in the resulting conceptual design.

Cryostat General Arrangement

The general cryostat arrangement is shown in Figs. B.13-1 and B.13-2. The major elements of the cryostat are the cryogenic piping, cold mass assembly, suspension system, thermal shields, insulation, vacuum vessel, and the interconnection region.

B.13-3 Cryostat Components

Cryogenic Piping

The cryostat assembly contains all piping that interconnects the magnet refrigeration system throughout the circumference of the ring. A five pipe system has been selected for cryogenic and magnet safety reasons.

Pipe 1: The complete cold mass helium containment subassembly that contains the supply of single phase helium fluid flowing through the magnet's iron and collared coil assembly.

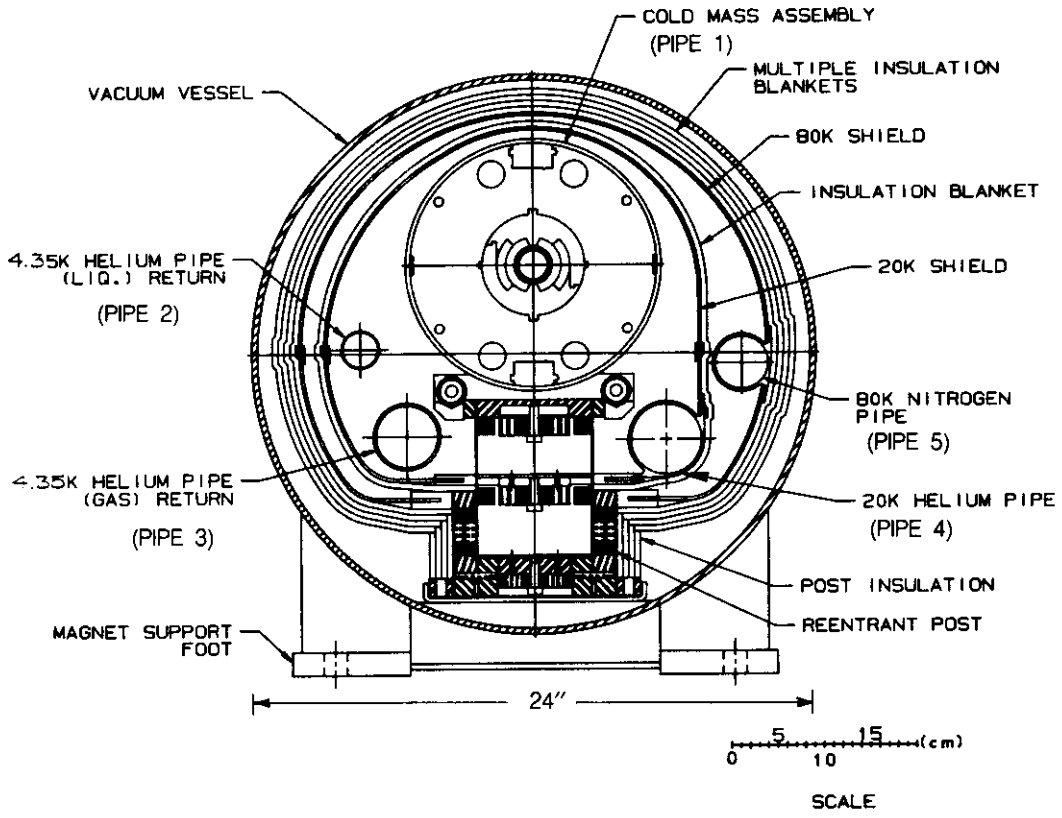

Figure B.13-1. Cross section of dipole cryostat.

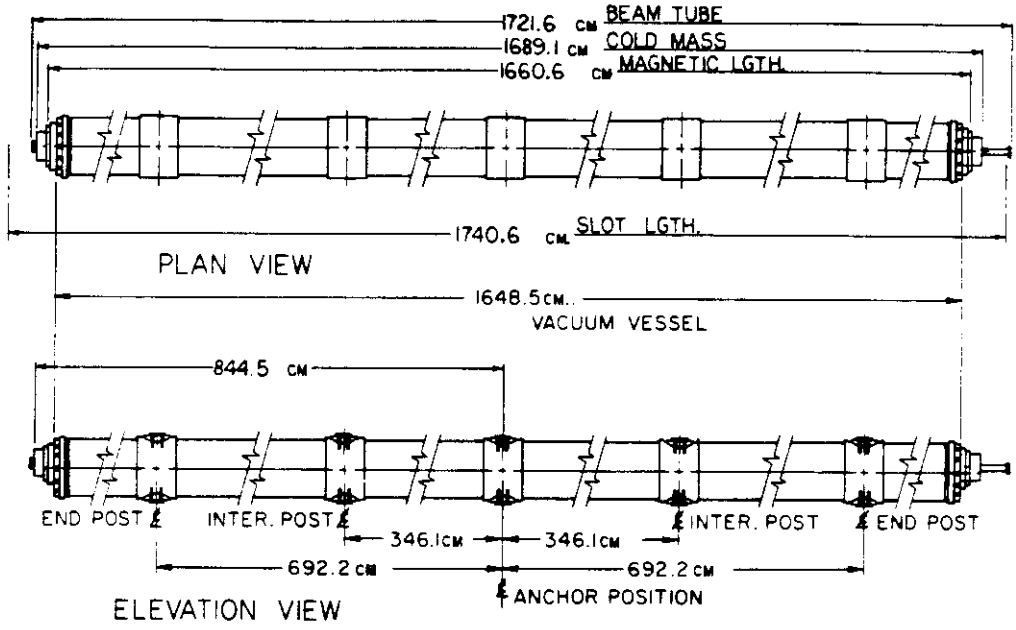

Figure B.13-2. Longitudinal views of cryostat.

Pipe 2: The 4.35 K helium fluid return and recooler supply pipe.

Pipe 3: The 4.35 K helium gas return pipe. The 4.35 K gas is generated in the helium recooler assemblies spaced around the accelerator ring to regulate the temperature of the single phase helium fluid.

Pipe 4: The 20 K thermal shield cooling pipe. This pipe connects to the helium relief header during system cooldown, or to the return or supply headers during operation. The 20 K line provides quench buffering.

Pipe 5: The 80 K thermal shield cooling pipe. This pipe connects to the liquid nitrogen return or supply header.

The pipes are sized for pressure drops that are compatible with the design of the refrigeration system. Circular cross sections are employed for reasons of compatibility with conventional bellows and/or intermetallic transition joints, and to facilitate the use of automatic welding and cutting equipment for the assembly and disassembly of joints. All internal piping is designed for an internal pressure of 20 atm. Piping support design considered the axial loads due to bellows recompression during assembly, pressure differential across the bellows, and axial thermal contraction of the piping. Deflection analysis also included the effects of bellows squirm.

Cold Mass Assembly

The cold mass assembly consists of the beam tube, collared coils, stacked iron yoke laminations, outer helium containment shell and alignment fiducials; all are joined together to provide a leak tight and structurally rigid welded assembly. The cross section of the cold mass assembly is shown in Fig. B.13-3.

Supercritical helium at 4.35 K and 4 atm is passed through the cold mass assembly to remove heat and to maintain the coil temperature at or below this temperature. The static heat load from conduction and radiation is estimated to be 0.02 W/m, and that due to synchrotron radiation is 0.12 W/m. The synchrotron radiation load is seen by the helium between the beam tube and the inner dipole coil. The annular space for this helium flow is small; however, the load is transferred radially by the 1 g/s flow that passes through the region to the main coils and, subsequently, to the main helium flow. Approximately 100 g/s total flow is required to limit the temperature increase to less than 0.2 K between recoolers (spaced every 200 m). This larger flow passes through the four large holes in the yoke laminations.

The helium containment shell is the principal structural element of the cold mass assembly, and provides the necessary rigidity between suspension points. The structural parameters of the cold mass assembly are given in Table B.13-3. The structure initially assumes no stiffening contributions by the collared coil assembly or by the yoke. The increase in stiffness due to these components requires experimental determination. Also requiring evaluation are the dynamic characteristics of the cold mass assembly, including the damping coefficients and the responses to transportation, handling, seismic and operational dynamic inputs.

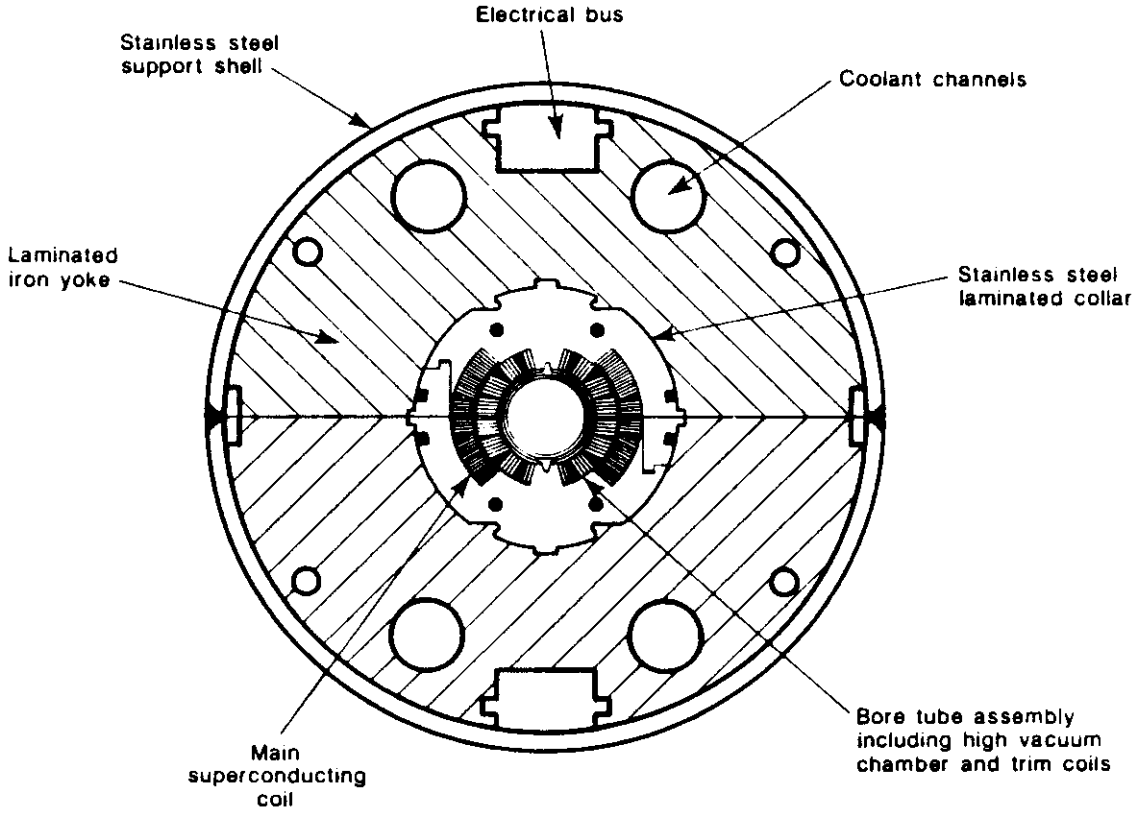

Figure B.13-3. Cross section of dipole magnet assembly (cold mass).

Table B.13-3
Cold Mass Assembly Structural Parameters

Overall	
• Outside diameter of iron yoke	26.67 cm
• Yoke length, overall	16.76 m
• Weight	7250 kg
• Allowable sag between supports	0.5 mm
• Sagitta	3 mm
Containment Shell	
• Material	304 SST
• Thickness	4.7 mm
• Flexural stiffness	7.2×10^6 Nm^2
• Torsional stiffness	4.4×10^6 Nm^2

Suspension System

The cold mass assembly and thermal shields with their distributed static and dynamic loads are supported relative to the vacuum vessel by the suspension system. This system must function under conditions that include cryostat assembly, shipping and installation, magnet cooldown and warmup, and steady-state operation and upset (i.e., magnet quench, cryogenic fluid leakage, loss of insulating vacuum) conditions. The requirements for the suspension system are: low cost, installation and adjustment ease, high reliability, elastic and creep dimensional stability, and low heat leak. The design requirements for the suspension system are given in Table B.13-4.

The cold mass and shield assemblies are supported at five points along their length. The number and location of these points was determined by the analysis of the deflection of the cold mass assembly as a beam, and by the need to minimize the number of support points for reasons of magnet fabrication ease and to ensure a low heat leak. The relation between cold mass deflection and number of support points is shown in Fig. B.13-4.

During the suspension system design a number of suspension options were considered and developed to varying degrees of completeness. The systems considered, along with a summary of their advantages and disadvantages, are shown in Fig. B.13-5 and Table B.13-5 respectively. A detailed discussion of the options considered follows.

Table B.13-4
Suspension System Structural and Thermal Design Requirements

Assembly weights:	
Cold mass assembly	7,144 kg
20 K shield assembly	227 kg
80 K shield assembly	295 kg
Total	7,666 kg
(3380 lb/support for 5 supports)	
Structure dynamic environments:	
Transportation[a,b]	5 g vertical 3 g axial 2 g lateral
Handling[a,c]	5 g vertical 3 g axial 2 g lateral
Seismic[d]	0.3 g level earthquake
Maximum allowable bending stresses during static or seismic conditions	0.5 × material ultimate strength
Allowable heat loads per magnet:	6.7 W to 80 K 0.72 W to 20 K 0.19 W to 4.5 K
Includes supports, anchor, and contingency	

[a]Removable shipping restraints allowed.

[b]The magnet-to-trailer interface will limit the trailer dynamic input to be less than the handling environment.

[c]Inputs are shock in nature.

[d]Utilize "USAEC Regulatory Guide No. 1.60" horizontal and vertical design response spectra scaled to prescribed earthquake level.

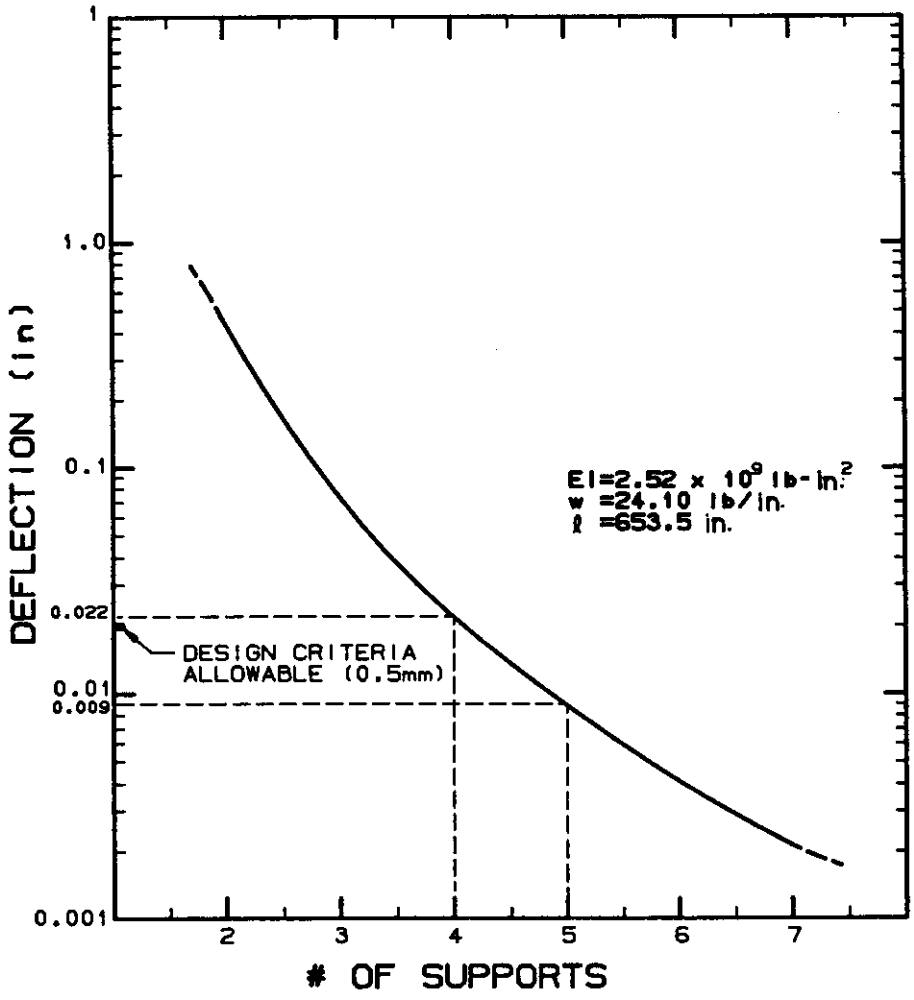

Figure B.13-4. Cold mass deflection vs. number of support points.

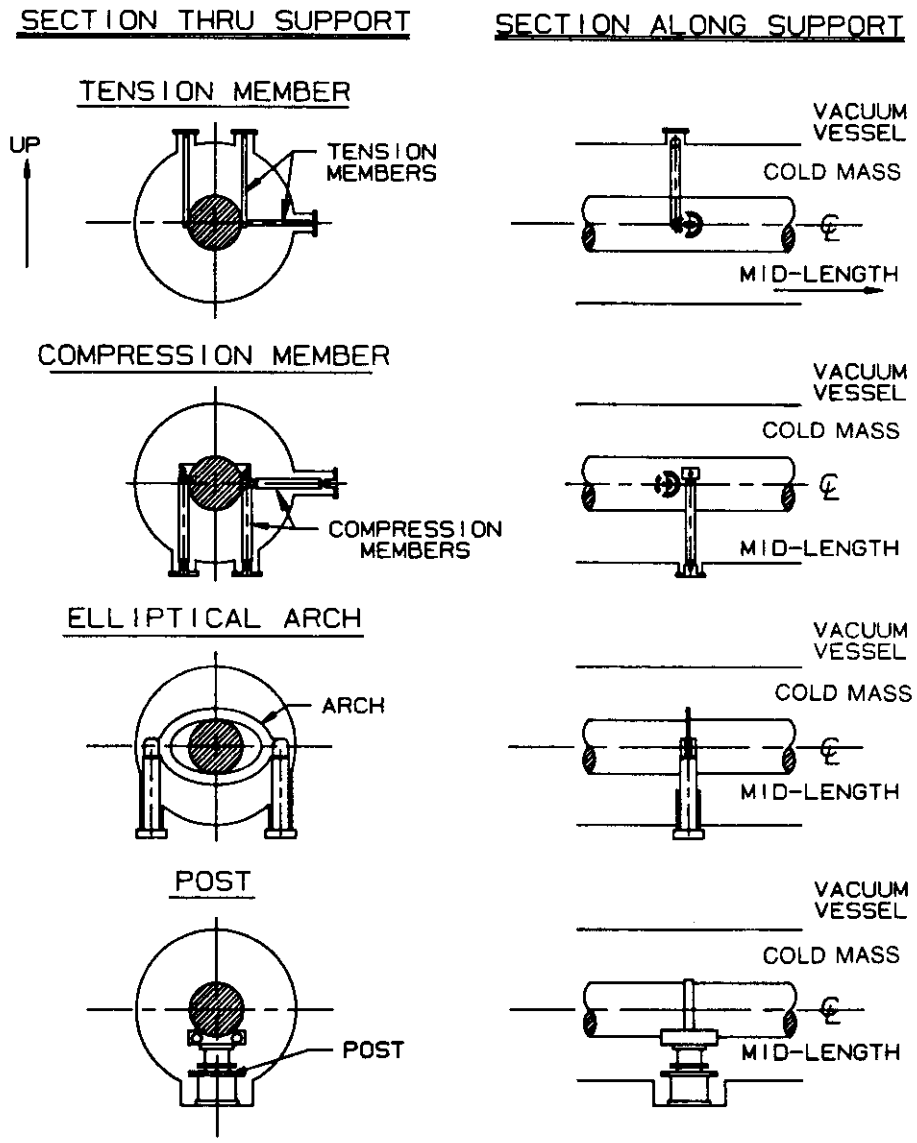

Figure B.13-5. Various support schemes.

Table B.13-5
Suspension Options Comparison

Tension Member	Compression Member	Elliptical Arch	Post-Type
Advantages	*Advantages*	*Advantages*	*Advantages*
1. Low conduction heat leak	1. Low conduction heat leak	1. Insensitive to load direction	1. Minimum number of shield penetrations required
2. Simple construction	2. Simple construction	2. Pivoting and/or sliding may not be necessary	2. Simple accomodation of shields
			3. Simple to heat intercept
			4. No adjustment required after installation
			5. Integral shipping and handling restraint can be incorporated
Disadvantages	*Disadvantages*	*Disadvantages*	*Disadvantages*
1. Difficult to adjust	1. Difficult to adjust	1. High conduction heat leak	1. Moderately high heat leak
2. Difficult to heat intercept	2. Difficult to accommodate shields	2. Complex construction	2. Complex construction
3. Difficult to accommodate shields	3. Large number of shield penetrations required	3. Difficult to accommodate shields	
4. Large number of shield penetrations required	4. Complicates final magnet assembly		
5. Complicates final magnet assembly			

Tension Member

Tension member supports are not new in superconducting magnet designs. They have been used in the CBA project at Brookhaven National Laboratory, and are currently being used for the HERA magnets at DESY. Supporting a structure like an SSC magnet with members in either pure tension or compression represents the most efficient use of support material. The primary benefit of this efficiency is the minimization of overall heat loss by conduction through the support member. Unfortunately, conduction heat loss is only one source of heat load into the helium system. Radiation through cracks and holes in thermal shields and their insulation adds to the conduction contribution. In a magnet system employing five support stations plus a longitudinal anchor, a minimum of seventeen penetrations must be made through each shield and insulating blanket. Not only is it difficult to estimate the radiation loss through a good closure of each penetration, but it is likely to be more difficult to guarantee that each closure can be well made repeatedly in a production environment.

An additional problem with the tension member support system is difficulty of final adjustment. Due to manufacturing tolerances in each member, slight variations in the elasticity of the material, tolerance build-up during assembly and their high flexibility, each tension member must be individually adjusted. This adjustment must be made such that the magnet is located within tolerance as well as ensuring that no one support is loaded more than any other. The difficulty of this adjustment is compounded by the fact that each support must pivot at both the warm and cold ends to allow for axial shrinkage of the cold mass assembly, which means that support loads must not only be distributed uniformly when warm, but must remain so during and after cooldown. Finally, supports of this type do not naturally lend themselves to effective heat sinking and to attachment of intermediate shields. In general, this attachment requires an additional set of hangers for each shield (small cables are commonly used) which further complicates the overall assembly.

Compression Member

In principle, compression member supports are nearly identical to tension supports, and the above discussion may equally well be applied to this support option. One complication associated with compression members but not with tension members is the tendency toward column buckling, which generally necessitates the use of tubular members. Although not a serious design problem, it must be addressed in any such design.

Elliptical Arch Support

One of the more interesting supports considered for use was the elliptical arch. The design considered consists of alternating layers of thin titanium sheet and fiberglass composite forming a laminated beam structure. The titanium sheet acts as the chief structural element resisting bending of the support. The glass composite acts to add stability against local buckling of the titanium. The primary advantage of such a support is that its strength and flexibility lie in directions appropriate for support of superconducting magnets. Although the normal load on any support system is the weight of the cold mass assembly, shipping, handling and seismic inputs can load the assembly in any other direction. The elliptical arch is able to resist vertical and lateral loads equally well. At the same time, its axial flexibility is such that it conceivably could flex along the length of the magnet during cooldown to accommodate the thermal contraction of the cold mass, eliminating the need for pivots or slides. The arch structure, however, does not use material as efficiently as the

tension and compression member supports. This fact, coupled with the high thermal conductivity of titanium (as compared with a glass composite) gives the elliptical arch an unacceptably high heat load.

Post

Like compression supports, a post-type support resists its primary load (cold mass assembly) through compressive loading of the support material. However, rather than using auxiliary members to resist lateral loads, the post support acts in bending if loaded in any non-vertical direction. In general, this bending load drives the diameter of the post up to increase its bending resistance, and subsequently drives up the material cross section. This fact generally results in a calculated heat load that is higher than that of a comparable support of the pure tension or compression type. By "folding" the support inside itself in the form of a reentrant post, one can partially offset the increased cross-section by added length. One benefit of the extra material is a significant increase in the axial stiffness of the post assembly. This increased stiffness, combined with the ability to maintain very close tolerances on the post assembly, eliminates the need for vertical adjustment after installation.

The hollow, central region of the post provides a space for the incorporation of an integral shipping and handling restraint. The restraint, a solid structural member, connects the warm and the cold ends of the post during transportation and handling operations and is removed at the time of installation prior to operation. The restraint, being integral with the post itself, does not require additional penetrations to the vacuum vessel, thermal shields, etc. Since the post represents a single element at each support location, the number of shield and insulation penetrations is reduced from seventeen for the tension or compression supports to seven, including two for an axial anchor, significantly reducing the radiation heat load potential to the cold mass volume. Additionally, the post assembly provides natural attachment points for other components, eliminating the need for cables or other devices to suspend intermediate shields.

To facilitate construction of the large number of magnets required for the SSC, mass production operations must be considered during the design process. One scheme that has great potential for increasing production efficiency is the use of a slide-in magnet assembly. This concept entails fabrication of the entire magnet assembly outside the vacuum vessel. Once completed, this assembly is slid into the vacuum shell and requires a minimum amount of additional work. The post-type support offers the greatest capability of completing the entire assembly prior to installation. The other options generally require a significant amount of additional work, involving attachment of supports after the magnet is installed in the vacuum vessel. Finally, because the post offers such a broad base for support, pivots to accommodate axial shrinkage of the single phase assembly are not required. Rather, a slide mechanism installed at the top of the post allows free axial movement of the cold mass while the post remains stationary.

B.13.4 Details of Support Posts

The details of the reentrant post support are given in Fig. B.13-6. The insulating sections of fiber-reinforced plastic (FRP) are G11CR tubing with metallic interconnections and heat intercepts. The dimensions of the tubular elements are determined by simultaneous consideration of stress, deflection, heat leak, creep effects and installation geometry. The

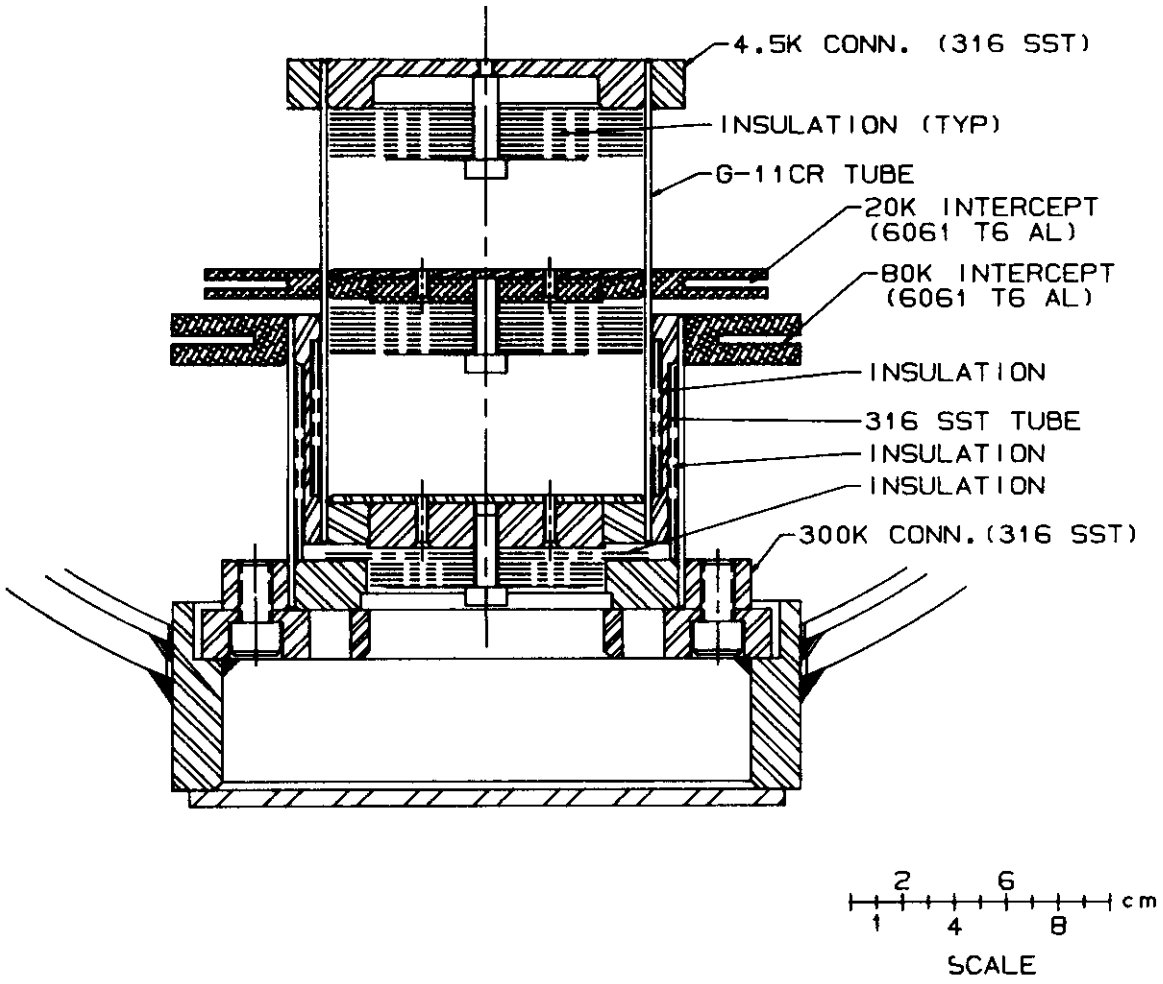

Figure B.13-6. Reentrant support post.

junctions between the FRP tubing and the metallic connections must be able to effectively transmit tension,compression, bending and torsional loads. In order to ensure position stability, the junctions must not slip either axially or tangentially when loaded to design conditions. After consideration of several joining methods, i.e., bonding, screwing, pinning, etc., it was decided to incorporate a shrink-fit type junction. The junction is accomplished by shrinking the tube onto a central metallic disc or ring and then shrinking a metallic ring over the tube. The advantages of the shrink fit junction are as follow:

(a) Non-invasive — The tubing is not machined or penetrated, only clamped between the metallic elements.
(b) Controlled strength — The strength of the junction can be controlled by material selection, amount of interference employed, and surface treatments of the mating surfaces.
(c) Operating temperature range — By proper selection of materials, e.g., stainless steel for the inner disc and aluminum for the outer ring, the junction can become stronger as it become colder due to the added clamping from the differential thermal contraction of the members.
(d) Heat intercept — The junction provides a tightly clamped, reliable connection between the tubing and metallic heat intercepts.
(e) Manufacturability — The junction involves the assembly of machined components with routine procedures.

In order to predict the long term stability, and thus reliability, of shrink-fit junctions, creep tests of the junctions have been made. Creep was measured at 40.5 C, which corresponds to the maximum predicted magnet storage temperature. The measurements incorporated strain gages to monitor the axial extension of the FRP tube material and the change in diameter of the metal clamping ring. The creep has been extrapolated to the 20 year machine life with no significant loss in joint integrity anticipated.

By its nature, a post support is subject to internal axial and radial thermal radiation. The radiation can significantly affect the thermal performance of the support member and must be controlled. Effective control can be achieved by the use of multilayer insulation internal to the post structure. The use of such insulation is shown in Fig. B.13-6.

Proper design of the thermal connection between the 20 K and 80 K intercepts on the support posts and the thermal shields is essential to minimize heat leak. Round, braided copper welding cable with aluminum compression terminals was selected for both intercepts. The cable assemblies accommodate the axial contraction at the end posts due to shield cooldown (at most 2.9 cm). The details of a typical connection to a heat intercept ring of a support post are shown in Fig. B.13-7. A 5 K temperature rise at the 80 K intercept, and a 1 K temperature rise at the 20 K intercept, were selected. The heat leak increases due to these temperature rises are a 10% increase to 20 K, and a 8% increase to 4.5 K.

The support post is fixed at its 300 K end and incorporates a slide at the 4.5 K end to accommodate the axial differential contraction between the mid span anchored cold mass assembly and the vacuum vessel. The 4.5 K slide is a part of the cradle assembly that connects the top of the post to the cold mass assembly. The slide incorporates rods that slide in guide bushing assemblies. The bushings are treated with a lubricant to prevent seizure at low temperatures and in a vacuum environment.

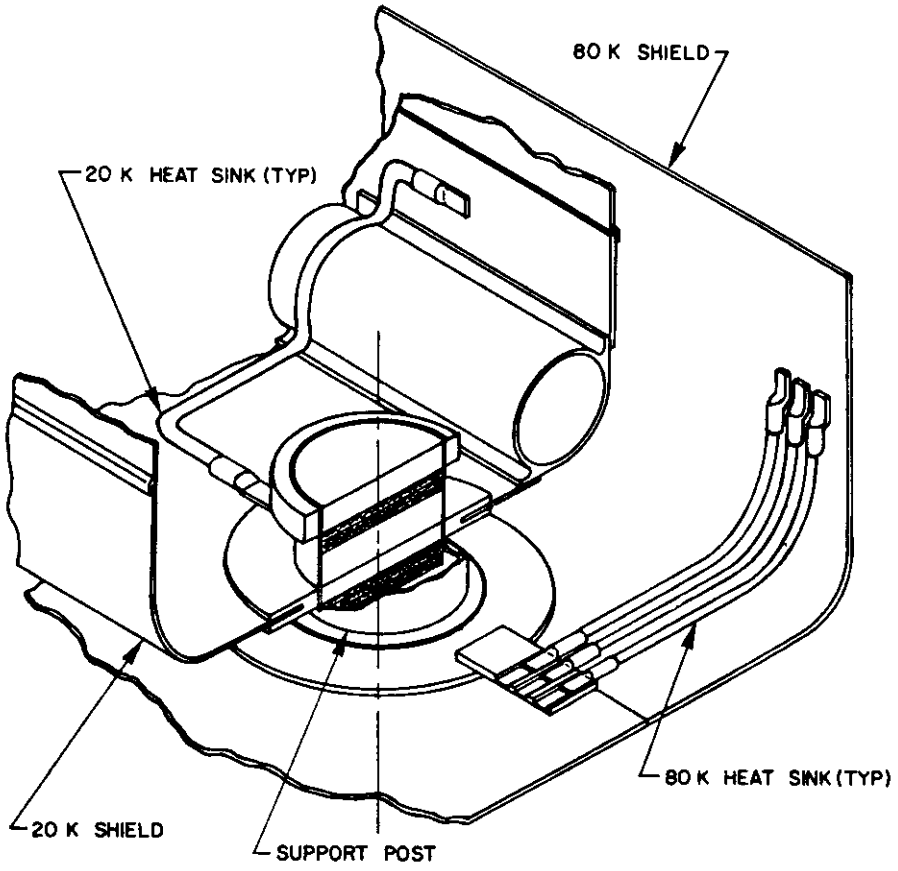

Figure B.13-7. Typical connection to heat intercept ring.

Significant transient bowing of the cold mass assembly is not expected due to its structure, location of helium flow paths, and the cooldown and warmup procedures to be employed. The 20 K and 80 K shields will undergo transient bowing and the shield-post interfaces are designed to provide the relative motions while providing support.

Post type supports were employed successfully in the ironless cosθ magnet development program. Single tube, pivoted post assemblies were incorporated in the 6 m Magnetic Effects Model [B.13-6] (3 posts) and the 12 m Heat Leak Model [B.13-7] (5 posts). The posts performed to design, both structurally and thermally, with excellent agreement between predicted and observed performance. The pivoting feature to accommodate the differential thermal contraction functioned well but required careful adjustment at the time of assembly. A slide assembly was selected for the subsequent design in order to reduce component and assembly complexity.

A reentrant tube post support, instrumented with temperature sensors, was installed and evaluated in a specially configured heat leak measurement dewar [B.13-8]. The support ends were at 300 and 4.5 K with intercepts at 80 K and 20 K. The heat intercepting approximated "ideal" conditions since it provided thermal contact between the intercept rings and the heat sinks around the entire perimeter of the rings. The heat flow to 4.5 K was measured with a heat leak meter [B.13-9]. The heat leak and temperature distribution results are shown in Fig. B.13-8. The measured and predicted temperature profiles and the heat leak to the cold end were in good agreement. The measured heat leak of 27 mW demonstrated that small heat leaks to 4.5 K can be achieved with conventional materials and methods. The thermal connection provided by the shrink fit connections is very good, as evidenced by the close correlation of the measured temperature of the intercept ring and FRP tube section directly above the intercept.

In order to permit the post support to withstand the high lateral handling loads without incurring a severe operating heat leak penalty, the post design incorporates an integral, coaxial, removable shipping restraint. The details of the restraint are shown in Fig. B.13-9. The restraint is installed during magnet assembly and is removed when the magnet arrives at tunnel level. The support post design incorporates removable thermal barrier discs and multilayer insulation blankets that permit the re-deployment of axial thermal radiation heat transfer barriers at the 80 and 20 K heat intercept levels after removal of the restraint.

In order to permit symmetrical axial thermal contraction from both ends of the magnet, the cold mass assembly, piping and thermal shields are anchored to the vacuum vessel at mid-span. The anchor consists of a pair of FRP struts that connect the base of the mid-span support post to the helium containment shell of the cold mass assembly. The anchor struts employ shrink fit joints and axial thermal radiation insulation, as in the support posts. The anchor is sized to withstand seismic axial acceleration. The details of the mid-span anchor are shown in Fig. B.13-10, and the anchor performance parameters are given in Table B.13-6.

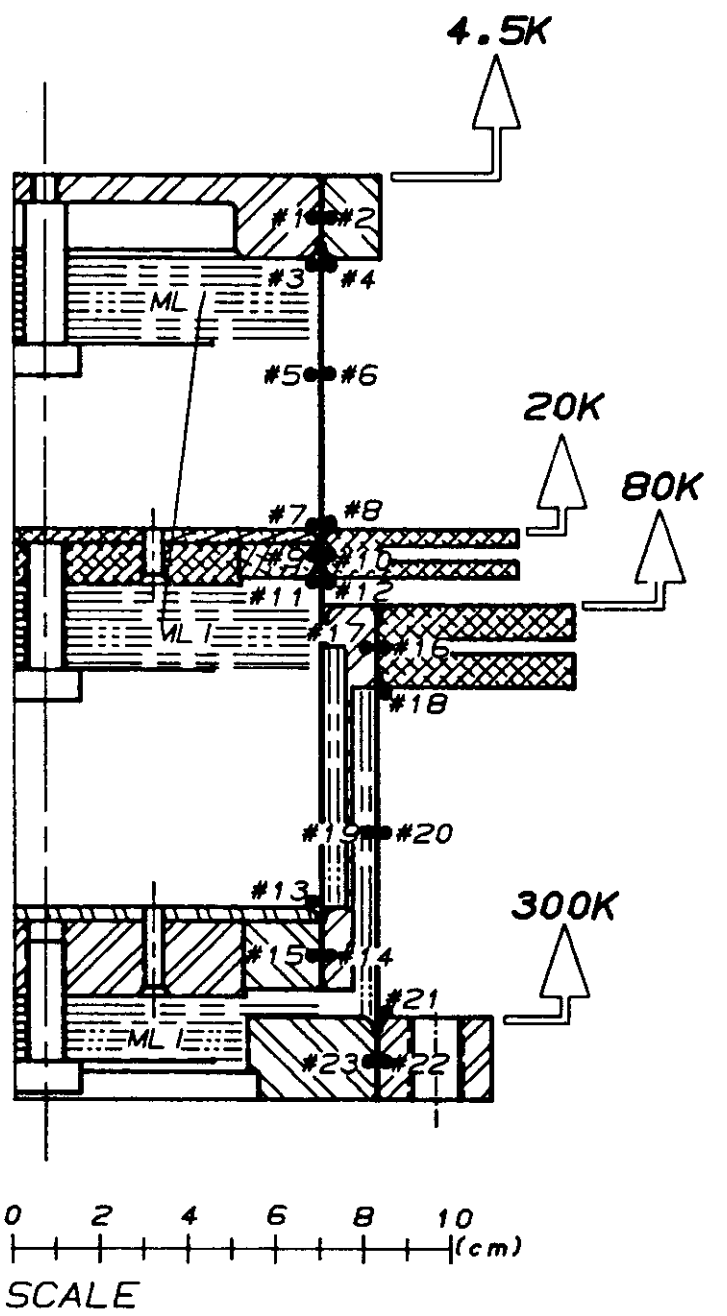

Temperature Profile		
SENSOR	DESIGN (K)	MEASURED (K)
1	4.5	6.5
2	4.5	6.7
3	4.9	7.4
4	4.9	7.9
5	13.6	13.9
6	13.6	14.5
7	20.0	14.7
8	20.0	22.5
9	20.0	19.8
10	20.0	19.6
11	20.0	23.5
12	20.0	25.4
13	79.0	80.3
14	79.1	82.1
15	79.1	82.0
16	80.0	79.6
17	80.0	—
18	80.0	90.7
19	200.0	185.9
20	200.0	186.6
21	200.0	293.8
22	300.0	298.9
23	300.0	299.0

Heat Leak		
QT	DESIGN (mw)	MEASURED (mw)
4.5K	19.1	26.6
20K	103.5	102.0
80K	1136	990.0

Figure B.13-8. Predicted and measured heat leaks and temperature profile.

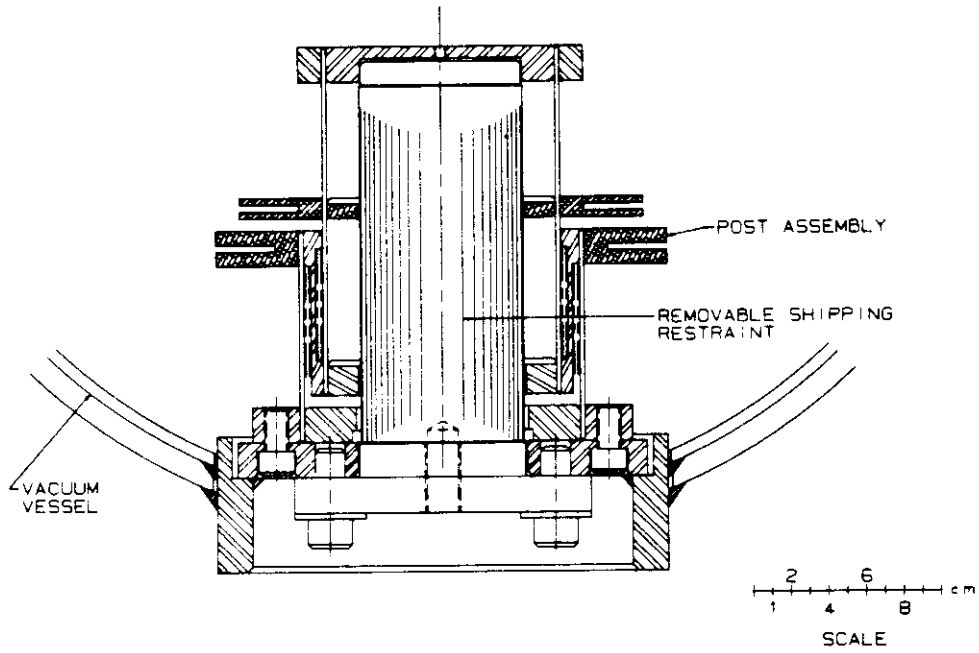

Figure B.13-9. Reentrant support post with shipping restraint.

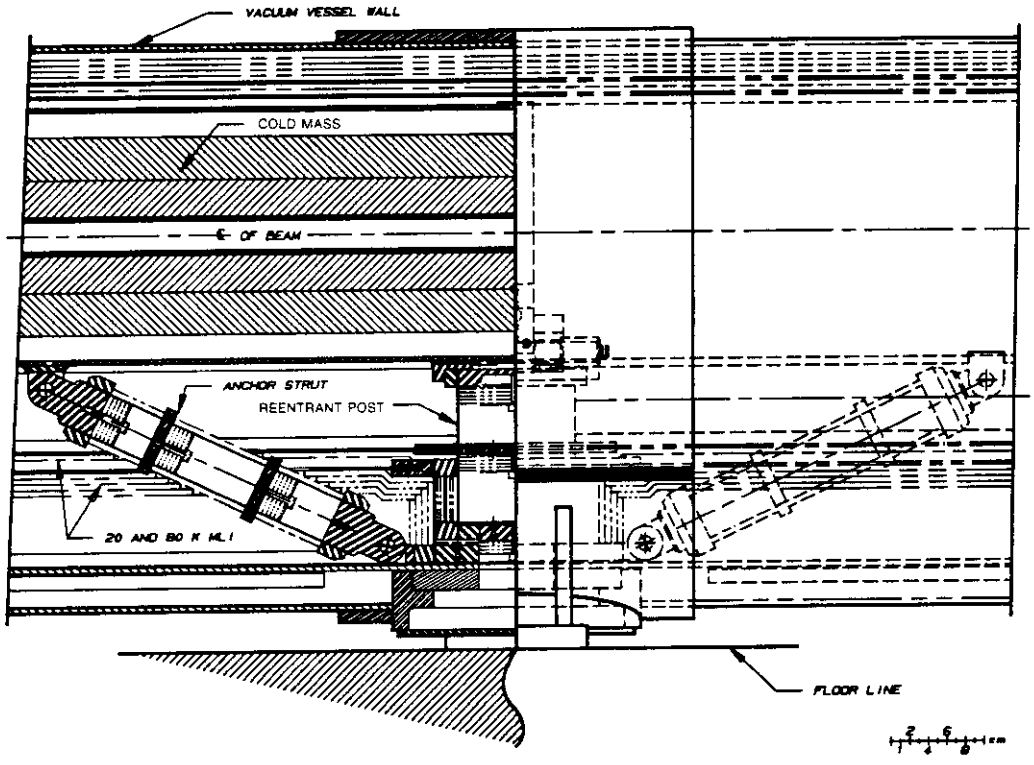

Figure B.13-10. Details of mid-span anchor system.

Table B.13-6
Single Phase Anchor Design Parameter Summary

Design axial load	10000 lb
Anchor tube material	G-11 CR
Length	13.125 in.
O.D.	2.000 in.
Wall thickness	0.055 in.
Design load tube stress	16850 psi
Safety factor	2.4
Column buckling critical stress	64000 psi
Safety factor	3.8
Heat load (both struts) to 80 K	0.78 W
20 K	0.05 W
4.5 K	0.01 W

In order to allow the mid-span anchor to survive high axial transportation and handling loads without incurring a severe heat leak penalty, the cryostat design incorporates a removable axial shipping restraint. It provides a strong structural axial connection between the cold mass assembly and the vacuum vessel shell. The details of the restraint are shown in Fig. B.13-11. The restraint is installed at the time of magnet assembly and is removed when the magnet arrives at its specified location in the tunnel. The restraint also provides a semi-gas tight closure at the magnet ends to accommodate a controlled atmosphere environment during magnet storage and transport.

B.13.5 Thermal Shields

Two thermal shields, operating independently at 20 and 80 K, surround the cold mass assembly. They absorb the radiant heat flux from warmer regions of the cryostat, and provide heat sink stations for the suspension system. The shields are constructed from aluminum and are fabricated from a combination of extruded flow channels and rolled shapes. Aluminum has desirable thermal properties lending itself to normal manufacturing operations such as extruding, machining, and welding with low cost. Aluminum does not exhibit a brittle low temperature transition, and remains strong and ductile at cryogenic temperatures. The low temperature strength is particularly important for the shields, which must sustain the loads due to differential thermal motions associated with system cooldown and warmup.

The 4.35 K liquid and gaseous helium return pipes are supported by hangers from the cold mass assembly. The 20 and 80 K shields are supported by, and are thermally anchored to, the cold mass assembly suspension. The 80 K shield can be reconfigured to

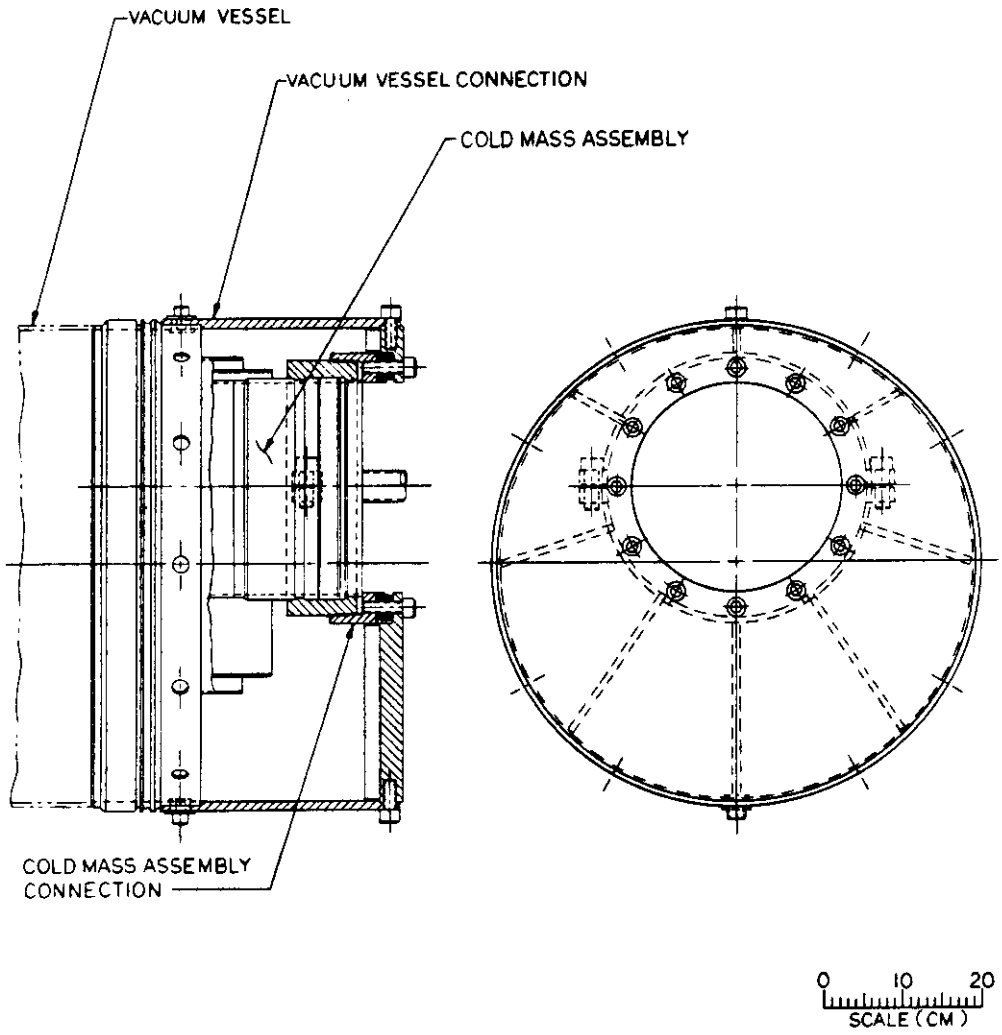

Figure B.13-11. Cryostat shipping restraint.

provide a symmetrical supplemental flow section to serve as the nitrogen return for a single ring, i.e., $\bar{p}p$, collider. The shields are supported at five points and have an axial anchor at mid-span. Elongated cutouts in the shield mounts provide for relative thermal motion between the shields and supports. The design allows all shields and cooling channels to contract to their operating lengths, while other parts remain at ambient temperature. During operation, it is planned to cool down the cold mass assembly and 80 K shield and then the 20 K shield.

A program to study thermal bowing [B.13-10] was undertaken as part of the ironless $\cos\theta$ magnet development program. The inner thermal radiation shield was selected for study. The thermal and structural response of the shield, when subjected to a 100 K temperature differential, was analyzed by finite element methods. Good agreement was achieved between the predicted and measured performance. The refrigeration system design limits the transient thermal excursions of the shield to 100 K.

During steady state operation, the temperature difference across the shield is 1 K.

Insulation

Thermal insulation is installed between the 300 and 80 K surfaces and between the 80 and 20 K surfaces to reduce radiant heat transfer. The design requirements for the insulation are as follows:

(a) Radiation Heat Transfer

T [K]	Q [watts]
4.5	0.05
20	1.72
80	17.2

(b) Best possible performance in the event of increased insulating vacuum pressure. Typically, the system should maintain good insulation performance at pressures up to 10^{-2} Torr. This requirement comes from operating experience of the Tevatron, where there has been considerable difficulty with the insulating system at the higher vacuum pressures associated with magnet quenches.
(c) Utilize the most cost effective materials available.
(d) Materials should be easy to obtain, install and fabricate.
(e) Maintain near maximum thermal performance when subjected to slight compressive loading from adjacent cryostat parts.

The insulation system must have a mean apparent thermal conductivity of 0.83×10^{-6} $Wcm^{-1}K^{-1}$ in order to meet the heat leak design allowance. This can only be achieved using a multilayer, laminar insulation system. The selected system consists of flat, reflective aluminized 0.025 mm polyester film radiation shields with 0.25 mm randomly oriented fiberglass mat spacers. The system provides 18 reflective layers per cm and is prefabricated in blankets of eleven layers. Four blankets are installed on the 80 K surface and

one is installed on the 20 K surface. Prefabricated transition pieces and well defined installation procedures are necessary to eliminate insulation system voids that could significantly increase heat transfer. The polyester substrate and the fiberglass mat should not suffer performance degradations when subjected to the estimated radiation environment of 1×10^8 rad for the 20 year machine lifetime. It is assumed that the radiation environment will be controlled by careful accelerator operating procedures, i.e., by slow filling, etc. The cryostat design insulating vacuum is 10^{-6} Torr with the cold mass assembly and shield at operating temperature. The insulating vacuum will not have a permanent pumping system. Rather, a vacuum pumpout space equal to the thickness of each insulation blanket is provided around one boundary of each insulated assembly.

The insulation system has been successfully employed in two, full section model cryostats, i.e., 6 m Magnetic Effects Model and 12 m Heat Leak Model, of the ironless, $\cos\theta$ magnet development program. The radiation heat transfer factors employed for the design were 6.1×10^{-1} Wm^{-2} to 80 K, 7.5×10^{-2} Wm^{-2} to 20 K and 2.7×10^{-4} to 4.5 K. The insulation system was easily manufactured and performed well during heat leak measurements at good (10^{-6} Torr) and poor (10^{-2} Torr) vacuums. The system was also evaluated from 300 to 80 K in a special test dewar, and yielded a mean apparent thermal conductivity of 6×10^{-7} Wcm^{-1} K^{-1}, which corresponds to a radiation heat transfer factor of 5.8×10^{-1} Wm^{-2} for a four-blanket assembly. The results of the pressure dependence measurements are given in Fig. B.13-12.

B.13.6 Vacuum Vessel

The vacuum vessel defines the insulating vacuum space and provides the support connection for magnet installation in the tunnel; it will be fabricated as a single-piece subassembly. The final magnet assembly incorporates a slide-in insertion of a completed cold mass assembly into the vacuum vessel. The support post-vacuum vessel connection provides for the alignment of the cold mass assembly fiducial system with respect to the vacuum vessel fiducial system. There is no capability for adjustment of the cold mass assembly position relative to the vacuum vessel after magnet fabrication.

Since the vessel has no magnetic requirements, candidate materials were carbon steel, stainless steel, 9% nickel steel, and aluminum. Carbon steel was selected on the basis of cost. The composition of the steel will be a compromise between the material's mechanical properties and fabrication cost. Steel of type AISI 1008 was selected.

Preliminary results of the cryostat failure mode analysis indicate that for the conditions of cryogen leakage from the cold mass assembly into the vacuum space, the steel vacuum shell can be cooled to temperatures where brittle fracture can occur. Such fracture could result in cracks that could require repair.

B.13.7 Interconnections

Mechanical and electrical interconnections are required at the magnet ends. It is essential that the connections be straightforward to assemble and disassemble, compact, reliable and economical.

The dipole-to-dipole mechanical connections involve the following components:

Beam tube vacuum vessel

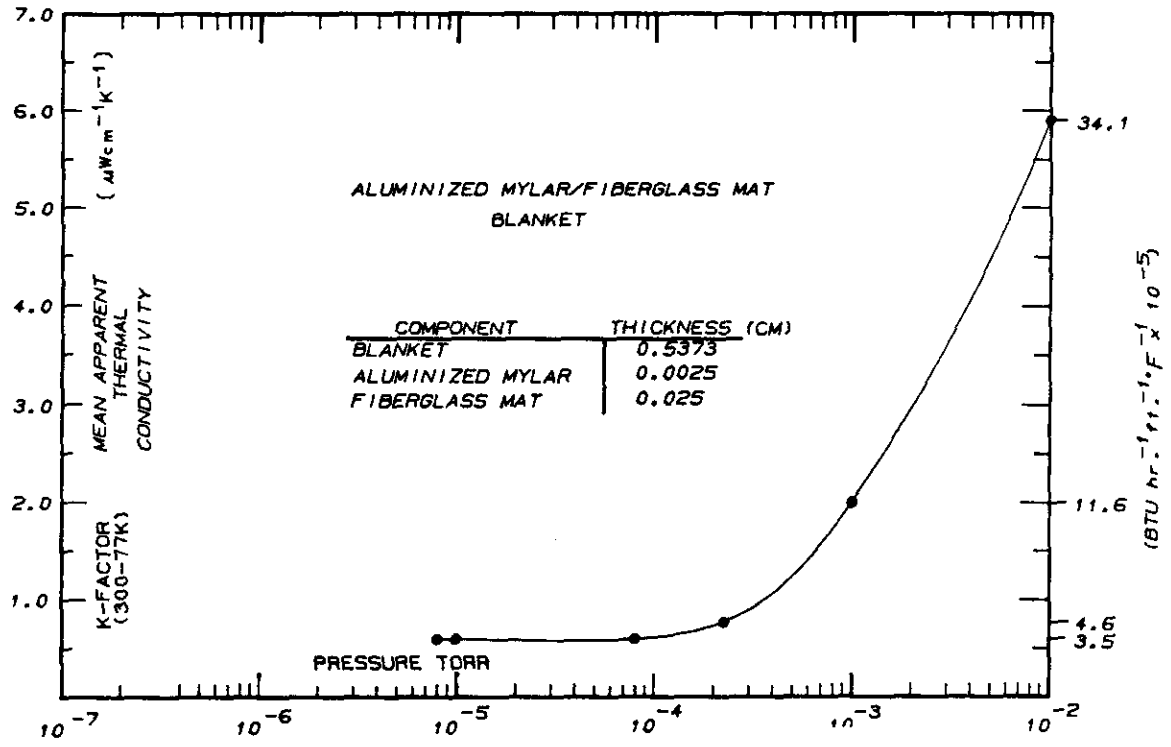

Figure B.13-12. Thermal conductivity vs. pressure for insulation material.

Cold mass helium containment vessel
Helium lines
Liquid nitrogen shield lines
Insulating vacuum vessel
Thermal radiation shield bridges
Insulation

The dipole-to-dipole electrical connections include:

Magnet current bus bars
Quench bypass bus bars
Quench protection diodes, instrumentation leads, quench detection voltage taps, correction coil leads, etc.

The interconnection design stresses the assembly and disassembly operations in the SSC tunnel. It permits the use of automated welding and cutting equipment that is essential for installation efficiency and interconnection reliability. For the Tevatron superconducting magnets system, a large fraction of the dipole cost was for the magnet ends. Therefore, the ends of the SSC magnet have been greatly simplified, using straight pipe connections between magnets. Cryogenic piping within the cryostat and the interconnection region is designed for an internal pressure at 20 atm, which is the maximum pressure envisaged during a quench. All pressure-tight connections are cylindrical and incorporate bellows for assembly and disassembly, and which allow axial thermal contraction. The bellows are of stainless steel and employ aluminum-to-stainless steel transition joints where required. For piping, two bellows are employed in series to increase the tolerance to offset. To obtain reliable leak-tight connections, all connections are welded stainless steel joints made by automatic welding equipment. Joints in the beam tube that separate the single phase helium flow from the beam vacuum are made with double wall bellows having an intermediate volume for leak interception. A small tube from the intermediate space is connected to the insulating vacuum space. This reduces the leakage in the outer bellows to the beam vacuum. On assembly, these bellows are the first joints welded. The main helium containment bellows slide over the cold mass assembly to permit access to diodes and to the electrical connections. Electrical connections (the main bus in particular) must provide adequate motion allowance, conductor support and insulation, high reliability and low heating due to conductor joints. After the electrical connections are made up, the single phase bellows is slid down and welds are made at each end. The helium pipes are then assembled. Retainers are provided for bellows whose internal pressure and length-to-diameter ratio could lead to excessive squirming.

The interconnection region incorporates 20 K and 80 K heat shield bridges to maintain the isothermal radiation heat transfer barriers. The bridges are attached to the magnet shields by riveting. Thermal connection is by means of copper braids, as in the support post heat intercept connections. A single blanket of multilayer insulation is installed on the 20 K shield bridge. Four blankets of multilayer insulation surround the 80 K shield bridge. The vacuum vessel shell has cantilevered ends to allow for the storage of the vacuum vessel bellows during magnet connection. Upon completion of insulation installation, the bellows is slid down and welded to the vacuum vessel.

The details of the interconnection region are shown in Figs. B.13-13, B.13-14, and B.13-15.

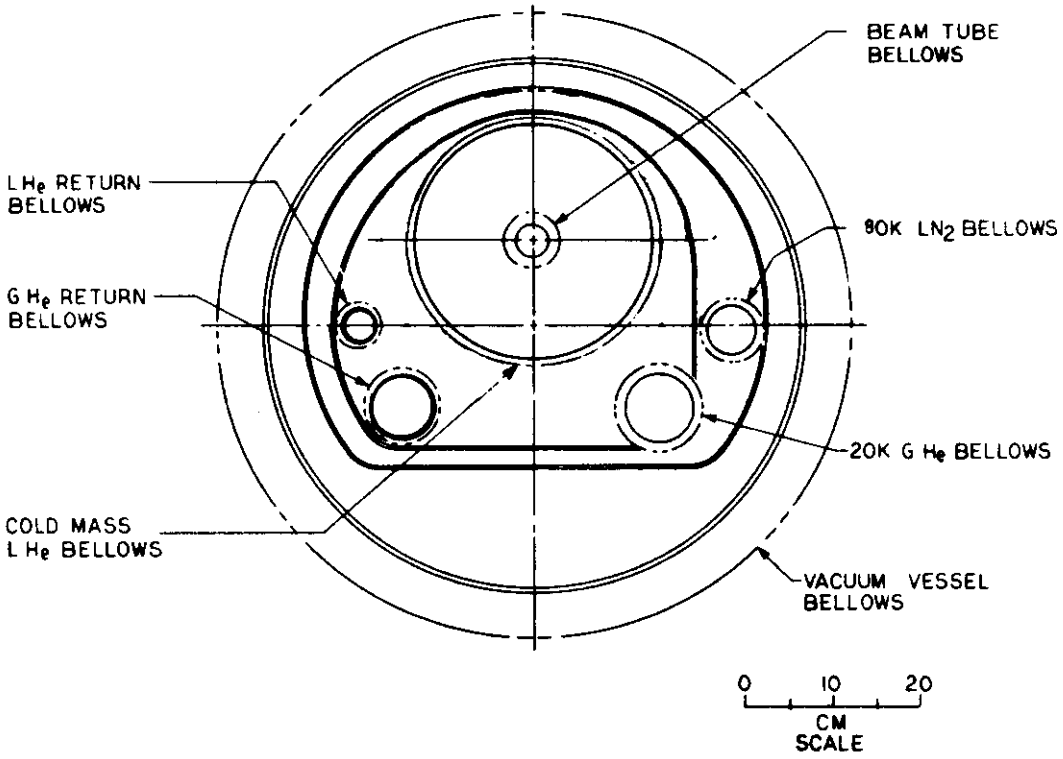

Figure B.13-13. Cross section of interconnection region, indicating the various bellows.

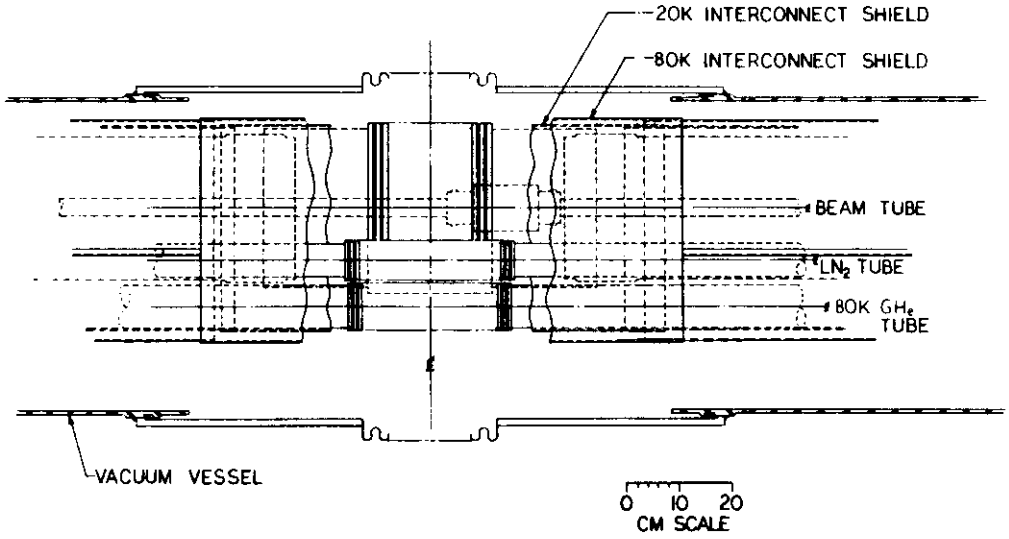

Figure B.13-14. Elevation view of interconnection region.

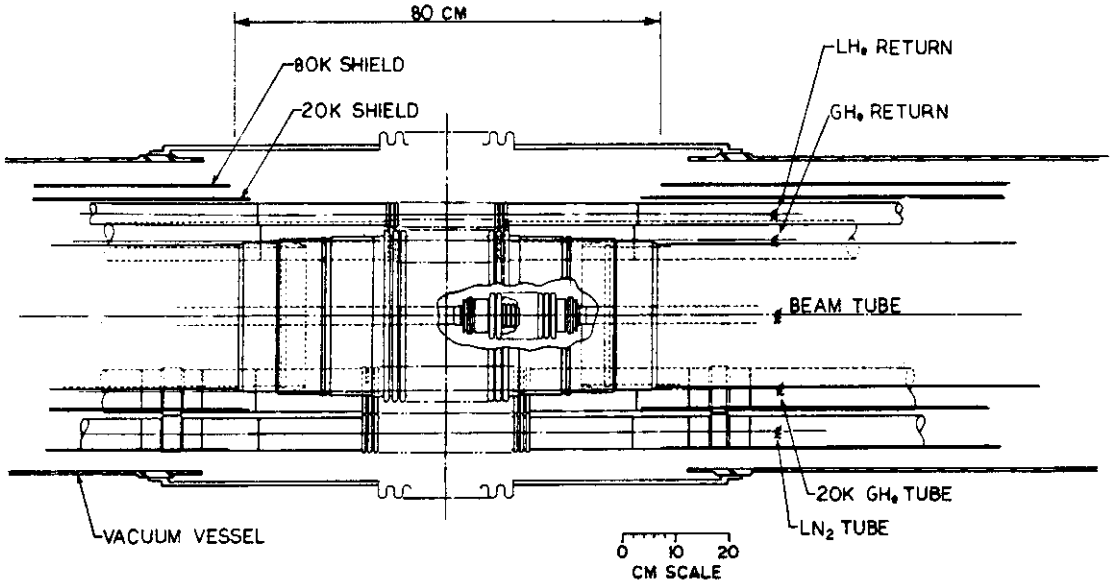

Figure B.13-15. Elevation view of interconnection region.

B.13.8 Heat Leak

The heat leak budget of the magnet cryostat consists of two major elements, thermal radiation and conduction through the suspension system. The budgeted cryostat heat leak totals, determined in conjunction with the design of the refrigeration system, are 25 watts to 80 K, 2.5 watts to 20 K and 0.3 watts to 4.5 K. The components of the heat leak budget are given in Table B.13-7. Other contributions to the total heat leak to the refrigeration system include 0.1 watt/magnet to 4.5 K due to ohmic heating in conductor splices and 2 watts/magnet to 4.5 K due to synchrotron radiation. The estimated center section heat leak for the dipole magnet cryostat Heat Leak Model is given in Table B.13-8.

Table B.13-7
Cryostat Heat Leak Budget per Magnet

	Watts to Temperature		
	80 K	20 K	4.5 K
Radiation	17.2	1.72	0.05
Supports and anchor	5.193	0.413	0.058
Voltage taps	0.1	0.01	0.01
Ends (junction)	1.0	0.05	0.05
Subtotal	23.493	2.193	0.168
Contingency	1.507	0.307	0.132
Total	25	2.5	0.3

Table B.13-8
SSC 16.6 m High Field Dipole Cryostat
Heat Leak Model
Center Section Heat Leak Prediction

	Watts to Temperature		
	80 K	20 K	4.5 K
Thermal radiation	17.68	1.778	0.002
Cold mass supports[a,b,c]	6.53	0.695	0.172
Cold mass anchor[d,b,c]	0.66	0.047	0.017
Total	24.87	2.52	0.191
Criteria budget	25	2.5	0.3

[a]For five 5 in. × 7 in. × 1/16 in. G11 CR reentrant posts.
[b]Corrected for predicted intercept temperatures of 85 K and 21 K.
[c]Corrected for calculated vs measured Suspension Heat Leak Dewar experience factor.
[d]For 2 in. × 0.050 in. G11 CR strut pair.

In support of the cryostat's thermal design, an intensive program of experimental heat leak measurements was conducted. The program included measurements of components (suspension system elements, multilayer insulation, etc.) under both normal and upset (partial loss of insulating vacuum) conditions. The results confirmed the ability to accurately predict thermal performance. The program also included measurements of full-length magnet thermal models. A typical open cycle thermal model is shown schematically in Fig. B.13-16. A full-length (12 m long) cryostat model corresponding to the ironless $\cos\theta$ dipole magnet was constructed, and heat leak measurements were made. Good agreement was obtained with the predicted values. The results are given in Table B.13-9. It is apparent that heat leaks to 80 K and 20 K can be very closely predicted, while the 4.5 K heat leak calculation vs. measurement appears to agree within 20%. It should be noted that, initially, this heat leak was predicted to be much lower. An instrumented support post in another magnetic model indicated that the temperature difference between the low temperature shield and the thermal intercept of the support post was approximately 10 K, increasing the support 4.5 K heat leak by a considerable amount. The results in Table B.13-9 include correction for the observed inefficiency of the thermal intercepts. The conceptual design cryostat development program includes an identical evaluation of a full-length dipole magnet cryostat. The center section of the model is manufactured in the Long Magnet Model Production Facility and uses production components, tooling, manufacturing procedures

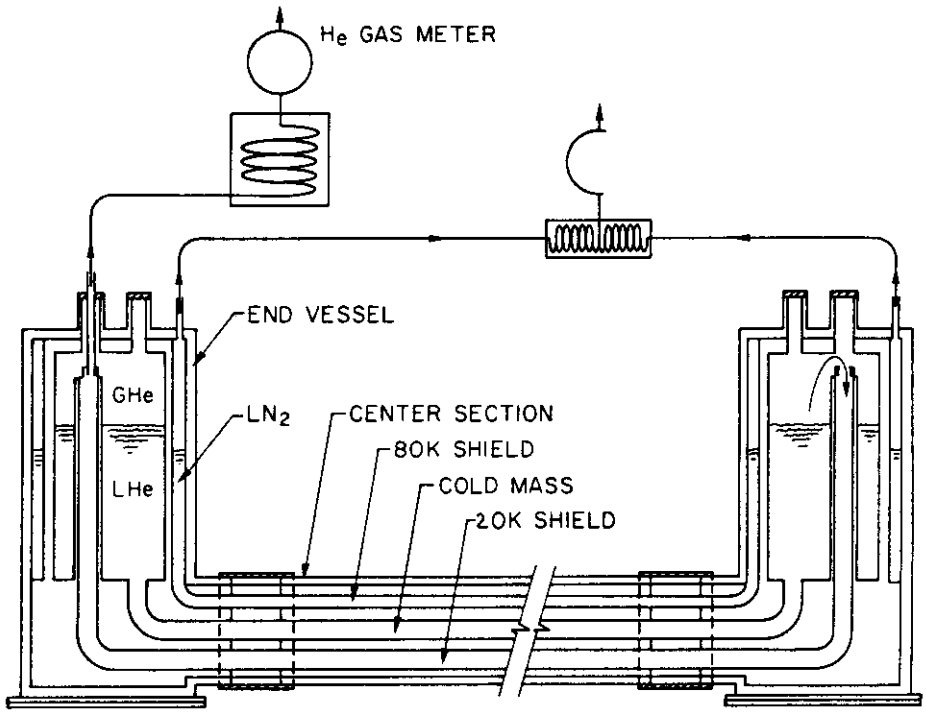

Figure B.13-16. Typical open cycle thermal model.

and quality control. Closed cycle heat leak measurements of a string of five magnet cryostats (Half Cell), with an operating cryogenic system, are part of the half cell String Test program.

Table B.13-9
SSC 12.5 m High Field Dipole Cryostat
Heat Leak Model I
Center Section Heat Leak Prediction

	Watts to Temperature		
	80 K	20 K	4.5 K
Thermal radiation	8.3	0.74	0.002
Support conduction[a,b,c]	21.2	1.54	0.440
Predicted total	29.5	2.28	0.442
Measured total	33.5	2.28	0.610

[a]Support not structurally optimized.
[b]Model did not include cold mass anchor.
[c]Corrected to reflect magnetic effects model instrumented post temperature profile

B.13.9 Dynamic Analysis and Testing

The effects of seismic, shipping and handling loads on SSC magnets are currently under study. ANSYS, a finite element code with excellent dynamic analysis capabilities, is being used to predict maximum stress and deflections in the magnet system to ensure structural integrity during all phases of installation and operation. Actual dynamic testing of completed magnets and individual supports will provide realistic damping values and verification of predicted results.

Seismic input data is taken from the A.E.C. Regulatory guide No. 1.60, "Design Response Spectra for Seismic Design of Nuclear Power Plants."

B.13.10 Safety

Safety considerations have played an important role in the cryostat design effort, including the following aspects:

- Design for the phases of assembly, testing, shipping and handling, storage, and both normal and upset operating conditions.

- Careful selection of realistic environmental factors for each phase.
- Use of materials with well understood properties.
- Conservative design approach with all vessels and piping conforming to ASME code, standard factors of safety, etc.
- Test of materials, components and systems under design conditions, to failure, etc.
- Internal and external design and safety reviews.
- Verification of design approach and validity of analysis by consultants.
- Failure mode analysis.

B.13.11 R&D Recommendations

It is recommended that the cryostat R&D program continue beyond the Conceptual Design effort in order to continue performance verifications and provide input essential for the Preliminary Design effort. The program should include the following elements:

(a) Magnet - Cryostat - Refrigeration system interactions and interfaces
(b) Performance requirements/specifications
  - Heat leak
  - Transportation, handling, seismic and operating dynamic structural environments
  - Installation
(c) Analysis
  - Structural response to dynamic loads
  - Structural response to thermal loads
  - Component optimization
  - Creep effects
  - Fatigue
(d) Measurements
  - Cold mass assembly static and dynamic structural properties
  - Suspension system structural, thermal, creep and fatigue properties
  - Insulation system properties
  - Shield system structural and thermal properties
  - Cryostat heat leak
  - Cryostat assembly dynamic responses
  - Response to upset conditions
  - Shipping and handling restraint and fixtures function
  - Installation in mock tunnel

Such R&D will further understanding of the cryostat performance and will result in a high degree of confidence in the resulting design.

References

B.13-1. R.A. Lundy, "State of the Energy Doubler," IEEE Trans. **MAG-17**, 709 (1981).
B.13-2. R. C. Niemann, et al., "Cryogenic Design of a Superconducting 5 T Dipole for the Superconducting Super Collider," Proc. Tenth Int'l. Cryo. Eng. Conf., Helsinki, Finland, Ed. H. Collan, P. Bergland, and M. Krusires, *ICEC10* 74 (1984)

Butterworth, Guildford, Surrey, UK.

B.13-3. R. C. Niemann, et al., "The Cryostat for the SSC 6 T Magnet Option," Adv. Cryo. Engr., **31**, (1986) Plenum Press, New York (to be published).

B.13-4. Design Criteria, Superconducting Super Collider, Design "D," Dipole Magnet Cryostat System, Fermi National Accelerator Laboratory, Batavia, Illinois, 1985 (unpublished).

B.13-5. R. C. Niemann, et al., "Design, Construction and Performance of a Post Type Cryogenic Support," Adv. Cryo. Engr., **31**, (1986) Plenum Press, New York (to be published).

B.13-6. P. O. Mazur, et al., "5-cm, No Iron SSC 6-m Dipole Test Program," Adv. Cryo. Engr., **31**, (1986) Plenum Press, New York (to be published).

B.13-7. R. J. Powers, et al., "5 cm, No Iron SSC Dipole 12 M Model Cryostat Thermal Performance," Adv. Cryo. Engr., **31**, (1986) Plenum Press, New York (to be published).

B.13-8. J. D. Gonczy, "Heat Leak Measurement Facility," Adv. Cryo. Engr., **31**, (1986) Plenum Press, New York (to be published).

B.13-9. M. Kuchnir, "Measuring Heat Leak with a Heatmeter," Adv. Cryo. Engr., **31** (1986) Plenum Press, New York (to be published).

B.13-10. T. H. Nicol, et al., "Thermal Shield Bowing in Long Superconducting Magnets," Cryo. Engr., **31** (1986) Plenum Press, New York (to be published).

B.14 Summary of Quench Performance and Field Quality Data from 1-Meter R&D Magnets

W. S. Gilbert
Lawrence Berkeley Laboratory

February 26, 1986

A total of ten 1-meter Reference Design D dipoles have been made and tested as part of the SSC R&D effort. All of these magnets have collars between the coils and the cold iron; two magnets use 25 mm wide aluminum collars, and the other eight have 15 mm wide stainless steel collars. The 3-wedge C5 cross section, with flared ends, was used in seven of the models. The new 4-wedge NC515 cross section, with straight and improved field quality ends, is used in the latest two models.

The training behavior of the 8 magnet, 3-wedge, series is shown in Fig. B.14-1. Most of the models reached their plateau central field value of 6.6 tesla at 4.4 K on the second or third quench, with the first quench occurring above 6 tesla. The eighth model was trained to its 4.5 K short sample value, without quenching, through a lower temperature conditioning operation. The magnet was cycled to 7.1 tesla in superfluid helium at 1.8 K before its operation at 4.5 K.

We measured the magnetic field qualities of the two models of the new 4-wedge cross section at room temperature. The second model was cryogenically tested. Although the new straight ends had some mechanical looseness, the first quench occurred at 5.5 tesla and the plateau field was 6.4 tesla.

Changes in shim thicknesses were made to control and change the mechanical prestress in the windings. Therefore the magnetic field quality was not expected to be the same for the entire series of magnets. In Table B.14-1 are listed the expected allowed multiples for the C5 cross section. Also listed are the average of the calculated multipoles of the seven magnets with their different size shims. The averages of the magnetic measurements are also shown. The agreement for the higher multipoles (b_6,b_8,b_{10}) is excellent. The new 4-wedge NC515 cross section was designed to reduce the higher multipoles to a value below 0.1 unit, and inspection of the table shows that the first models have succeeded in doing this.

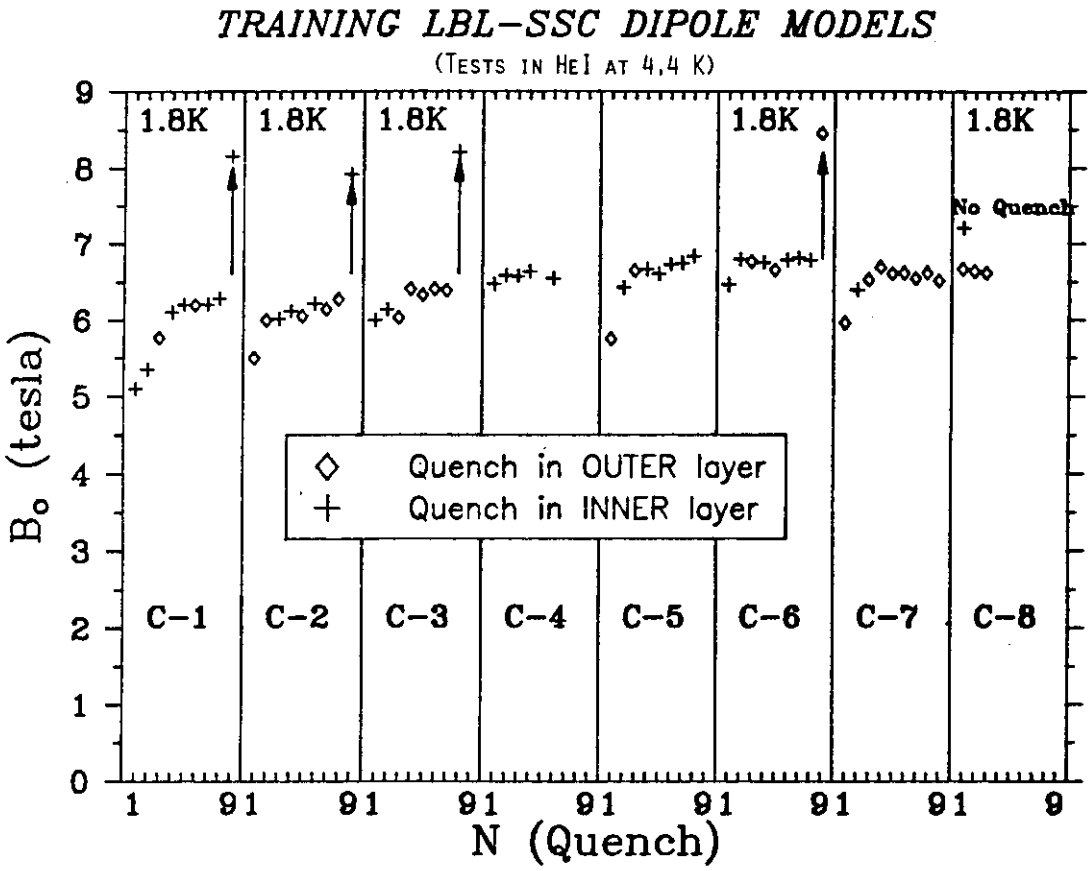

Figure B.14-1. Training performance of eight 1-m dipole magnets.

Table B.14-1
Calculated and Measured Multipoles of SSC Type Dipoles

Cross Section	Identification	Multipoles $\times 10^{-4}$				
		b_2	b_4	b_6	b_8	b_{10}
C5	Calculation - Design	0.4	0.0	0.2	0.8	0.0
	Calculation - As Built (Average of 7 Magnets)	6.5	−0.35	0.09	0.74	0.0
	LBL Measurements (Average of 7 Magnets, 3000 A)	7.4	0.56	0.12	0.73	0.0
NC515	Calculation - Design	0	0	0	0	0.01
	LBL Measurements (Warm) 2 Magnets	7.2	0.11	0.02	0.07	0.03
	(1 Magnet Cold, 3000 A)	8.1	0.13	0.03	0.06	0.03

B.15 Summary of Quench Performance and Field Quality Data from 4.5 m and 3.5 m R&D Magnets

P. Wanderer
Brookhaven National Laboratory

April 1986

A total of six 4.5 m and two 3.5 m Reference Design D dipoles have been made and tested as part of the SSC R&D effort. The two 3.5 m magnets were made to confirm a simplified, although not final, design of the coil ends.* This section presents training results and multipole data from these eight magnets.

The training results are presented in Figs. B.15-1 and B.15-2. On average, the magnets train in a few quenches to the "plateau" field, which is within a few per cent of the predicted short-sample limit of 6.4 T. At helium temperatures below 4.5 K, the magnets routinely reach fields of 7 T. The highest quench field is above 8 T. The typical critical current density of the conductor used in these magnets is 2400 A/mm^2. The CDR uses 2750 A/mm^2 as a critical current, and such conductor is now available. The training data from these eight magnets, at 4.5 K and lower temperatures, indicate that the design field of 6.6 T can be achieved with the desired margin of safety.

The average value of the transfer function is 1.0358 ± 0.0008 T/kA at 2 T. (An NMR probe was used to measure the dipole field.) This is close to the calculated value, 1.0379 T/kA [B.15-1]. The rms scatter among magnets is essentially the same as the estimate made by the Aperture Task Force and used in the choice of magnet aperture, 0.0007 T/kA [B.15-2].

The integral multipoles for the six magnets including the "dogbone" ends are summarized in Table B.15-1. For comparison with calculation, the allowed multipoles of all eight magnets, averaged over the center 75 cm, but excluding the ends of the magnet, are listed in Table B.15-2. The multipoles are listed at a field of 2.0 T. It is convenient to break the discussion of multipoles into two parts: the average values and the widths of the distributions. The discussion of average values in turn breaks into two parts, allowed multipoles (Table B.15-2) and unallowed multipoles.

A goal of this initial series of 4.5/3.5 m magnets was to establish that the design and measured values of the allowed multipoles are in good agreement. Once agreement has been established, the coil cross section can be iterated to match the final list of accelerator

*Future magnets will have the final version of the simplified ends.

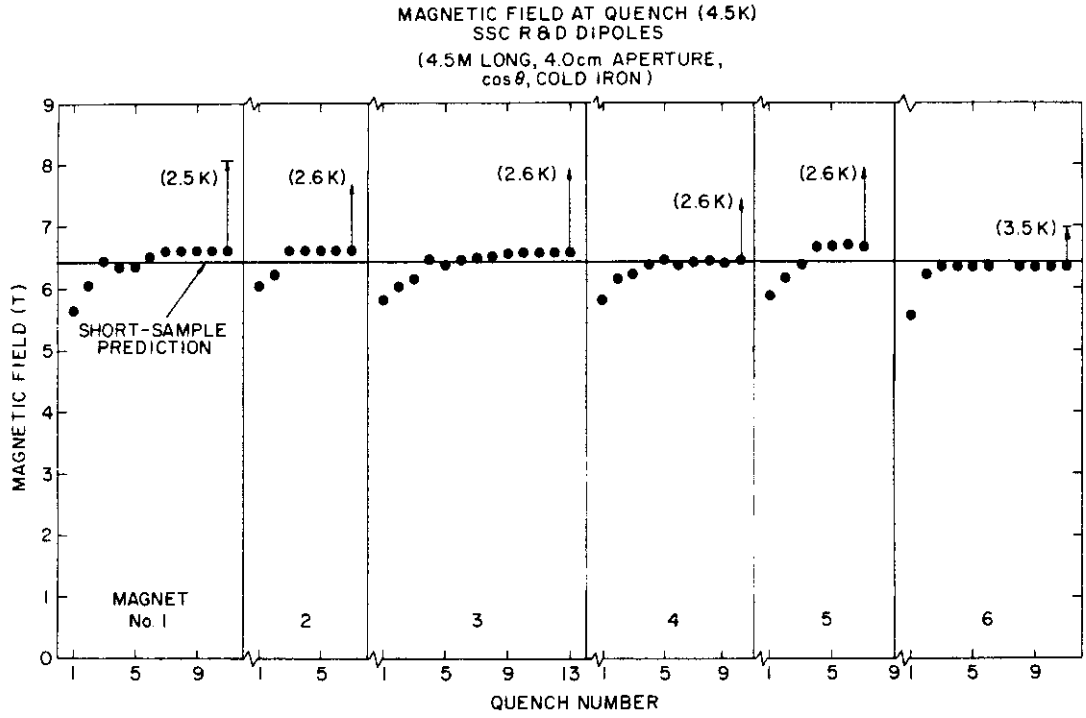

Figure B.15-1. Training performance of six 4.5 m dipoles.

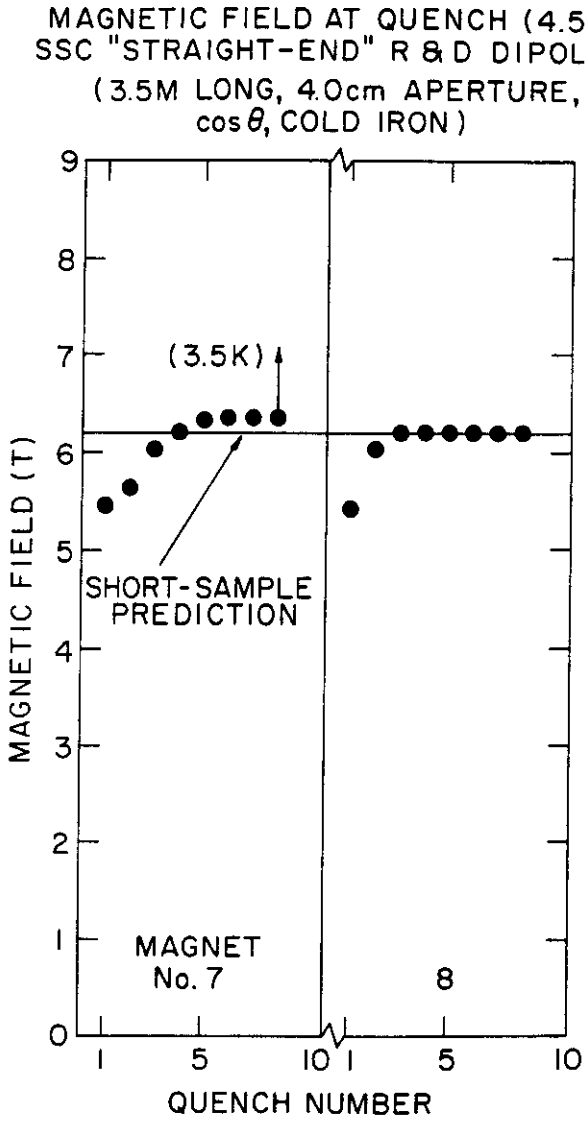

Figure B.15-2. Training performance of two 3.5 m dipoles.

Table B.15-1
Multipole Data for Design D Magnets (units of 10^{-4} cm^{-n})
Six 4.5 m Dipoles, Integral Field,
2 kA Excitation (~2 T)

	Mean ± σ, Measured	σ, Estimated[a]
b_1	0.41 ± 0.79	1.6 (0.7)[b]
b_2	8.57 ± 1.24	2.01
b_3	−0.12 ± 0.15	0.35
b_4	−0.68 ± 0.30	0.59
b_5	−0.01 ± 0.03	0.059
b_6	0.01 ± 0.06	0.075
b_7	0.07 ± 0.05	0.016[c]
b_8	0.81 ± 0.01	0.021[c]
b_9	0 ± 0.00	0.003[c]
a_1	−2.17 ± 2.77	3.3 (0.7)[b]
a_2	1.03 ± 0.22	0.61
a_3	−0.50 ± 0.29	0.69
a_4	−0.08 ± 0.12	0.14
a_5	−0.06 ± 0.11	0.16
a_6	0.03 ± 0.03	0.034
a_7	0.06 ± 0.08	0.030[c]
a_8	0.02 ± 0.01	0.006[c]
a_9	−0.01 ± 0.01	0.006[c]

Note: Results are not corrected for offsets of the measuring coil with respect to the axis of the magnetic field.

[a]"Magnetic errors in the SSC," SSC 7, 4/85, Table S-1 except for a_1 and b_1.

[b]The larger of the two values given for a_1 and b_1 are those expected for magnets built without the ability to adjust the collared coil in the iron (SSC 7, Table III.10); the smaller values assume adjustment (SSC 7, Table S-1). These first D magnets were not adjusted.

[c]Does not include measurement errors, for which σ is estimated to be −0.05 to 0.1.

Table B.15-2
Allowed multipole data and comparison with design for Design D magnets (units of 10^{-4} cm^{-n}). Eight 3.5/4.5 m dipoles, central field excluding ends, 2 kA excitation (~2T).

Multipole	σ, Estimated[a]	b_n, measured	b_n, measured − b_n, design
Sextupole, b_2	2.01	−4.6 ± 1.7	−5.6 ± 1.6
Decapole, b_4	0.59	−0.3 ± 0.7	0.1 ± 0.6
14-pole, b_6	0.075	−0.05 ± 0.07	−0.19 ± 0.07
18-pole, b_8	0.021	0.93 ± 0.02	0.07 ± 0.014

[a]Reference B.15-2.

requirements. For b_4, b_6, and b_8, the design and measured values agree to better than 0.2 units (Table B.15-2). The value of b_8, 0.9 units, is now known to be too large for the SSC, and the coil presented in the Conceptual Design Report has a b_8 design value of 0. The excellent agreement between the design and measured values of b_8 in the present series of magnets establishes that the design value will be achieved. The 5.6 units difference in b_2 between design and measured values (Table B.15-2) is due to differences between the design sizes and the sizes actually achieved in the coils and collars. The systematic offset in b_2 is removed by a small iteration in the coil parameters after construction and measurement of the initial eight or ten magnets of a particular coil design, as was successfully done for the CBA magnets. Note that the value of b_2 in Table B.15-1 differs from that in Table B.15-2 because of the "dogbone" ends included in the integral measurements.

The average value of the unallowed terms is expected to be zero, from symmetry. (There is little change in the unallowed multipoles with current.) The data in the left-hand column of Table B.15-1 show that, within statistical limits, the averages are zero for all but three of the unallowed harmonics. Two non-zero averages, a_1 and a_3, are linked to a previously known construction problem which may have affected a_2 as well. The problem occurred because of a small vertical off-centering of the collared coil in the yoke resulting from the keys of the collars being slightly larger than the keyways in the yoke (shown on the vertical and horizontal axes of the magnet in Fig. 5.2-2 of the Conceptual Design Report). When the yoke is assembled around the collared coils, the misfit produces the off-centering. This problem has since been remedied by widening the yoke keyway. The assembly of the first 16.6 m magnet (LLN001) was mechanically satisfactory, and it is expected that the value of a_1 will be satisfactory. The small value of b_1, which would be produced by a left-right miscentering of the collared coil in the yoke, indicates that a good match between keys and keyways can, in fact, be obtained.

The data on the widths of the multipole distributions should be compared to the estimated widths developed by the Aperture Task Force and listed in the right-hand column of Table B.15-1. The measured widths are smaller than the estimated widths for all multipoles through b_6 and a_6, even with the construction problems noted earlier. The widths of the distributions are similar at SSC injection and at 6.6 T.

The main (dipole) coil and the sextupole trim coil were powered simultaneously to demonstrate the correct operation of the trim coil. See Fig. B.15-3. The most difficult correction is at SSC injection, where about 30×10^{-4} units of sextupole are generated by magnetization currents in the present 20-micron NbTi filaments. (With 5 μm filaments in the final SSC conductor, magnetization currents will generate 5 units of sextupole at injection.) With the trim coil in operation, the residual sextupole can be reduced to an arbitrarily small value as shown in the figure. Also, the dipole and sextupole have been run together from injection to full field to demonstrate sextupole control over the full range of operation.

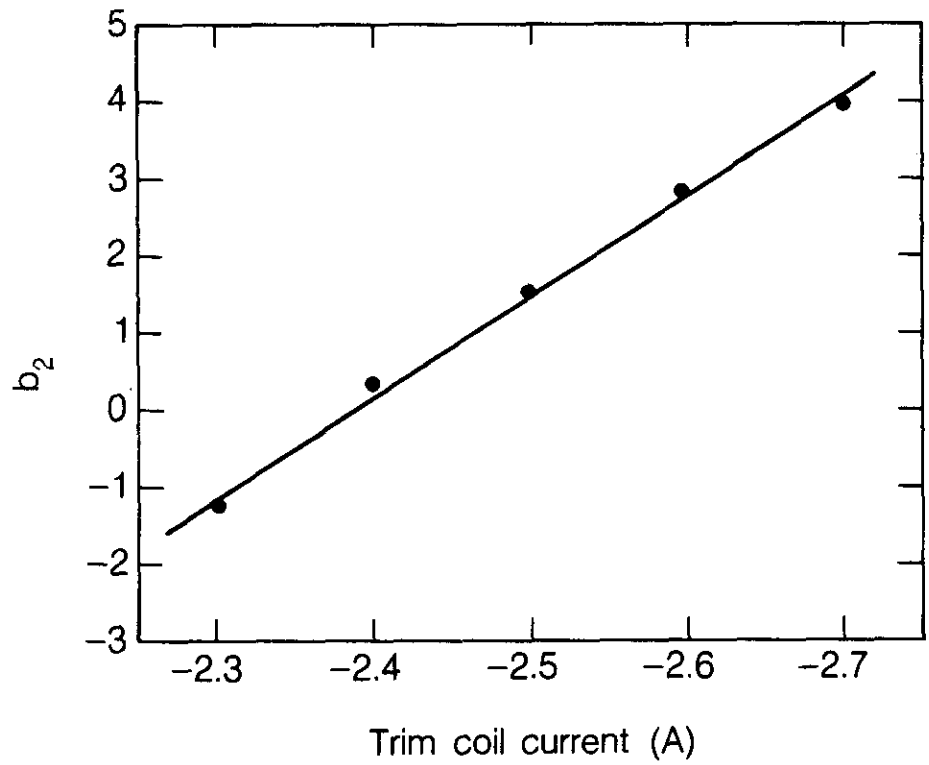

Figure B.15-3. Measurements of trim coil current required to adjust the total sextupole component in the dipole magnet. The main coil current is 300 A (~0.3 T). Units of b_2 are 10^{-4} cm^{-2}.

References

B.15-1. G. Morgan, private communication 12/10/85.
B.15-2. E. Fisk et al., SSC Central Design Group Report No. SSC-7 (1985), Table S-1.